Evaluating endothelial function during neurovascular coupling in awake behaving mice using advanced imaging technologies

Mohammed A. Shaik

Submitted in partial fulfillment of the requirements for the degree of Doctor of Philosophy in
the Graduate School of Arts and Sciences

COLUMBIA UNIVERSITY

2018

©2018

Mohammed A. Shaik

All Rights Reserved

ABSTRACT

Evaluating endothelial function during neurovascular coupling in awake behaving mice using advanced imaging technologies

Mohammed A. Shaik

Local neuronal activity in the brain results in increased blood flow and is called neurovascular coupling. Such blood flow changes result in the blood-oxygen level dependent (BOLD) fluctuations detectable by functional magnetic resonance imaging (fMRI). The hemodynamic response is also an essential component of brain health and is impaired in various models of cognitive dysfunction. However, we still do not understand *why* functional hyperemia in the brain is important. To understand this question, various groups have studied brain metabolic activity as well as the mechanisms underlying neurovascular coupling. Over the years, several cell types have been proposed to contribute to functional hyperemia in the brain, including neurons, astrocytes and pericytes. However, the picture remains incomplete – controversies abound regarding the exact role of astrocytes, and pericytes in neurovascular coupling.

Our lab has studies the mechanisms of neurovascular coupling from a mesoscopic perspective, as vasodilation in the rodent cortex involves capillaries and diving arterioles in the brain parenchyma as well as surface vasculature in the brain. We proposed that the vascular endothelium itself might provide a continuous conduit for transmitting vasodilatory signals initiated at the capillary level due to local neuronal activity. Given that systemic endothelial dysfunction could contribute to decreased neurovascular function, this hypothesis raised important concerns regarding endothelial vulnerabilities in common diseases like hypertension and diabetes and its role in diminished cognitive function and neurodegeneration.

Based on findings from vascular research in other organ systems, we hypothesized that two distinct mechanisms of endothelium-derived vasodilation significantly contribute to neurovascular coupling the brain. These two mechanisms were expected to consist of fast long-range endothelium-derived hyperpolarization (EDH) dependent vasodilation (conducted

vasodilation) and slower, more localized endothelium calcium-wave dependent vasodilation (propagated vasodilation). Together, we expected these mechanisms to shape the spatio-temporal evolution of hemodynamic responses in the brain. This dual mechanism of endothelial control of the hyperemic response in the brain might explain the complex spatiotemporal properties and non-linearities of the fMRI blood oxygen level dependent (BOLD) signal.

My initial experiments were conducted in anesthetized rats, where I pharmacologically inhibited endothelial dependent vasodilation during functional hyperemia in the somatosensory cortex under a hind-paw electrical stimulus paradigm. While the results gleaned from these experiments were very revealing, it was important to consider the effect of the pharmacological manipulations on neuronal activity in the brain. In addition, neurovascular coupling and overall brain blood flow in anesthetized animals is dramatically altered when compared to awake animals. In order to accomplish these goals, I built a wide-field optical imaging system that could simultaneously measure fluorescence-based neuronal activity and reflectance-based hemodynamic activity in awake head-restrained mice.

I then used non-blood brain barrier permeable pharmacology to study endothelial mechanisms of neurovascular coupling in awake Thy1-GCaMP6f mice, which express the calcium fluorophore in a subset of excitatory neurons in the cortex. I found that using this pharmacology I could dissect out the hypothesized two spatiotemporally distinct components of whisker-stimulus evoked neurovascular coupling in awake mice. With simultaneous recording of the neuronal activity driving this blood flow, I was able to build a mathematical model for neurovascular coupling that accounted for these two mechanisms by allowing for the superposition of a time-invariant, constant hemodynamic response with a hemodynamic response obtained by convolving the underlying neuronal response with a hemodynamic response function (HRF). I was able to linearize these apparent non-linearities in the hemodynamic response by studying the properties of deconvolved HRFs for stimuli of different durations before and after pharmacological manipulation of endothelial activity.

Two important considerations remain. Firstly, our wide-field, mesoscopic view of the brain prevents observations of endothelial function (hyperpolarization and calcium activity) and the propagation dynamics of dilation best observed at the microscopic level. To accomplish this task, ongoing experiments currently use our high-speed volumetric imaging technology (SCAPE – Swept Confocally Aligned Planar Excitation microscopy) to study stimulus-evoked vascular dynamics in mouse lines expressing GFP and GCaMP8 in endothelial cells.

Secondly, our longitudinal imaging of these animals is ideal for studying the acute and long-term effects of endothelial dysfunction on cognitive function. This requires adequate study of changes in mouse behavior during manipulations of endothelial function longitudinally in awake mice. Future experiments should involve the development and implementation of appropriate task-based behavior experiments, and analysis methods for more carefully exploring changes in neuronal activity in the mouse brain during stimulus and non-stimulus dependent activity.

Table of Contents

Definitions and list of acronyms

EDHF – Endothelium-derived hyperpolarization factor

fMRI – functional magnetic resonance imaging

BOLD – blood-oxygen level dependent signal

COX – cyclo-oxygenase

NAD – nicotinamide adenine dinucleotide

FAD -- flavin adenine dinucleotide

MS-OISI – multi-spectral optical intrinsic signal imaging

WFOM – wide-field optical mapping

HRF – hemodynamic response function

HbT – total hemoglobin

HbO – oxygenated hemoglobin

HbR – de-oxygenated hemoglobin

GCaMP – a genetically encoded calcium indicator made from a fusion of GFP, calmodulin & M13

GFP – green fluorescent protein

VSD – voltage sensitive dye

CCD – charge coupled device

EMCDD – electron multiplying charge coupled device

SCMOS – scalable/scientific complementary metal-oxide semiconductor

Acknowledgments

There are several people who have supported and guided me throughout my graduate work. My thesis advisor, Elizabeth Hillman, has been my mentor since I was an undergraduate student at Columbia University. Over the years, she has patiently and expertly trained me in bioinstrumentation, optics, neuroscience and vascular endothelial physiology – all of which will be invaluable to my future. She has unwaveringly believed in my abilities, tolerated my tendency to conduct distracting experiments, and continuously encouraged me to set high expectations of myself, high standards for my experiments and analysis, and to be meticulous with my written and presented work. I will continue to seek her mentorship for the rest of my scientific career, and am tremendously grateful for all she has done for my professional and personal growth.

My proposal committee members, Drs. Josh Jacobs, Christoph Juchem, Gordana Vunjak-Novakovic and Peter Canoll provided valuable insight and feedback towards formulating my work into a cohesive dissertation. I sincerely appreciate their guidance and enthusiasm for my research. I also want to specifically thank Dr. Peter Canoll for his generosity with both his lab's resources and the time he dedicated advising me on my future medical career.

Several of my colleagues have provided me with assistance and valuable advice, which has contributed significantly to my work. I would like to thank Sasha Rayshubskiy for encouraging me to continually read papers and update and expand my fund of knowledge. I would like to thank Sasha, Dr. Mariel Kozberg and Dr. Brenda Chen for training me in rodent surgical and experiment procedures. In addition, I would like to thank Mariel for the endless discussions and arguments we had over the mechanisms of neurovascular coupling and blood flow in the brain. Dr. Matthew Bouchard developed the original imaging system we used for our experiments – I would like to thank him for showing me how to build the system despite being extremely busy with his own thesis work. I would like to thank Dr. Pubudu 'Gali' Galwaduge for patiently listening to my ideas and for his encouragement, even though he may not have always understood or agreed with my theories.

Ying Ma and Jacob Portes helped me learn techniques for analyzing linear systems and guided me towards developing our model for neurovascular coupling in the awake mouse. Jacob spent many late nights with me patiently commenting and validating my code, and I'm grateful for his boundless enthusiasm for my work.

Without Sharon Kim none of my animal experiments would be possible. I am grateful for her patience and encouragement during our long animal preparations and her dedication to the care and comfort of our rodents. I would like to thank Venkatakaushik Voleti for our earnest discussions on the mechanisms of neurovascular coupling, and for continually challenging me to question and update my hypotheses on endothelial mechanisms of brain blood flow. I deeply appreciate his friendship and his constant reassurance, which has made it a pleasure to work in the Hillman lab.

I am deeply grateful to Teresa Zhao for reading and editing my thesis on extremely short notice. Her passion for science and zeal for life has made it an immense pleasure to be her desk-mate and friend. I thank David 'Nic' Thibodeaux for literally bringing music into my life (of data analysis) and for helping me develop and implement our behavior paradigms.

I would like to thank Wenze Li for help with SCAPE experiments, Hang Yu for help with two-photon experiments and Kripa Patel for help with analysis of 3D SCAPE data. I also thank Carla Kim for being an excellent lab manager, and for helping me conduct experiments towards the end of my time in the lab on short notice. In addition, Citlali Perez Campos has been an amazing friend and mentor, while also excellently managing the Hillman lab, and I thank her for her endless supply of oranges. I would like to thank my mentee Mary Kate Montgomery for teaching me how to guide and advise new trainees.

I would like to acknowledge the National Heart Lung and Blood Institute for generously funding my thesis work and my medical education via the F30 funding program, as well as the Columbia Medical Science Training Program.

Finally, I would like to thank Dr. Jenny Ruiz for her endless love and support and for helping me keep things in perspective. It has been a great pleasure to go through our education at Columbia together over the past 10 years.

1. Introduction and Background

The brain is a metabolically active tissue and has dynamically changing energy needs. To ensure normal brain function, the supply of blood flow to the brain needs to be tuned to its metabolic needs. However, brain metabolism and blood flow do not follow simple rules of matching energy supply to energy demand. Hence, the mechanisms underlying changes in metabolism and blood flow during functional activation of the brain have been studied for several years. By elucidating these mechanisms, we can not only build an intuition for brain energetics, but also begin to understand how alterations in brain metabolism and blood flow during vascular and neuronal disease affect brain health. Here, we primarily focus on brain blood flow, where we explore the mechanisms by which the vascular endothelium itself provides adequate blood supply to the brain. While in the vasculature of other organ systems, endothelial vasoactivity has been deeply explored, a similar understanding of endothelial function in the brain is still lacking. We thus set out to explore the contributions of the endothelium to neurovascular coupling in the brain.

Chapter 1 begins with a description of neurovascular coupling and the peculiar organization of the brain's macro- and microvasculature. We then briefly explore the relationship between functional hyperemia and brain metabolism. The contributions of various brain cell-types to the control of neurovascular coupling at different levels of the brain vasculature is then described. Finally, we review prior studies describing endothelial-dependent mechanisms of vasodilation in the brain.

In **Chapter 2**, we describe optical imaging methods for studying neuronal activity, brain metabolic activity and brain blood flow. We first describe reflectance imaging for measuring brain hemodynamics, followed by speckle imaging for measuring brain blood flow, and conclude with methods for fluorescence imaging of brain metabolic and neuronal activity.

In **Chapter 3,** we use our MS-OISI imaging system to study brain hemodynamics in anesthetized rats. We observe the complex spatiotemporal nature of the stimulus-evoked hemodynamic response, as well as the differential effects of ketorolac, enalaprilat and calcium channel blockers (nimodipine/nicardipine) on stimulus-evoked blood flow. While these pharmacological manipulations were primarily meant to affect brain endothelial function, some of them had complex effects on systemic blood pressure and baseline brain blood flow. These, and additional confounds related to slow vascular oscillations, anesthesia and the lack of measurements controlling for changes in brain neuronal function, led us to consider developing a better experimental paradigm for studying brain endothelial function and neurovascular coupling.

In **Chapter 4**, we describe the development of our wide-field optical mapping (WFOM) system, designed to simultaneously measure brain-wide neuronal activity and hemodynamics in the awake, behaving mice. We describe the process through which we extract the pure fluorescence signal indicating neuronal activity from the raw fluorescence data, which is confounded by hemodynamic artifacts. In a study describing the relationship between neuronal activity and blood flow during the "resting state", we describe analytical techniques that are used to quantify neurovascular coupling by creating hemodynamic response functions (HRFs). We also briefly discuss our observations of resting state neuronal activity and hemodynamics in the awake and anesthetized mouse. We show that anesthesia and pharmacological manipulations can have dramatic effects on resting-state neuronal activity and hemodynamics in the brain, which can, in turn, alter stimulus-evoked neuronal activity and blood flow. These findings set the stage for finally studying endothelial activity during neurovascular coupling in a controlled manner.

In **Chapter 5**, we use the WFOM system, analysis tools developed from describing resting-state activity, and insight from our pharmacological studies in anesthetized rats to study the contribution of endothelial mechanisms of vasodilation to stimulus-evoked neurovascular coupling in the awake mouse. By using ketorolac and ketoconazole, two non-blood brain barrier permeable drugs that target different mechanisms of endothelial vasoactivity, we are able to dissect two spatiotemporally distinct contributions to hemodynamic changes in the brain. We additionally show that the normal stimulus-evoked hemodynamic response can be mathematically modeled as a superposition of two components of vasodilation derived from separate endothelial mechanisms. We discuss the mechanisms of endothelium dependent vasodilation from a microscopic level, and the imaging tools (light-sheet SCAPE microscopy) that can be used to study these mechanisms in more detail. Finally, we discuss the behavioral aspects of stimulus-evoked hemodynamics in the brain and the effects that these pharmacological agents may have on neuronal activity as a result of altered brain blood flow.

We hope that, in future work, in depth studies looking at pharmacological and disease-derived disruptions of endothelial function and the downstream effects on neurovascular coupling, neuronal activity and mouse behavior will fully elucidate the relationship between altered vascular function and brain health.

1.1 What is neurovascular coupling?

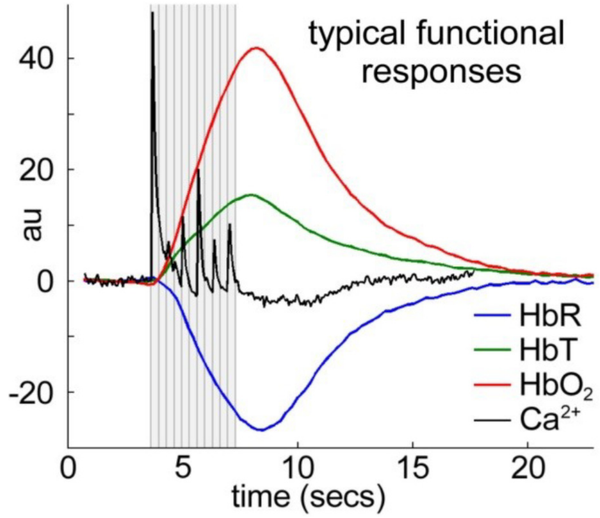

Fig 1. Neurovascular coupling. Calcium imaging of neuronal activity in the brain (black) during hind-paw stimulus. This results in an increase in total blood volume (total hemoglobin, HbT, green), and an increase in blood oxygenation (HbO_2, red), i.e. a concomitant decrease in deoxygenated hemoglobin (HbR, blue).

Local neuronal activity in the brain results in increased blood flow and is called neurovascular coupling. Blood oxygenation changes resulting from this increased blood flow manifest as the blood-oxygen level dependent (BOLD) fluctuations detectable by functional magnetic resonance imaging (fMRI). This increase in blood flow is a direct result of vasodilation in the brain. Hence, functional hyperemia involves changes in the blood volume, blood oxygenation level and blood flow in the active region of the brain (Fig 1). The total blood volume changes in the brain actually results in changes in total brain volume, and were first observed over a century ago with functional stimulation of the brain (Roy & Sherrington, 1890). As seen in Fig 1, fast changes in neuronal activity result in a slower actuation of the vasculature – the hemodynamic responses peak a few seconds after stimulus-evoked activity begins in the cortex.

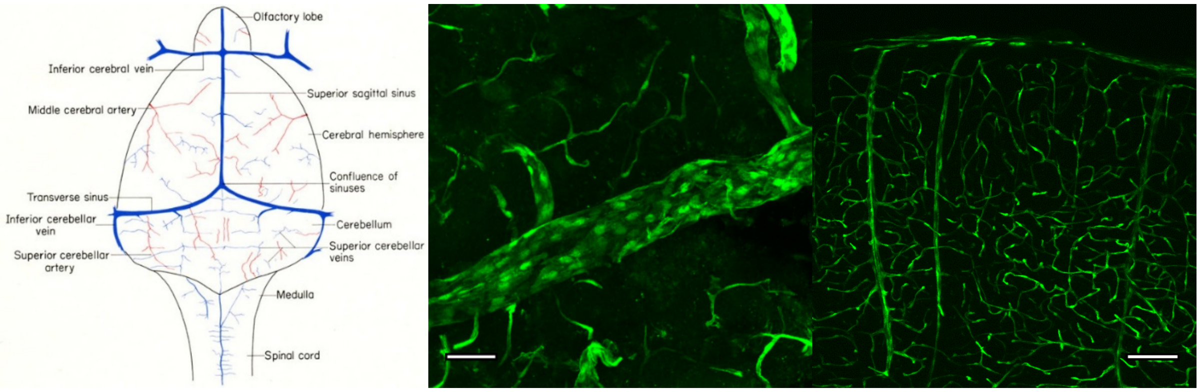

Fig 2. Structural organization of vasculature in the brain (Left) Surface level organization of the vasculature supplying the rodent cortex (Adapted from www.jax.org). (Middle) Section of a surface artery of the mouse brain (50 um scale bar) in a Tie2-GFP mouse, an endothelial marker. (Right) Diving arterioles and capillaries of a cross-section of a Tie2-GFP mouse (100 um scale bar)

To properly understand the spatio-temporal properties of the hemodynamic response, it is important to first understand the structural organization of the vasculature in the brain. Here, we focus on the organization of the vasculature in the rodent cortex (Fig 2). The middle and anterior cerebral arteries, derived from internal carotid artery supply each cortical hemisphere from the lateral side and the central sulcus respectively. These arteries sit above the pia mater in the sub-arachnoid space. Branches of these surface arteries on the cortical surface dive at 90 degree angles into the brain forming diving arterioles that penetrate through some or all layers of the cortex. The diving arterioles then split off into pre-capillary arterioles followed by the capillary plexus of the brain. The convoluted capillary plexus make contact with diving venules which merge on surface veins which eventually drain into one of the three major venous sinuses.

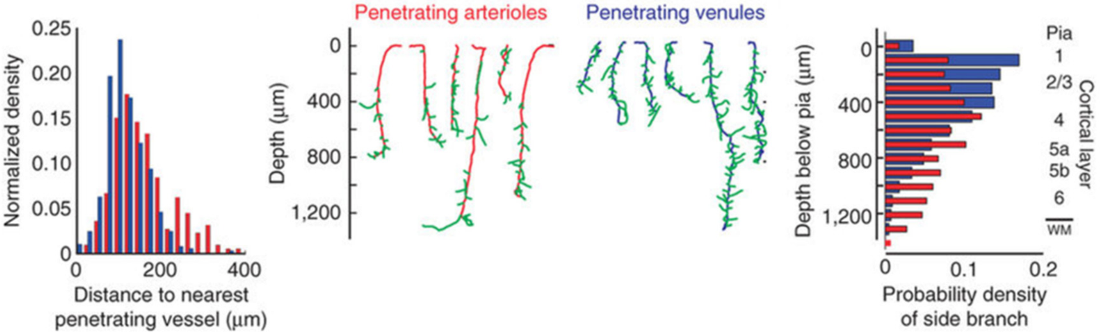

Fig 3. Adapted from (Blinder et al., 2013) Left: Average distance between two penetrating vessels (veins in blue, arterioles in red). Center: Example image of diving vessels, with color coded arterioles, venules and capillaries. Right: Depth dependent probability of a diving vessel having a side branch.

The organization of the diving vasculature is particularly interesting from a tissue engineering perspective. An important study conducted a few years ago (Blinder et al., 2013) quantified the structural organization of the diving vasculature and found that the average distance between two diving vessels is about 150 μM (Fig 3). Another study, using two-photon imaging of NADH auto-fluorescence (Kasischke et al., 2011), found that the intensity of the NADH signal changed dramatically as a function of distance from the center of each diving arteriole, and could be modeled as a "Krogh cylinder", used to study the diffusion of oxygen from vasculature. The NADH signal (further discussed below) is a marker of the redox state of the tissue, which is directly related to local oxygenation. Overall, these studies suggest that the organization of the cortical vasculature is no mistake, but rather it's optimized to adequately supply oxygen and glucose to a tissue with high and constantly changing metabolic needs.

At the microscopic level, many previous studies have focused on the neurovascular coupling at the level of capillaries, or at diving arterioles at specific depths in the cortex. However, from a mesoscopic perspective, neurovascular coupling occurs at capillaries, diving vessels and the surface vasculature – a proper study of functional hyperemia in the brain requires that we study vasodilation at all three levels.

1.2 The relationship between functional hyperemia and metabolism

Alongside the mechanisms of neurovascular coupling, it is also crucial to understand exactly *why* increases in neuronal activity are associated with changes in brain blood flow. Conventional wisdom suggests that increased metabolic demand manifests as a transient decreased in local oxygenation in the brain and the local vasculature supplying the tissue. This implies that increased neuronal activity would be associated with transient decreases in the blood oxygenation of the local vasculature. Indeed, early studies using red reflectance imaging of the brain found that the measured hemodynamic signal during stimulus-evoked responses had a so-called "initial dip" (Hu & Yacoub, 2012), indicative of transient de-oxygenation in the brain, followed by a an overshoot, i.e. a delayed over-oxygenation. In addition, *in vitro (Brennan, Connor, & Shuttleworth, 2006)* and *in vivo* studies employing intrinsic fluorescence imaging of NADH (nicotinamide adenine dinucleotide) and FAD (flavin adenine dinucleotide), found similar a similar "initial dip" (decreased NADH), or "light phase" (increased FAD), followed by an overshoot ("dark phase"), suggestive of decreased tissue oxygenation and increased metabolic demand (Fig 4. Also see 2.4.3 Metabolites -- NADH and FAD for description of NADH and FAD fluorescence imaging). Alongside these experiments, an exciting hypothesis emerged regarding the metabolic machinery of the brain – the so-called "lactate shuttle" hypothesis (Pellerin et al., 1998). In simple terms, the hypothesis asserts that the neuronal metabolic machinery is attuned for oxidative phosphorylation, whereas astrocytes are more efficient at glycolysis. Following neuronal activation, and the initial de-oxygenation in neurons, astrocytes would rev up glycolysis and convert glucose to lactate. The lactate molecules would then "shuttle" over to neurons, and be subsequently used to restore the redox state of surrounding neurons. An elegant Science paper by Kasischke et al. (Kasischke, Vishwasrao, Fisher, Zipfel, & Webb, 2004) demonstrated that *in vitro* the initial dip was indeed localized to neurons, whereas the subsequent overshoot occurred in astrocytes (Fig 4), popularizing the "lactate shuttle" hypothesis.

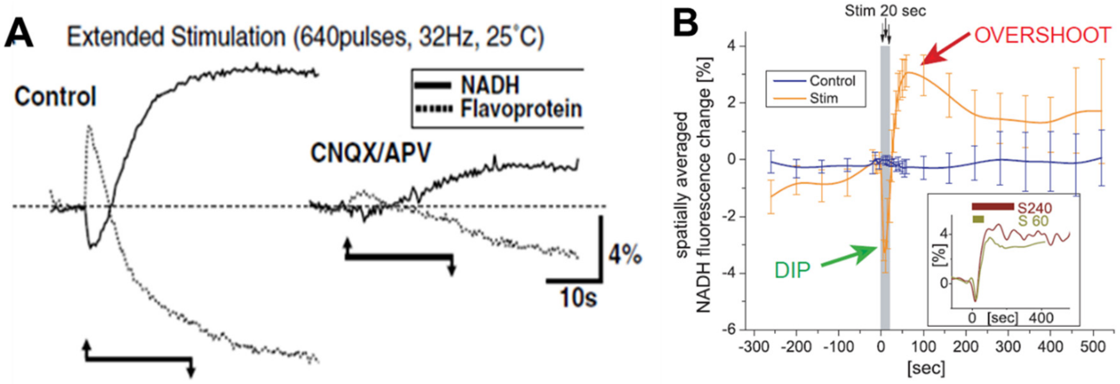

Fig 4. In-vitro measurements of FAD and NADH fluorescence. A. (Brennan et al., 2006) observed biphasic FAD/NADH responses in-vitro using extended stimulation and wide field imaging. B. Using 2 photon microscopy (Kasischke et al., 2004) reported an NADH 'dip' and 'overshoot' in response to 20 second stimulation in the hippocampal slice.

Subsequent literature, however, began reversing some of the (now dogmatic) findings regarding the initial dip in intrinsic reflectance imaging studies. Red reflectance imaging, which predominantly measures changes in de-oxygenated hemoglobin, shows that there is an "initial dip" in the hemodynamic response. However, using different wavelengths of light (described in -- 2.1 Optical intrinsic signal imaging), one can actually approximate the changes in the pure de-oxygenated and oxygenated hemoglobin signal. In this improved paradigm, the initial dip, while present in the raw reflectance data, disappears from the approximated de-oxygenated hemoglobin data(Sirotin, Hillman, Bordier, & Das, 2009).

With intrinsic fluorescence imaging, the local oxygenation state of *in vitro* slices dramatically changes the nature of the biphasic NADH responses (Galeffi, Somjen, Foster, & Turner, 2011)– lower *in vitro* tissue oxygenation results in a greater consumption response and a small overshoot (over-oxygenation). *In vivo* brain parenchymal pO2 concentrations are often much lower than *in vitro* preparations of brain tissue, hence lower external tissue oxygenation is more representative of the local environment. Indeed, *in vivo* imaging studies using wide-field fluorescence imaging of FAD fluorescence reveals a predominantly monophasic increase in FAD signal (oxygen consumption) under conditions of stimulus-evoked increases in neuronal activity (Kozberg, Ma, Shaik, Kim, & Hillman, 2016). NADH wide-field imaging is extremely difficult, given that NADH fluorescence excitation peaks in the ultraviolet regime, and ultraviolet light does not penetrate significantly into brain tissue.

Several groups considered using two-photon imaging of cell-localized NADH and FAD fluorescence to visualize changes in metabolic activity several hundreds of microns deep into the rodent brain. The low signal-to-noise of intrinsic fluorescence greatly increases the difficulty of these in vivo imaging studies. While dramatic changes in metabolic activity manifest well in the two-photon NADH fluorescence (Baraghis et al., 2011), curiously, no analogous studies have been published with FAD fluorescence. Under stimulus-conditions, the two photon signal of NADH and FAD molecules is dominated by photo-bleaching, which has made it quite difficult to carefully dissect the pathways of brain metabolic activity under physiological conditions. Our own preliminary experiments with two photon imaging of FAD imaging showed monophasic increases in FAD fluorescence during stimulus-evoked neurovascular coupling, followed by a small undershoot post-stimulus. With NADH imaging, photo-bleaching dominates, and no discernable changes in NADH fluorescence are seen during the stimulus. However, a small, significant NADH overshoot is observed after the stimulus is over, suggesting that perhaps changes in the redox state are perhaps somewhat biphasic, but not during the period of increased metabolic demand. Instead the observed overproduction of NADH and decreased FAD occur after the metabolic demand returns to baseline – this may occur as a consequence of increased blood flow due to neurovascular coupling (Fig 5).

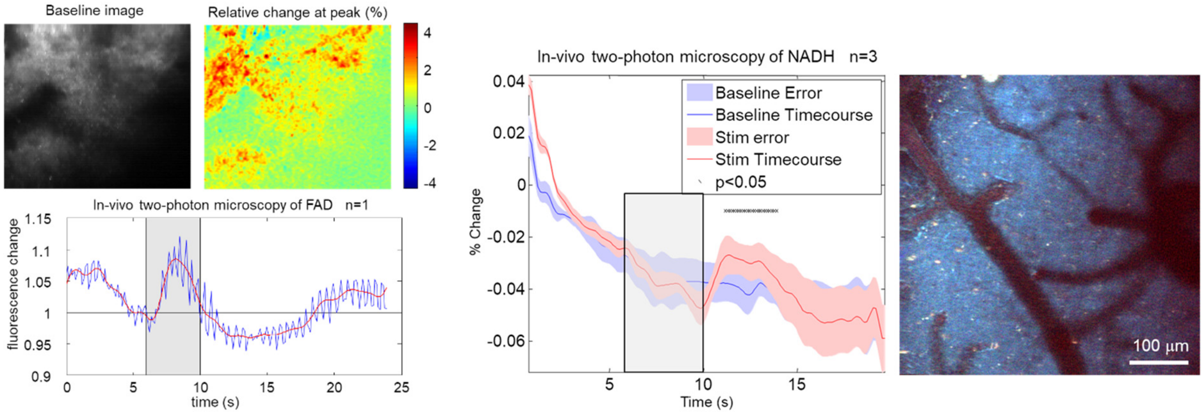

Fig 5. Left: In-vivo 2-photon measurements of FAD dynamics in response to stimulus. Top right shows map of peak % signal change. Plot shows time-course of green 505-560 nm emission. Right: In-vivo 2-photon measurements of NADH dynamics in response to stimulus. The time course with standard error shows average changes in the blue 350-505 nm channel in 3 rats. Stim runs (red) were recorded alternating in sequence with baseline runs (blue). Map to the right shows a typical RGB merge of intrinsic fluorescence in all 3 channels at 740 nm excitation.

Finally, studies in recent years (Tang, 2017) have directly contradicted the lactate shuttle hypothesis, showing that activated neurons can happily use both glycolysis and oxidative phosphorylation. In summary, the initial philosophy regarding biphasic responses of oxygen consumption and production is under serious debate. An updated understanding of brain metabolomics suggests that increased neuronal activity results in increased local oxygen consumption in the brain parenchyma that precedes an increase in local blood oxygenation resulting from the hemodynamic response.

1.3 Cell types proposed to contribute to neurovascular coupling

At the capillary level, neurons can communicate dilatory signals to the endothelium and pericytes. Pericytes are contractile cells (similar to smooth muscle cells) that sparsely populate (Mishra et al., 2014) the capillary plexus and pre-capillary arterioles that could control capillary diameter. Pericytes are distinguished from smooth muscle cells based on their morphological and cell lineage properties (Attwell, Mishra, Hall, O'Farrell, & Dalkara, 2016). In addition, the expression of pericytes does not extend to diving arterioles, where contractility is provided by smooth muscle cells.

Astrocytic processes form a continuous sheath from capillaries to diving arterioles (Fig 6), most importantly as part of the blood-brain barrier. This also implies that astrocytes can communicate vasodilatory signal to diving arterioles in addition to capillaries. Finally, the surface vasculature (Fig 6) is not contacted by central neurons or astrocytes (McCaslin, Chen, Radosevich, Cauli, & Hillman, 2011) given that both of those cells are limited to the pia mater. Of course, peripheral perivascular neurons exert tonic control over the surface vasculature based on sympathetic/parasympathetic changes in tone.

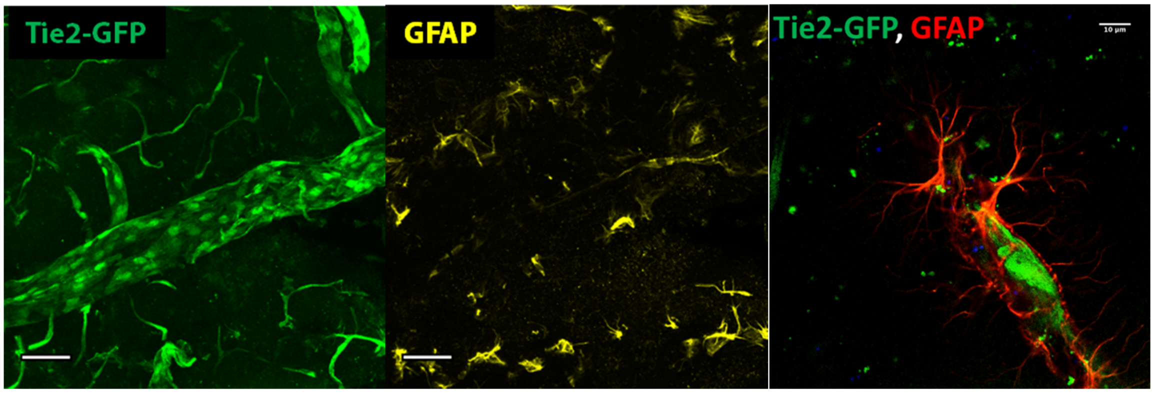

Fig 6. Left (50 µm): Surface vasculature of a Tie2-GFP animal – Tie2 expresses in the vascular endothelium Middle (50 µm): GFAP image of the surface vessel – there is no GFAP expression in the surface. Right (10 µm): Diving vessel showing astrocytic processes enveloping the vessel and the vascular endothelium inside the vessel.

Neurons have the ability to release vasodilatory molecules (Lacroix et al., 2015; Lecrux et al., 2017; Lecrux et al., 2011) directly onto the capillaries and diving arterioles, however these contributions have been approached from a non-specific pharmacological perspective that doesn't take into the account the release of these same dilatory molecules by surrounding cells, including the endothelium itself. While pericytes can control capillary dilation *in vitro* – it is unclear whether *in vivo* pericytes themselves dilate capillaries or if blood flow changes upstream of capillaries result in passive dilation of capillaries and the pericytes surrounding them. There is also controversy over the morphological distinction of pericytes from smooth muscle cells, hence questioning a specific role of pericytes during neurovascular coupling. Astrocytes can control diving arteriole vasodilation *in vitro* or during non-physiological stimulation paradigms *in vivo* (optogenetic activation, exogenous calcium release, startle responses, abnormally long stimuli). However, under physiological stimulus paradigms, calcium increases in astrocytes, thought to be crucial in initiating the vasodilation cascade, either occur too slowly or not at all (Bonder & McCarthy, 2014; Nizar et al., 2013), often after vessel dilations have already been initiated. While some analysis methods have revealed fast astrocyte calcium transients in the brain (Lind, Brazhe, Jessen, Tan, & Lauritzen, 2013), these appear to play no role during stimulus-evoked vasodilation in the brain (Lind et al., 2017). These results have led some studies to suggest that astrocytic control of blood flow in the brain might be restricted to tonic control required for autoregulation (Filosa, Morrison, Iddings, Du, & Kim, 2016; Rosenegger, Tran, Wamsteeker Cusulin, & Gordon, 2015) rather than dynamic fluctuations in blood flow during changes in local neuronal activity.

1.4 Prior studies exploring the spatiotemporal properties of functional hyperemia

Given what we know about the organization and complexity of the vasculature and of cells that can control vasoactivity in the brain, we can recognize that functional hyperemia in the brain must have a complex spatiotemporal pattern that may or may not be exactly related to local neuronal activity or metabolic demand. Initial approaches to modeling and interpreting the fMRI BOLD signal assumed linear relations in which a simple impulse or hemodynamic response function (HRF) could be convolved with some driving function representing neuronal activity (Geoffrey M Boynton, Stephen A Engel, Gary H Glover, & David J Heeger, 1996; Buxton, Wong, & Frank, 1998; Heeger & Ress, 2002). The linearity of the BOLD response was subsequently questioned by numerous reports (Berwick et al., 2008b; Devor et al., 2003; Karl J Friston, Mechelli, Turner, & Price, 2000; Hewson-Stoate, Jones, Martindale, Berwick, & Mayhew, 2005; Hirano, Stefanovic, & Silva, 2011; Chris Martin, John Martindale, Jason Berwick, & John Mayhew, 2006; C. Martin, Y. Zheng, N. R. Sibson, J. E. W. Mayhew, & J. Berwick, 2013; John Martindale et al., 2005; Sheth et al., 2004; Yeşilyurt, Uğurbil, & Uludağ, 2008), which identified nonlinear scaling in the amplitude and duration of the hemodynamic response to stimuli of different frequencies, amplitudes, and durations, as well as complex spatiotemporal dynamics. Such nonlinearities could potentially have consequences for the analysis and interpretation of fMRI and NIRS data, which in current practice often rely on the assumption of spatiotemporal linearity.

Simple analyses of the hemodynamic response include investigating the linearity of various time-courses of different stimulus durations for a single region of interest, and investigating the linearity of distinct spatial regions. In a seminal study that acquired neuronal and fMRI BOLD data simultaneously in primates, linear modeling required site-specific HRFs and found fit discrepancies for long-duration stimuli (Nikos K Logothetis, Jon Pauls, Mark Augath, Torsten Trinath, & Axel Oeltermann, 2001). Martindale et al. found that a linear convolution model could not predict measurements of blood flow responses to stimuli of longer duration (>2secs) in rat barrel cortex, regardless of the impulse response function chosen (John Martindale et al., 2005). Berwick et al. found two spatially distinct hemodynamic responses to single whisker stimulation in anesthetized rat barrel cortex: a transient response in the "upstream" branches of surface arteries and a later highly localized increase in blood volume centered on the activated cortical column (Berwick et al., 2008b). In a subsequent study of single whisker stimulation in awake rat, Martin et al. found biphasic response regions (initial increases in blood volume and oxygenation followed by subsequent decreases) in addition to a localized increase in blood volume centered on the activated cortical column (Chris Martin et al., 2013).

Various attempts have been made to develop elegant models to account for these nonlinearities, most notably by Martindale et al. and Zheng et al. (John Martindale et al., 2005; Zheng et al., 2010). The majority of these models, however, are purely descriptive and are not based on clear biological mechanisms.

As will become evident later, some of our experiments with pharmacological modulation of endothelial function, as well as our understanding of previously described mechanisms of endothelial vasoactivity led us to find a clear relationship between observed hemodynamic non-linearities and endothelial function. Hence, we next discuss previous work that explored the role of endothelium-dependent vasodilation in the brain during neurovascular coupling.

1.5 Prior studies describing the role of endothelium in neurovascular coupling

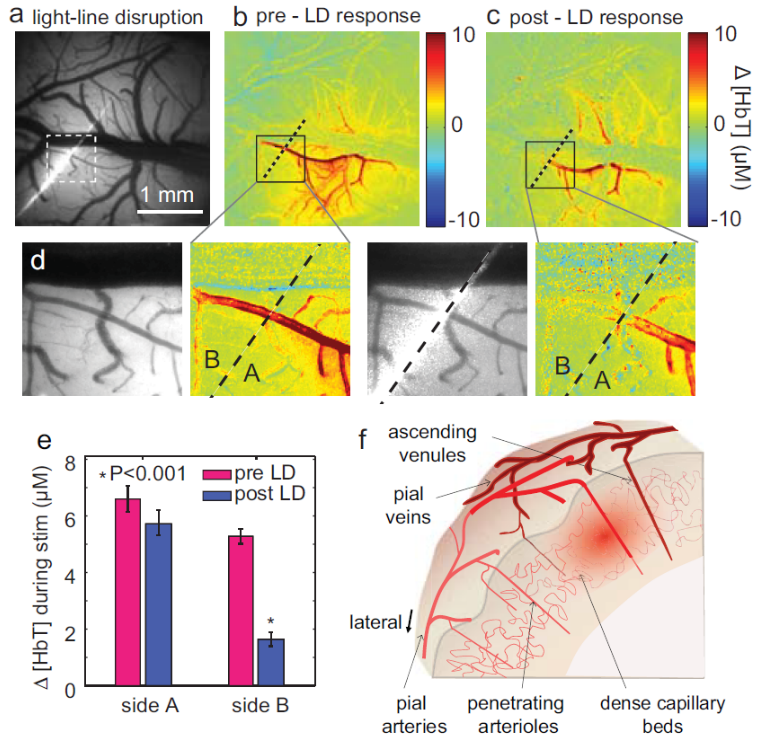

Fig 7. First confirmation of endothelium-dependent vasodilation (a) Somatosensory cortex with 'light line' used to transect a pial artery. (b) Δ[HbT] map prior to light-line treatment. (c) The same region post light-line. (d) Zoomed in regions of (b) and (c). (e) Summary over n=4 rats (Student t-test). (f) Schematic of cortical vascular organization showing the proposed route for signaling from capillary beds to pial artery dilation. (Adapted From Chen et. al. 2013)

As mentioned previously, the vascular endothelium itself provides a continuous conduit for transmitting vasodilatory signals initiated at the capillary level by local neuronal activity to diving arterioles and the surface vasculature. An endothelial component of functional hyperemia has not yet been fully investigated. Previous studies have shown that endothelium-dependent propagated "retrograde" vasodilation from capillaries to arterioles can occur in the brain (Iadecola, Yang, Ebner, & Chen, 1997; Longden et al., 2017). The timing properties of this vasodilation at the level of diving arterioles (Silva & Koretsky, 2002; Tian et al., 2010; Uhlirova et al., 2016) and surface vessels (B. R. Chen, Bouchard, McCaslin, Burgess, & Hillman, 2011) is consistent with its retrograde nature.

We previously showed (Fig 7) that selective light-line disruption of endothelial function across a surface arteriole diminishes functional hyperemia in upstream branches of this surface arteriole, confirming endothelial involvement (B. R. Chen, Kozberg, Bouchard, Shaik, & Hillman, 2014). Fluorescence excitation of FITC-dextran (a non-BBB permeable green fluorescent indicator molecule) causes the release of reactive oxygen species (ROS) that damage the endothelium, hence reducing their vasoactivity. A laser line of blue excitation was therefore used to transect endothelial action in a surface artery during hind-paw stimulus evoked vasodilation. In control experiments (Fig 8) we confirmed that smooth muscle activity was intact in the transected vessel using direct application of sodium nitroprusside, SNP, which releases nitric oxide directly onto smooth muscle cells to initiate dilation. We also showed that that endothelial dependent vasodilation was still intact upstream of the transected section using acetylcholine, Ach, which initiates endothelial-dependent vasodilation. These results not only confirmed endothelial involvement, but also confirmed that alternate mechanisms of upstream vasodilation that don't require an intact endothelial conduit (such as shear-induced flow-dependent vasodilation) are not responsible for the observed changes. This kind of endothelium-dependent propagated vasodilation has been widely observed in the peripheral vasculature. Two distinct mechanisms of vasodilation are generally described – a fast endothelium-derived hyperpolarization (EDH) that can rapidly spread over large distances (>1 mm) along vessels, as well as a slower, more spatially restricted calcium-wave dependent vasodilation involving nitric oxide (NO) and cyclooxygenase (COX) activity (Domeier & Segal, 2007; Figueroa & Duling, 2008; Segal, 2015; Tallini et al., 2007). Endothelial hyperpolarization and the subsequent conducted vasodilation has now been described in the brain *in vivo* (Longden et al., 2017).

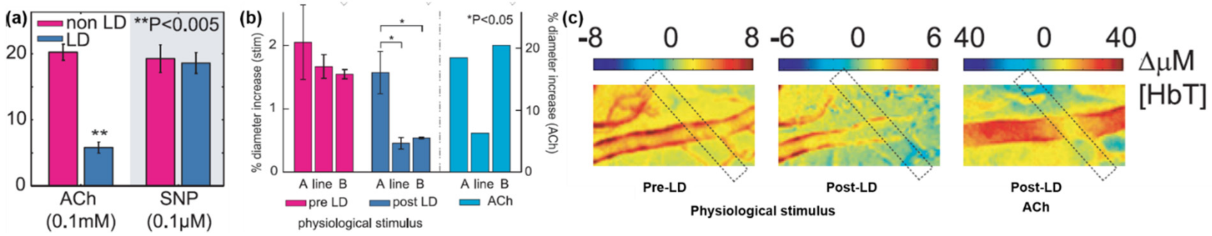

Fig 8. Controls for light-line experiments. (a) Transected section diameter response to Ach (acetylcholine) and SNP (Sodium nitroprusside). (b) Response along the vessel (both sides A and B as well as on the line) to physiological stimuli and ACh. (c) Corresponding Δ[HbT] map response map along the vessel with light line area indicated with the rectangle. (From Chen et. al. 2013)

In this thesis we will use mesoscopic and microscopic imaging techniques to evaluate the contribution of the endothelium to the spatiotemporal evolution of the stimulus-evoked hemodynamic response in the brain. We delve into the dual mechanisms of vasodilation in the brain and attempt to selectively impair each mechanism and observe the effects of each mechanism on hemodynamic responses in the brain. But first, we will discuss the optical imaging tools we use to study blood flow in the brain, which are described next.

2. Optical methods for neurovascular imaging

From an imaging perspective, the full exploration of neurovascular science involves imaging neuronal activity, metabolic activity and blood flow. Wide-field imaging allows for a mesoscopic approach, where blood flow can be measured in surface vasculature and gross tissue parenchyma, and neuronal or metabolic activity can be measured as a conglomerate of different cells (for example, in a population of neurons). This mesoscopic approach has allowed us to ask a wide variety of questions regarding neurovascular coupling, making the nuances of wide-field imaging essential throughout this thesis. The absorption spectra of hemoglobin molecules and the excitation/emission spectra of various fluorophores and the optical interactions between these molecules need to be considered carefully.

2.1 Optical intrinsic signal imaging

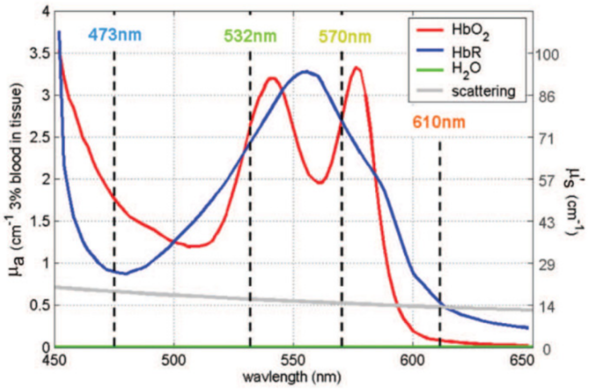

Fig 9. Hemoglobin absorption spectra. Different wavelengths of light quantify changes in oxy-hemoglobin [HbO2], deoxy-hemoglobin [HbR] and total hemoglobin [HbT] due to differential absorption. We usually use 470, 534, and 615 nm Thorlabs LEDs.

Oxygenated and de-oxygenated hemoglobin have different wavelength-dependent absorption spectra (Fig 9). At ~532 nm there exists an isosbestic point where both molecules equally absorb green light. Blue light is preferentially absorbed by oxygenated hemoglobin whereas red light is preferentially absorbed by de-oxygenated hemoglobin. By illuminating live tissue with light at different wavelengths, one can actually calculate the concentration changes in oxygenated hemoglobin, Δ[HbO] and de-oxygenated hemoglobin, Δ[HbR] in the tissue. A simple description of the process is as follows:

When the surface of the brain is illuminated (I_0 – illuminated light intensity) with a specific wavelength of light (λ), the transmission of light through the tissue is determined by the absorption of light by (mostly) hemoglobin (μ_a – absorption coefficient of the tissue at that wavelength) as well as by light scattering. Brain is highly scattering, and allows for some of the light illuminating the tissue to be scattered back to the surface of the brain (I – reflected light intensity). The modified Beer-Lambert law can be used to describe this behavior:

$$I = I_0 e^{-\mu_a X + G}$$

Equation 1

Here, X represents the differential path length, i.e. that distance the average photon travels (after scattering) in the tissue and G represents geometric factors approximating the uncertainty with which light exiting the tissue can be captured by the imaging camera. Relative measurements in time, however, leaves us with:

$$\frac{I_t}{I_{t=0}} = e^{-\Delta\mu_a X}$$

Equation 2

Additionally, changes in the absorption coefficient of brain tissue at different wavelengths is determined by:

$$\Delta\mu_a\,(\lambda) = \epsilon_{HbO}(\lambda)\Delta[HbO] + \epsilon_{HbR}(\lambda)\Delta[HbR]$$

Equation 3

Hence, by illuminating the surface of the brain with diffuse light of two different wavelengths, by measuring the temporal changes in the reflected light, one can measure changes in Δ[HbO] and Δ[HbR]. Separately, these two represent changes in the oxygenation of the brain, but when added together, Δ[HbR]+ Δ[HbO]= Δ[HbT], we are able to obtain changes in the concentration of total hemoglobin in the brain. Total hemoglobin, by itself is a measure of changes in the total blood volume of the brain (assuming a constant hematocrit, or concentration of blood cells in the blood). Taken together with Δ[HbR] and Δ[HbO], however, Δ[HbT] can appropriately be also used as a surrogate for brain blood flow. To obtain these measurements however, one must simultaneously (or near-simultaneously) be illuminating the surface of the brain with different wavelengths of light and separately collecting the data from the reflected light. One practical approach, developed in our lab is described next.

2.2 Multispectral hemodynamic imaging

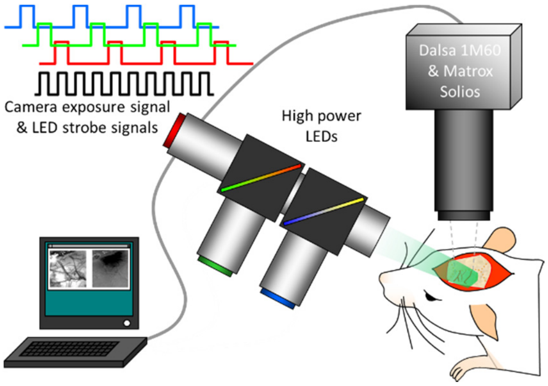

Fig 10. MS-OISI system. High Power blue, green and red LEDs are strobed on the surface of the rodent cortex; the reflectance signal is captured with the imaging camera. Each successive frame of the camera captures a different LED signal, which are all driven by the camera exposure signal.

As described previously, our lab developed a multispectral optical intrinsic signal imaging (MS-OISI) system to capture changes in Δ[HbR] and Δ[HbO] at high sampling rates. High power blue, green and red ThorLabs LEDs are strobed on the surface of the brain in sequence, locked to the exposure signal of the imaging camera (Fig 10). The exposure signal of the camera is read into an Arduino and hardware interrupts are used to sequentially send TTL logic ("1" and "0") signal to strobe the LEDs. This configuration allows us to effectively collect three channels with blue, green and red reflectance data at 1/3rd the frame rate of the imaging camera. The LEDs themselves are co-aligned using dichroic filters and focused onto the brain using appropriate lenses in order to uniformly illuminate the surface of the brain. A custom-written acquisition code in LabWindows (SPLASSH) can be used and adapted to different imaging cameras to use our MS-OISI system (Sun, Bouchard, & Hillman, 2010).

2.3 Speckle-flow imaging

While MS-OISI can be used to effectively look at changes in Δ[HbR], Δ[HbO] and Δ[HbT], which taken together, represent simultaneous changes in blood flow and blood volume, one criticism of hemodynamic imaging is that it does not *directly* measure changes in brain blood flow. While laser Doppler can be used to measure blood flow changes – it has extremely limited spatial resolution. Another approach involves using speckle flowmetry. The diffuse reflection of monochromatic laser light from scattering tissue results in a "speckly" intensity pattern that can be captured with an imaging camera. In static samples, the speckle pattern remains constant, but in samples with moving scattering particles, the speckle pattern changes. With respect to blood flow, blood cells themselves act as these scattering samples in the surface vasculature of the brain. Hence, due to the blood flow in the brain surface vasculature, the speckle pattern obtained from the brain is constantly changing. Therefore, one can quantify the "blur" in the speckle pattern as a metric of brain blood flow:

$$K = \sigma/\mu$$

Equation 4

Here, K quantifies the standard deviation (σ) of the signal normalized to the mean value of the signal (μ), i.e. 0<K<1, where 0 represents a complete lack of flow. These can be calculated temporally (over a certain number of camera frames) or spatially (over a certain number of camera pixels) to obtain "temporal speckle" and "spatial speckle" respectively(Dunn, 2012). Temporal speckle allows for flow calculations with high spatial resolution, whereas spatial speckle approximates temporal changes in blood flow more precisely. A direct calculation of flow can also be done (Dunn, Bolay, Moskowitz, & Boas, 2001):

$$K = \ \sigma/\langle I \rangle = \left(\frac{\tau_c}{2T}[1 - ex\,p\left(-\frac{2T}{\tau_c}\right)]\right)^{1/2}$$

Equation 5

Here, the exposure time of the imaging camera (T) as an added variable, allows us to calculate τ_c, the correlation time, which is inversely and linearly proportional to the mean velocity of the scattering particles. Our MS-OISI system can easily be adapted to include speckle flow by adding a fourth imaging channel where instead of an LED, a coherent laser source is strobed on the surface of the brain – hence simultaneously observing hemodynamics and blood flow in the brain. An example (Fig 11) of a processed speckle image (K, temporal speckle), shows dark vasculature (veins are arteries) over the lighter parenchyma, clearly demonstrating blood flow in the vasculature.

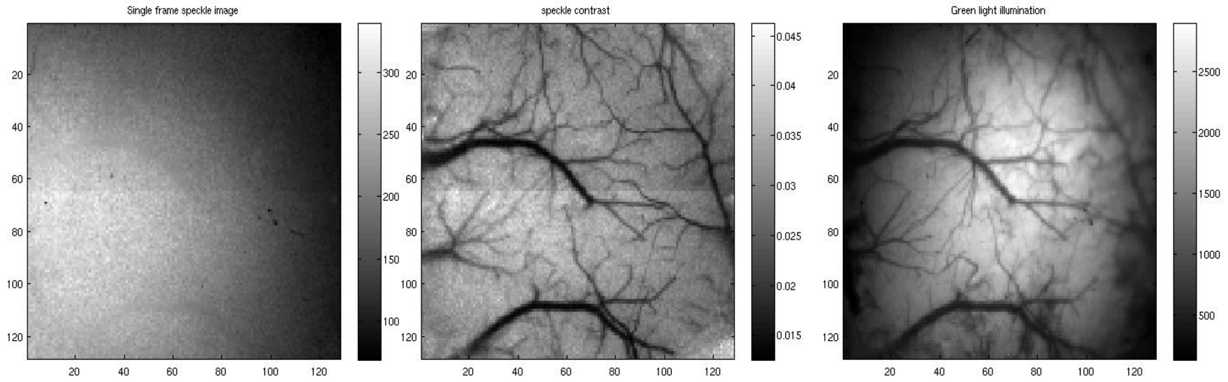

Fig 11. Speckle flowmetry. Left: Raw speckle image. Middle: Processed temporal speckle image (K) demonstrating active flow in the surface vasculature. Right: Green reflectance image shows the same surface vasculature.

While speckle flowmetry could allow one to directly calculate changes in blood flow in the surface vasculature, several parameters, including the exposure time of the camera, the pixel size of the camera, the imaging lens and the laser speckle wavelength all affect the measured signal. In practice, speckle flow ultimately is still an indirect measure of blood flow.

In the context of neurovascular coupling, increases in Δ[HbT] are associated with increases in Δ[HbO] and decreases in Δ[HbR], directly suggesting increased blood oxygenation due to vasodilation and increased flow. Changes in blood flow are directly related to changes in vascular resistance, i.e. Δ[HbT], and must be associated with increases in Δ[HbO], due to an increased rate of tissue oxygenation. Hence, the speckle flow signal usually matches the Δ[HbT] signal. Nevertheless in situations of abnormal blood flow (changing hematocrit, systemic blood oxygenation etc.), as well as a validation of hemodynamic measurements, speckle flowmetry can serve as a valuable tool for measuring blood flow in the brain.

2.4 Imaging fluorescent indicators of neural activity

While several groups have studied neurovascular coupling in the brain and the mechanisms underlying changes in coupling, few studies have controlled for changes in the underlying neuronal activity. The previous gold standard for simultaneously measuring changes in neuronal activity and blood flow was through electrophysiology, where recording electrodes are inserted into the brain and neuronal activity is recorded alongside hemodynamic imaging of the brain.

This approach works well – one study found that apparent changes in neurovascular coupling and the stimulus-evoked hemodynamic response due to a hypercapnic challenge was actually directly related to underlying changes in neuronal activity(Kennerley et al., 2012). However, there are a few disadvantages to this approach. Firstly, inserting recording electrodes into the brain most certainly damages brain vasculature. While care is usually taken to avoid damaging the surface vasculature, the diving vasculature and capillaries around the recording electrode are often damaged, changing the nature of blood flow to the recording region. In addition, while hemodynamic imaging allows us to look at changes in blood flow across large areas of the rodent cortex, electrode recordings are limited to specific regions of the brain. An exciting alternative approach is to use fluorescent indicators of neuronal activity – a non-invasive approach that allows for simultaneous imaging of both neuronal activity and hemodynamic changes. While most imaging studies of neuronal activation are done at the microscopic scale, these changes can also be measured at the mesoscopic level. Over the years, several approaches to imaging neuronal activity have been intensively researched, and are summarized below.

2.4.1 Voltage sensitive dyes

With electrophysiology, changes in neuronal activity are often quantified with local field potentials (LFP) and multi-unit activity (MUA). Fundamentally, both signals measure changes in neuronal electrical activity, i.e. changes in voltage. Commonly available voltage sensitive dyes (VSDs) include the ANEP dyes (di-4, di-8-ANEPPS) and RH237. While these dyes are have fast response times, the signal to noise ratio is often quite low, making their *in vivo* use difficult. The ANEP dyes are ratiometric, i.e. their excitation and emission spectra change as a function of voltage. An appropriate calibration of voltage changes hence requires measuring changes from two different fluorescence channels. In addition, as with any fluorophore, changes in blood flow in the brain will contaminate the measured fluorescence signal. Finally, the ANEP dyes also have poor penetration through tissue, since they are designed to get “trapped” inside cells once they enter them. These difficulties have precluded the use of VSDs for measuring neuronal activity in the brain. However, they are still commonly used in cardiovascular research to study changes in the electrical activity of heart tissue (Herron, Lee, & Jalife, 2012).

2.4.3 Calcium indicator dyes

Fluorescent calcium indicators are a useful tool for imaging neuronal activity in vivo. These indicators can easily capture super-threshold activity from brain tissue generated during action potentials within neurons. Unlike VSDs – however, they do not provide information regarding subthreshold changes. With calcium indicators, the response time and decay time of the calcium signal become important considerations.

Of the calcium dyes, the Oregon green BAPTA (OGB) AM dye is probably the fastest with a rise time of <50 ms and a decay time half-life in the 100s of milliseconds. The most useful version of the OGB dye is the cell-permeant type, where, similar to the ANEP dyes, after entering a cell, the OGB molecule is altered and trapped within the cell. For practical purposes, OGB is often injected into the brain at various locations at picoliter volumes in order to help the dye reach the tissue of interest. This procedure carries the hazard of damaging the brain tissue, and the drawback of not being able to uniformly stain the tissue to capture neuronal activity from a large area. In addition, OGB and other fluorescent indicators have no specificity for neurons, astrocytes or other brain cells, i.e. mesoscopic imaging of these dyes carries information regarding calcium changes from all stained cells. One could assume, however, that all "fast" calcium changes are resulting purely from neuronal activity, which is likely true. An example of simultaneous hemodynamic and calcium imaging using OGB under stimulus-evoked conditions is shown below (Fig 12). Blue illumination of the *in vivo* rat brain is used alongside a 500 long pass filter on the imaging camera to collect only the fluorescence signal, while green reflectance is concurrently observe hemodynamic changes. A pulsed hindpaw electrical stimulus (.3 Hz, 3 ms), results in repeated, fast changes in calcium activity that are associated with concurrent decreases in green reflectance, indicative of an increase in brain blood flow.

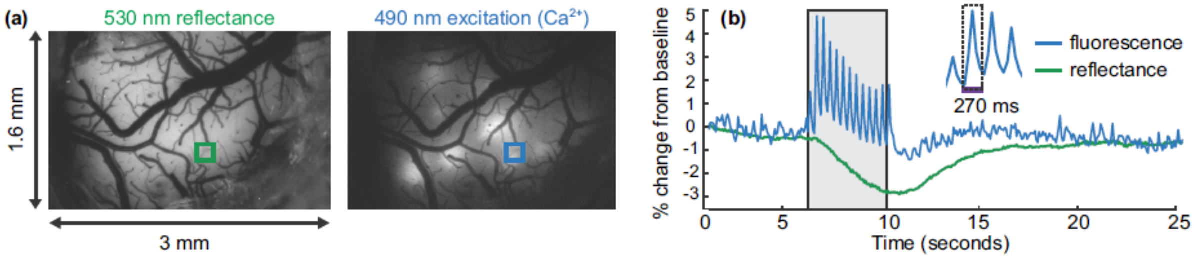

Fig 12. Adapted from (Bouchard, Chen, Burgess, & Hillman, 2009). Simultaneous imaging of hemodynamic activity and calcium fluorescence. (a) Green reflectance image alongside the fluorescence image from the blue channel. Note the non-uniform appearance of the fluorescence signal, resulting from sparse local injections of the calcium fluorophore. (b) Time course of stimulus-evoked responses in the blue fluorescence and green reflectance channels.

One of the difficulties of using imaging dyes is their limited permeability into brain tissue. An alternative approach is to observe intrinsic fluorescence changes in the brain. Changes in neuronal activity result in dramatic changes in metabolic activity – which can be measured by observing changes in NADH and FAD auto-fluorescence. This approach is described next.

2.4.3 Metabolites -- NADH and FAD

As mentioned earlier, the "auto-fluorescence" of NADH and FAD can be used to assess the metabolic state of live tissue. NADH, the reduced counterpart of NAD+ is fluorescent, with peak excitation at 340 nm (UV range) and peak emission at 430-450 nm (blue). NAD+ is not fluorescent. Hence, a decrease in the NADH/NAD ratio, as would occur during increased metabolic demand would manifest as a decrease in measured fluorescence signal as measured with UV excitation. Conventional descriptions of FAD fluorescence describe FAD, the oxidized counterpart of $FADH_2$ as fluorescent with peak excitation at 430 nm (blue) and peak emission at 525 nm (green). $FADH_2$ is not fluorescent. This description, while not inaccurate, appears to inversely equate the chemical properties of NADH and FAD. However, this creates a small misunderstanding of the relationship between NADH and FAD. While "free-floating" NADH is fluorescent and interacts with several enzymes during glycolysis and the Krebs cycle, FAD primarily exists as a cofactor in enzymes involved in redox reactions (Huang, Heikal, & Webb, 2002). Specifically, ~50% of FAD signal fluorescence is derived from lipoamide dehydrogenase (LipoDH) which is found in the mitochondrial enzymes, pyruvate dehydrogenase and alpha-ketoglutarate dehydrogenase (see Fig 13). An additional 25% of the signal is derived from flavoproteins involved in the electron transport chain, while the remaining 25% is derived from enzymes not involved in electron transfer(Kunz & Kunz, 1985). This implies that changes in FAD signal during metabolic activity should almost exclusively be derived from the two mitochondrial enzymes that convert NADH to NAD. Thus, changes in the FAD fluorescence – or rather, changes in the FAD/FADH$_2$ ratio – are directly linked to changes in the NADH/NAD ratio, and can be described by the following simplified reaction scheme (**Fig 13**):

$$FADH2 + NAD^{+} + H^{+} \leftrightarrow FAD + NADH$$

Equation 6

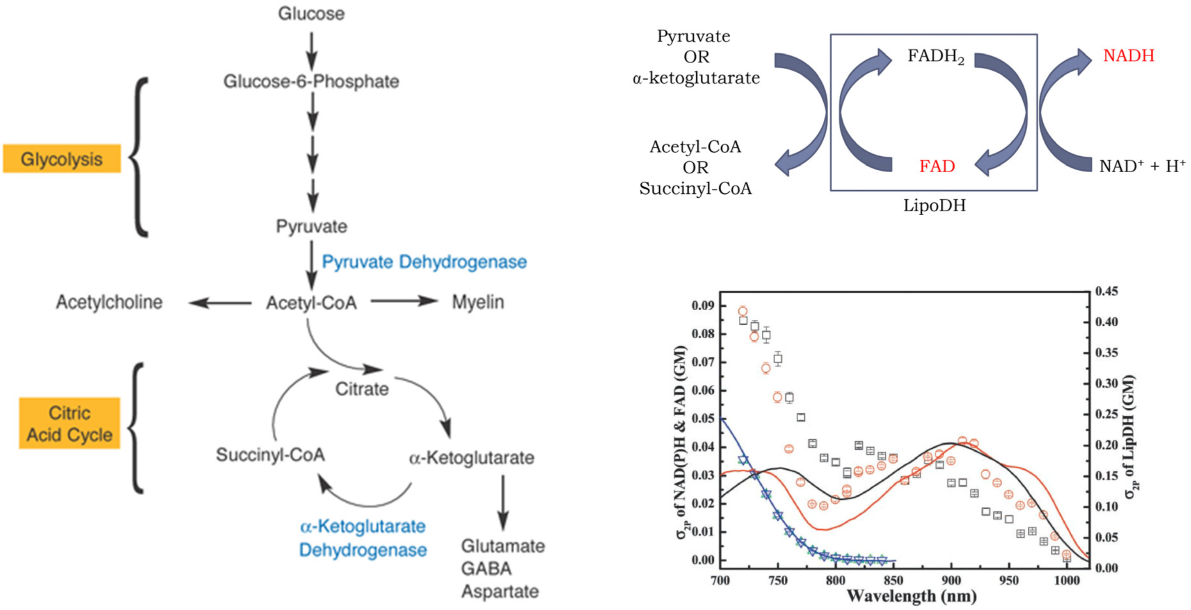

***Fig 13. Properties of NADH and FAD**. (Left) Glycolysis and Krebs cycle, showing the location of two molecules that make NADH and use FAD as co-factors. (Top Right) Reaction schematic showing the direct relationship between the NADH/NAD ratio and the FADH/FAD ratio. (Bottom Right, adapted from (Huang et al., 2002)): Excitation and emission spectra of NADH (blue) and FAD (red) with single photon and two photon excitation. Solid lines indicate NAD and FAD fluorescence with single photon excitation (excitation wavelengths multiplied by 2x), while dotted lines indicate two photon fluorescence at the displayed wavelengths.*

To summarize, increased oxygen consumption drives a decrease in NADH fluorescence, which in turn results in the conversion of FADH$_2$ into FAD and subsequent increase in FAD fluorescence. Importantly, NADH fluorescence indicates changes in glycolysis and oxidative phosphorylation, whereas FAD only indicates changes occurring inside the mitochondria (oxidative phosphorylation). Hence, *increases* in NADH fluorescence, tied to *decreases* in FAD fluorescence are more complex to interpret from a metabolic standpoint – they could be reflecting simultaneous changes in glycolysis and oxidative phosphorylation, i.e., changes in both anaerobic and aerobic respiration. To better understand these changes, lactate, pyruvate and ATP concentrations in the local tissue become important to measure – several groups have worked on building fluorescent indicators for this purpose.

With respect to NADH and FAD imaging, as mentioned earlier, limited UV light penetration of brain tissue makes wide-field NADH imaging nearly impossible, and wide-field imaging generally cannot localize changes in metabolic activity between different cells. In addition, hemoglobin absorption affects the fluorescence of the FAD excitation (blue) and emission (green) signals. Two-photon imaging of these molecules could be used to mitigate some of these issues. The two-photon excitation spectra (**Fig 13**) of these molecules suggests that FAD fluorescence is best measured around ~900 nm whereas NADH fluorescence is highest at lower wavelengths (<750 nm). However, the two-photon cross-section of FAD appears to get much higher at these lower wavelengths, making the spectral disambiguation of these molecules more difficult. The overall wide excitation spectra and low signal-to-noise of these molecules has made imaging of dynamic changes in intrinsic auto-fluorescence in the brain challenging, prompting the need for better metabolic imaging sensors.

2.4.4 Genetically encoded indicators of neural activity

Genetically encoded fluorescent proteins offer a number of advantages over synthetic dyes and endogenous fluorescence. The availability of a wide array of fluorescent proteins with distinct spectral characteristics, as well as the ability to make the expression of the protein contingent on the presence of, for example, specific promoter sequences, facilitate greater versatility in experimental design. There are two approaches to using genetically encoded indicators. The first involves viral injections – which usually take up to two weeks to fully express in the brain. This allows for a much faster production of usable rodents – wild-type animals can be used for experiments within a month of the surgical and injection procedures. It suffers from the same drawbacks as calcium dyes – non-uniform labeling of the tissue and the possibility of tissue damage. The second approach involves creating mouse lines that express these fluorophores in the germline. For neuronal expression, popular promoters include Thy1 (expression in layer II/III and IV excitatory neurons) and Emx1 (expression in >90% of all excitatory neurons). GCaMP, a calcium indicator based on GFP, calmodulin and M13, a peptide sequence from myosin light chain kinase is the most ubiquitous genetically encoded calcium indicator (GECI) in use today. Several variants of the GCaMP molecule, with different baseline fluorescence, kinetics, ΔF/F (normalized change in fluorescence) have been developed over the years (Fig 14). Established Thy1-GCaMP lines are readily available on Jackson Labs and are predominantly used for our experiments. While Cre-Lox can be used to create GCaMP lines driven by different promoters, these lines often take several months to create, yield few mice at a time, and are not stable due to genetic drift.

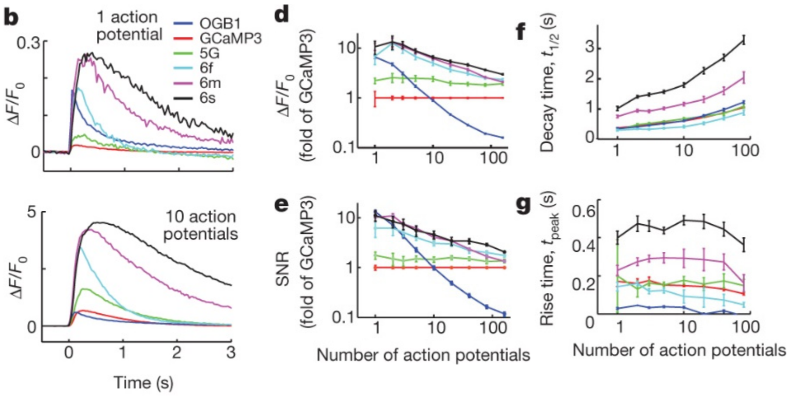

Fig 14. Kinetic properties of different variants of GCaMP and OGB1, adapted from (T. W. Chen et al., 2013). (b) Response time courses of different variants. (d-g): Quantification of various kinetic parameters of the different GCaMP variants.

Alongside GECIs, several groups have worked on genetic indicators of voltage activity (Yang & St-Pierre, 2016). There are several iterations of these indicators – the goal is to make bright indicators with fast response times and good two-photon cross-sections. In addition, for both GECIs and GEVIs, several groups have developed red-shifted indicators that allow one to image deeper in the brain, as well as to allow for simultaneous imaging of calcium activity in two different neuronal populations.

Hence, we can use Thy1-GCaMP6f mice with wide-field imaging to capture neuronal activity during neurovascular coupling. An important consideration is the signal-to-noise ratio of the wide-field fluorescence signal, and will be considered in Chapter 4.

3. Exploring endothelial function during neurovascular coupling using MS-OISI in anesthetized rats

A significant portion of my early experiments were conducted in anesthetized rats. In the next few sections, we will explore the experimental paradigms used for my experiments as well as the pros and cons of using rats for neurovascular coupling experiments.

3.1. Background: How to perturb endothelial functionality during neurovascular coupling?

The observation of endothelial dysfunction after light-line disruption and the exploration of endothelial mechanisms of vasodilation in peripheral vasculature prompted us to consider specifically disrupting endothelial function related to the dual mechanism of vasodilation. One study (Bakalova, Matsuura, & Kanno, 2002) showed that both non-selective COX inhibition with indomethacin and COX2 selective inhibition with rofecoxib diminished the hindpaw-stimulus evoked hemodynamic response (Fig 15). Note that at a 0.2 Hz stimulus frequency, the early part of the stimulus-evoked responses seems much less affected than the sustained part of the response, which will re-emerge later.

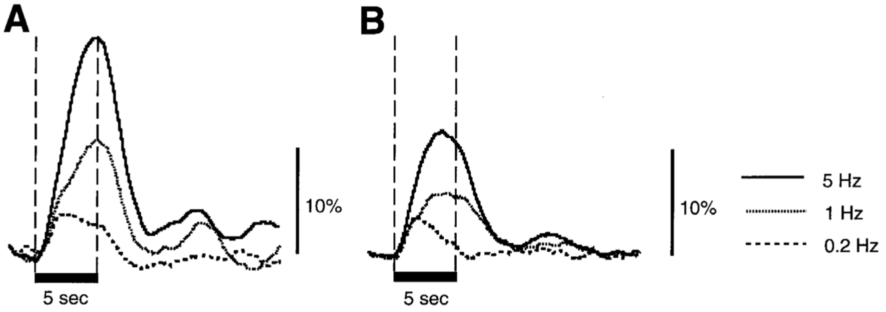

Fig 15. Adapted from (Bakalova et al., 2002) Effect of indomethacin on stimulus-evoked cerebral blood flow in the anesthetized rat. (A) Normal blood flow responses for a 5 second hindpaw stimulus at different stimulus frequencies. (B) Reduced blood flow responses after indomethacin administration.

The clinical relevance of the action of rofecoxib on cerebral blood flow prompted us to search for clinically used pharmaceutical agents that could affect neurovascular coupling. We found ketorolac, which is a non-selective non-blood brain barrier permeable (Mroszczak et al., 1987; Rice, Lloyd, Bullingham, & O'Sullivan, 1993) COX 1, 2 inhibitor used clinically to manage severe acute pain(Buckley & Brogden, 1990). We also use enalaprilat, an angiotensin-enzyme inhibitor (ACEi) that leads to the production of bradykinin, a putative EDHF (factor) to ascertain the effect of changes in endothelial hyperpolarization on the hemodynamic response. Enalaprilat is also a non-BBB permeable drug, hence its action is similarly limited to the vasculature.

3.2 Methods: Anesthetic choice, surgical preparation, imaging windows and stimulus-evoked activity.

For several years, the standard experiment for studying neurovascular coupling *in vivo* in rodent models involved using anesthesia. Choices of anesthesia during imaging included isoflurane, alpha-chloralose, ketamine and urethane, with each anesthetic offering advantages and disadvantages. While isoflurane and ketamine are short-acting, hence tightly controllable, their dramatic effects on underlying neuronal activity in the cortex often precluded their use to conduct neurovascular coupling studies. Urethane allows for a long-term surgical plane depth of anesthesia, and has a much less dramatic effect on neuronal activity. However, it is a carcinogen and can have strange effects (Prakash et al., 2007) on neurovascular coupling, and is therefore infrequently used. Alpha-chloralose is a sedative that does not provide “surgical plane” anesthesia. However, after performing surgeries under isoflurane, animals can be switched to a continuous infusion of alpha-chloralose and subsequently used for imaging studies. The ability to control the depth of anesthesia by manipulating infusion rates, and the limited effect of chloralose anesthesia on neuronal activity in the brain allowed it to become a popular anesthetic of choice in several imaging studies. Importantly, under anesthesia, rodents lose the ability to regulate temperature and cardiovascular function.

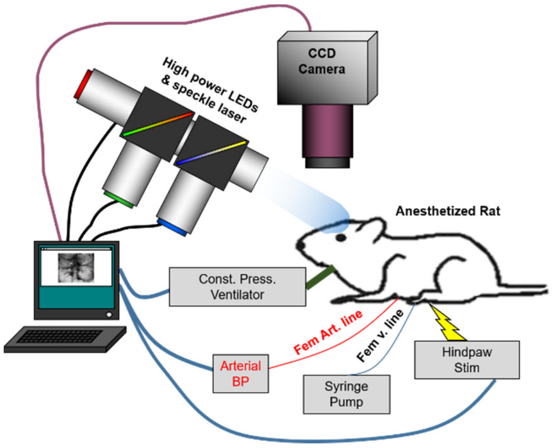

Fig 16. MS-OISI in anesthetized rats. High power LEDs are synchronized to the exposure signal of a CCD camera and strobed on the exposed cortex to collect reflective images of the pial surface (2x2 binning, 60 fps / 4 channels). Data input and output are synchronized to camera exposure start time. A NI-DAQ board is used to monitor physiological data and for stimulus signal generation.

Hence, for our imaging studies, rats were artificially ventilated using a constant pressure ventilator. Blood pressure was monitored continuously via a femoral arterial line in order to adjust anesthetic depth, as well as to monitor pharmacological effects on the blood pressure of the animal. A femoral venous line was used to deliver a continuous infusion of alpha-chloralose and intravenously deliver ketorolac and enalaprilat to the animal. Another standard animal preparation technique involves using full-thickness craniotomies. Here, the skull above the region of interest, in this case the somatosensory cortex, is removed using a dental drill. In rats, the thickness of the dura prevents adequate visualization of the cortical surface, hence the dura is carefully resected. To re-establish the pressure system of the cortex, a glass coverslip is sealed with artificial cerebral spinal fluid (ACSF) using dental acrylic.

For our imaging studies (Fig 16), Sprague-Dawley rats were initially anesthetized with 3-4% isoflurane. A thoracotomy was performed in order to artificially ventilate the animal. Femoral arterial and venous lines were placed on the left side as described. The animal was secured in a stereotax and the skin and connective tissue over the dorsal surface of the skull were resected. A craniotomy and durotomy were performed over the left somatosensory cortex and a glass coverslip was sealed with ACSF. The anesthesia was switched from isoflurane to alpha-chloralose during imaging. Stimulus electrodes were inserted into the right hindpaw. A 12 second stimulus of 1.5 mA amplitude, 0.3 ms duration was applied at a frequency 3 Hz. The imaging itself involves strobing LEDs of different wavelengths onto the cortical surface time-locked to each successive frame of a standard CCD camera. The camera used here (Dalsa Pantera 1M60) captures 512x512 12 bit images at 45-60 frames/sec, i.e. each channel – blue, green and red is captured at 15-20 fps.

Two of the three imaging channels can be used to convert the raw reflectance data into changes in oxygenated hemoglobin [HbO], deoxygenated hemoglobin [HbR] and total hemoglobin [HbT] as described previously (Bouchard et al., 2009).

3.3. Results: Ketorolac and enalaprilat have different effects on hemodynamic responses.

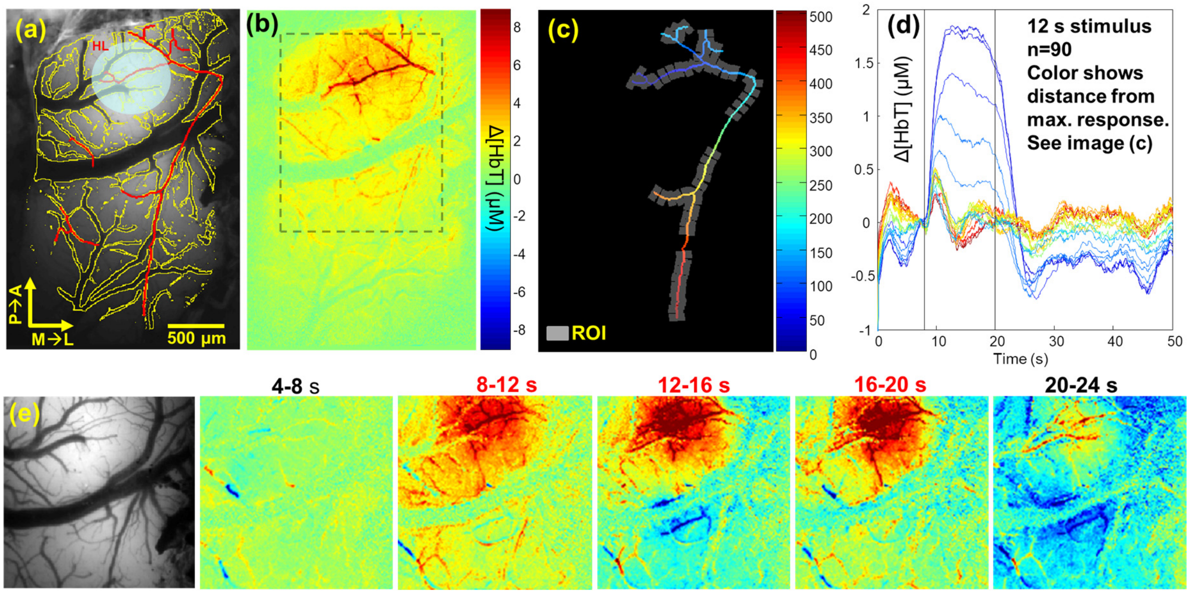

Fig 17. ***Spatio-temporal properties of the HbT response*** *(a) Exposed unilateral somatosensory cortex under 534 nm light illumination, depicting hindpaw region with an oval. Automated segmentation of all vasculature shown in yellow. Skeletonization of arterial trees in red. (b) Averaged Δ[HbT] map over the stimulus period (12 s). Shaded box is expanded in (e). (c) MATLAB function,* ***bwdistgeodesic,*** *used to calculate distances along responding pial artery from point of maximal Δ[HbT] amplitude. Equally spaced ROIs (10 pixels along the vessel, 20 pixels in width) shown in gray. ROIs rotated along vessel orientation (to allow quantification of vessel diameters via FWHM technique). (d) Averaged Δ[HbT] distance dependent response to 12s hindpaw stimulus. (e) Sequence of ΔHbT maps (hindpaw stimulus 8 – 20 seconds) showing initial long-range dilation of pial arteries (arrowhead). Residual hyperemia after vasodilation is more localized.*

A 12 second electrical stimulus was administered to the right hindpaw of the anesthetized rat. The average HbT response over the stimulus period, as well as the evolution of this response is shown in **Fig 17.** To properly analyze the spatio-temporal properties of this response, I segmented the vasculature in the somatosensory cortex using a custom built automated algorithm in MATLAB. I then manually isolated arterial trees supplying the cortex and skeletonized them in MATLAB. The region along the arterial tree with the maximal [HbT] response was considered to be the center of the hindpaw region. ROIs were automatically selected at specific distances along the arterial tree away from the center and aligned to be perpendicular to each arterial segment in order to properly sample changes in blood volume along the surface arteriole.

In the central region of maximal HbT activity, the HbT signal rises quickly before reaching a plateau for the duration of the stimulus before returning to baseline. As we travel away from this center, along the arterial tree, the sustained nature of the HbT response decreases quickly as compared to the initial increase, resulting in a visibly biphasic response. Towards the periphery of the hindpaw region, along the arteria tree, no sustained HbT response is observed, whereas the initial increase in HbT remains. Note that this peripheral region is located outside the hindpaw region, where stimulus-evoked neuronal activity in this region should not occur, and therefore cannot account for the peripheral HbT response. Based on previous results, we hypothesized that the initial, fast increase in hemodynamic activity in the brain is driven by fast, long range EDH-dependent vasodilation, while the sustained phase of hemodynamic activity is maintained by Ca^{2+} mediated localized increases in COX activity. Based on this hypothesis, ketorolac should have no effect on the peripheral response and should attenuate the central response, while enalaprilat should affect the peripheral response without affecting sustained vasodilation.

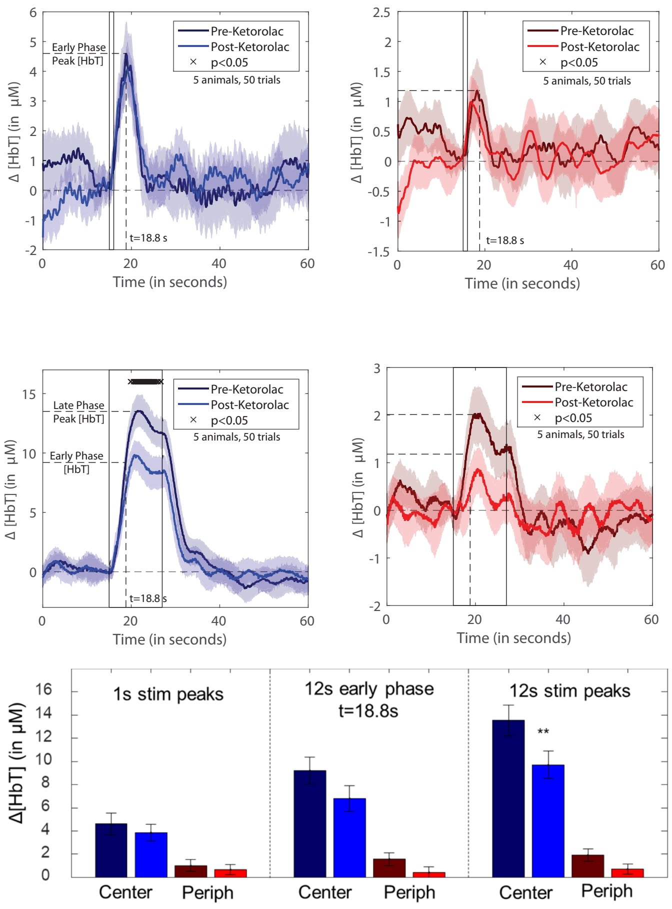

*Fig 18. Effect of ketorolac. Top: 1s responses in the center and periphery. Middle: 12 second responses in the center and periphery. Bottom: Peak responses and the early phase of the 12s response. ** -- p<0.05*

We further hypothesized that stimuli of different durations would allow us to more carefully isolate the initial and sustained phases of vasodilation. The early phase (i.e. EDH, which propagates to the periphery) would manifest most fully in short duration stimuli and in the periphery of the stimulus region, regardless of stimulus duration. Long duration stimuli would allow for the manifestation of the sustained phase of vasodilation, which would be driven more prominently in the center of the stimulated region. Ketorolac (**Fig 18**) has no effect on short duration (1 second) stimuli in the center or the periphery. It diminishes the amplitude of vasodilation in the center for long duration stimuli (12 s stimuli). In the periphery, it reduces a sustained component of vasodilation without affecting the fast initial component; however this is just a trend. I attempted to quantify whether ketorolac affected the initial increase in vasodilation, given that 1 second stimulus evoked responses are unaffected by the drug. The initial phase of the HbT response for a 12 second stimulus would be identical to the initial phase of a 1 second stimulus response. Consistent with this observation, ketorolac has no effect on the initial increase in the HbT response for a 12 second stimulus in the center or periphery.

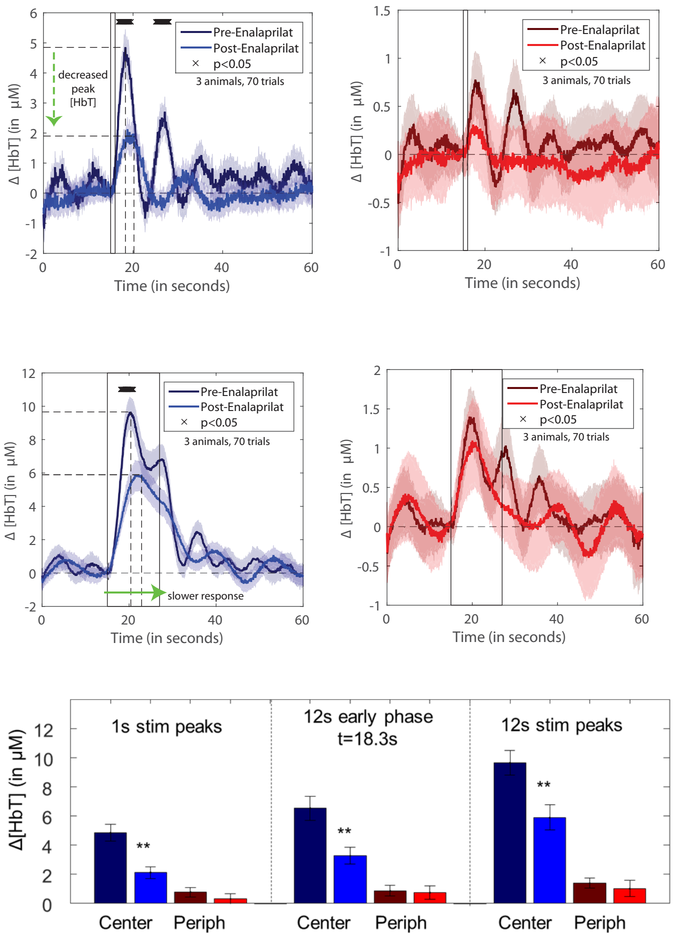

Fig 19. Effect of enalaprilat. Top: 1sresponses in the center and periphery. Middle: 12 second responses in the center and periphery. Bottom: Quantification of peak responses and 12s early phase. **$p<0.05$

Enalaprilat has wholly different effects on the stimulus-evoked hemodynamic response for 1 second and 12 second stimuli (**Fig 19**). Being an ACE inhibitor that increases systemic levels of bradykinin, a putative EDHF, we hypothesized that this increase in overall hyperpolarization of the vasculature would attenuate further hyperpolarization. We don't expect this drug to have an effect on the slow Ca^{2+} wave dependent vasodilation. This appears to be true. Enalaprilat significantly attenuates the 1s stimulus-evoked HbT response in the center and appears to also diminish the peripheral response (trend-wise, but not statistically significant). It also significantly attenuates the initial rise of the 12 second stimulus-evoked response in the center, but doesn't appear to have a big effect on the sustained nature of vasodilation in the central region during the 12 second stimulus. These results are consistent with enalaprilat affecting the nature of fast, EDHF dependent vasodilation in the rat cortex. However, enalapril is a potent vasodilator and significantly reduces the blood pressure of the animal. The mean arterial pressure (MAP) as measured through the femoral line is significantly attenuated after enalapril administration (**Fig 20**). Neither baseline diameters of the surface arteries nor the cerebral blood flow (as measured with speckle flowmetry) changed – suggesting that autoregulation was kept intact. However, this massive change in systemic blood pressure is an important confound that cannot be accounted for with these experiments.

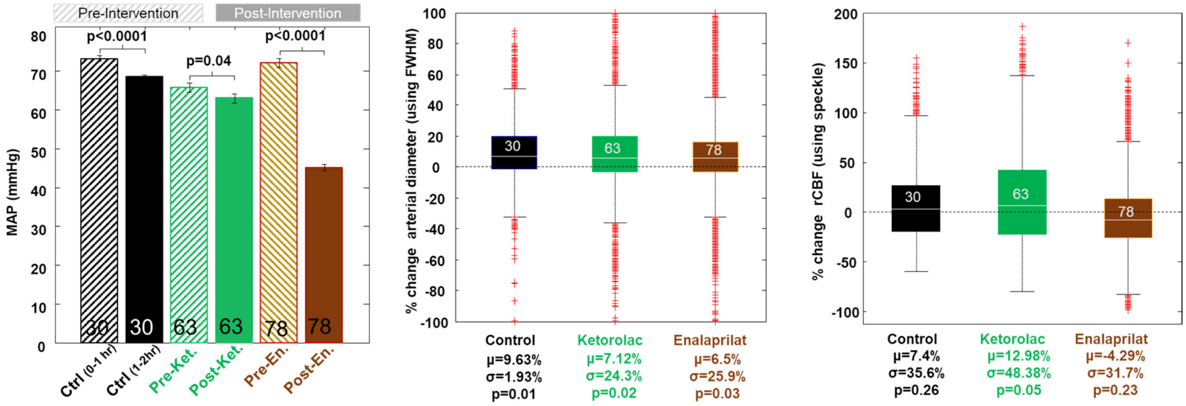

***Fig 20. Effect of ketorolac and enalaprilat on baseline blood pressure, vascular tone and blood flow**. Left: Changes in mean arterial pressure as measured through the femoral arterial line. Middle: Changes in baseline surface artery diameter in the hindpaw region using full-width half max (FWHM) measurements. Right: Changes in cerebral blood flow measured with speckle flowmetry.*

3.4. Additional results: Hemodynamic oscillations and the effect of calcium channel blockade.

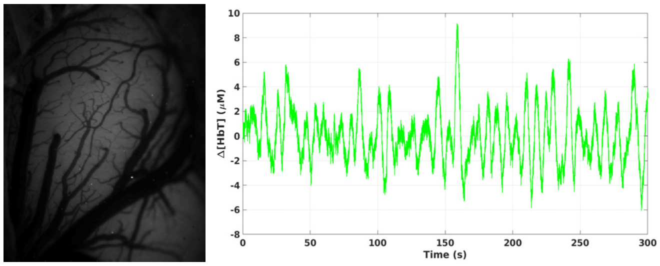

Fig 21. Hemodynamic oscillations in the anesthetized rat. Left: Green reflectance image of the exposed somatosensory cortex (over the hindpaw region). Right: Δ [HbT] over 5 minutes of resting state hemodynamic activity.

In our experience, hemodynamic oscillations occur often in anesthetized rats under urethane and alpha-chloralose anesthesia. These slow, sinusoidal hemodynamic oscillations (SSHO), occur around 0.1 Hz, and are large oscillations with amplitudes comparable to the hemodynamic response of sensory stimuli. They have been observed *in vitro*, and *in vivo* in several different species, and in several different organ systems. While several different hypotheses exist regarding the nature and origin of the vascular oscillations, calcium activity and oscillations within endothelial cells and smooth muscle cells are crucial to the process. An example of these oscillations from a rat under alpha-chloralose anesthesia demonstrates the surprisingly consistent periodic nature of these oscillations.

While these oscillations served as a hindrance for my experiments with ketorolac and enalaprilat, often reducing the amplitude of stimulus-evoked hemodynamic responses, a series of experiments I conducted helped us better understand the nature of the oscillations and their relationship to stimulus-evoked hemodynamic responses in the rat. These experiments were inspired by the study of delayed cerebral ischemia (DCI),after subarachnoid hemorrhage (SAH).

3.4.1. Calcium channel blockers and subarachnoid hemorrhage

Aneurysmal subarachnoid hemorrhage (aSAH) affects 30,000 Americans each year (Bederson et al., 2009). This only accounts for about 5% of all strokes, but causes a disproportionate amount of mortality and morbidity. One-third to one-half of patients die within the first month. A major complication after aSAH is vasospasm or delayed cerebral ischemia, which accounts for 50% of all deaths. Vasospasm is the main cause of secondary brain injury after aSAH, and is classically considered a disorder of the large cerebral arteries. It's usually detected on cerebral angiography 3-10 days after aneurysm rupture, and is associated with multiple ischemic lesions and focal neurological deficits (Rabinstein, Weigand, Atkinson, & Wijdicks, 2005). Nimodipine, a calcium channel blocker, was found to reverse large vessel spasm and modestly improve outcomes (Pickard et al., 1989). However, these outcomes are not actually associated with reversal of large vessel spasm itself(Allen et al., 1983). Therefore, terms like delayed cerebral ischemia or delayed ischemic neurological deficits are now preferred. In addition, in contrast to nimodipine, nicardipine, a related calcium channel blocker, also improves large vessel vasospasm, but fails to improve outcomes in patients with DCI secondary to aSAH. There is also evidence that aSAH leads to microvascular pathology. However, there is limited *in vivo* evidence of microvascular dysfunction after SAH. Using our MS-OISI imaging system in anesthetized rats, we set out to look at the effects of aSAH on neurovascular coupling, as well as the effects of nimodipine and nicardipine on normal animals and animals with aSAH.

The model we used for inducing aSAH involved injecting arterial blood into the fourth ventricle of the rat, and then imaging the animal a few days later. One of the major problems with this approach is that the injection procedure drains a significant amount of CSF from the brain while also significantly reducing intracranial pressure (ICP) due to drainage from the injection site. This is a rather important confound – the ICP is important for both blood flow autoregulation and affects blood flow changes due to neurovascular coupling.

Despite the issues with the model, the effects of nimodipine and nicardipine on neurovascular coupling and resting blood flow in control animals were striking. Firstly, these drugs have complex effects on resting blood pressure and cerebral blood flow. An example of this effect in two different animals with the two drugs is shown below (Fig 22):

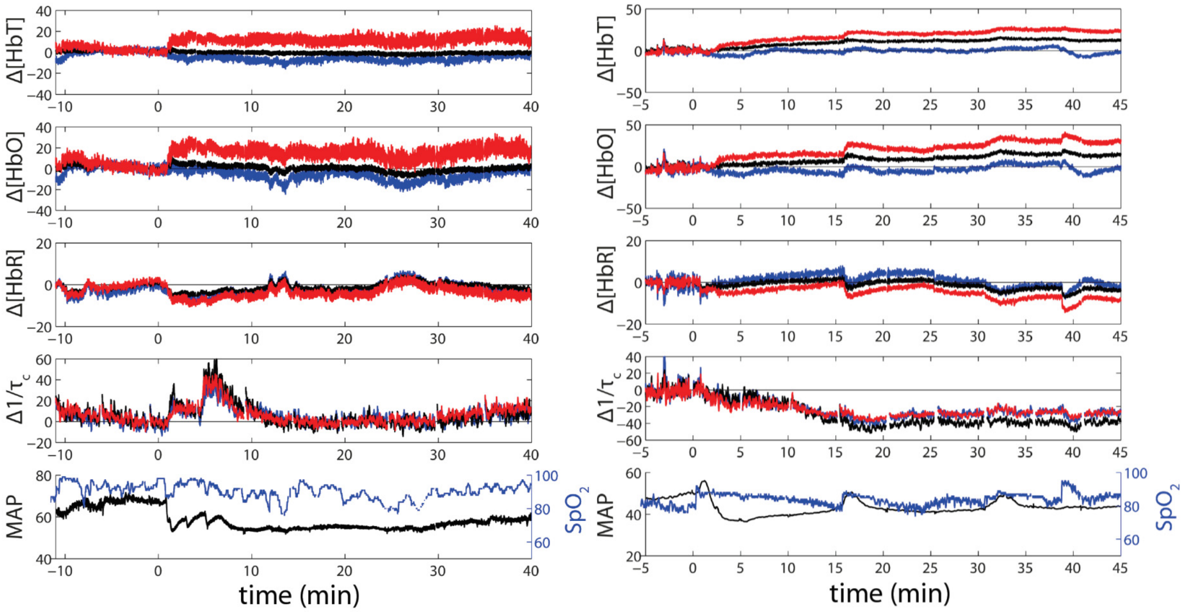

Fig 22. Effects of nimodipine (left) and nicardipine (right) on baseline hemodynamics, blood flow, blood pressure and systemic oxygenation. Hemodynamics and speckle flow measurements from an artery, brain parenchyma and a vein are shown. Drugs are administered intravenously at t=0 minutes.

Generally speaking, both calcium blockers decrease blood pressure, which leads to an increase in arterial blood volume (HbT). Blood flow initially increases with nimodipine administration, and decreases with nicardipine administration – speaking to the complicated role cerebral autoregulation plays in maintaining cerebral blood flow. The effects on parenchymal and venous blood volume are more difficult to comprehend, but what is clear, however, is that both drugs have non-trivial effects on the systemic and cerebral vasculature. Next, we look at changes in hindpaw stimulus-evoked neurovascular coupling before and after administration of these drugs.

To account for the effects of vascular oscillations on stimulus-evoked hemodynamic responses, one approach involves observing Δ[HbT] in arteries in the “responding region”, i.e. an artery that supplies the hindpaw region, and comparing it to hemodynamic changes in a “non-responding” artery. While one might assume that averaging activity across several different trials should markedly diminish the contributions of baseline oscillations, in reality, the superposition of these oscillations often result in an averaged response signal that appears to show significant hemodynamic changes. Hence, comparing changes across the two different arterial beds allows one to discern true stimulus-evoked hemodynamic changes from the contribution of baseline oscillations to the signal.

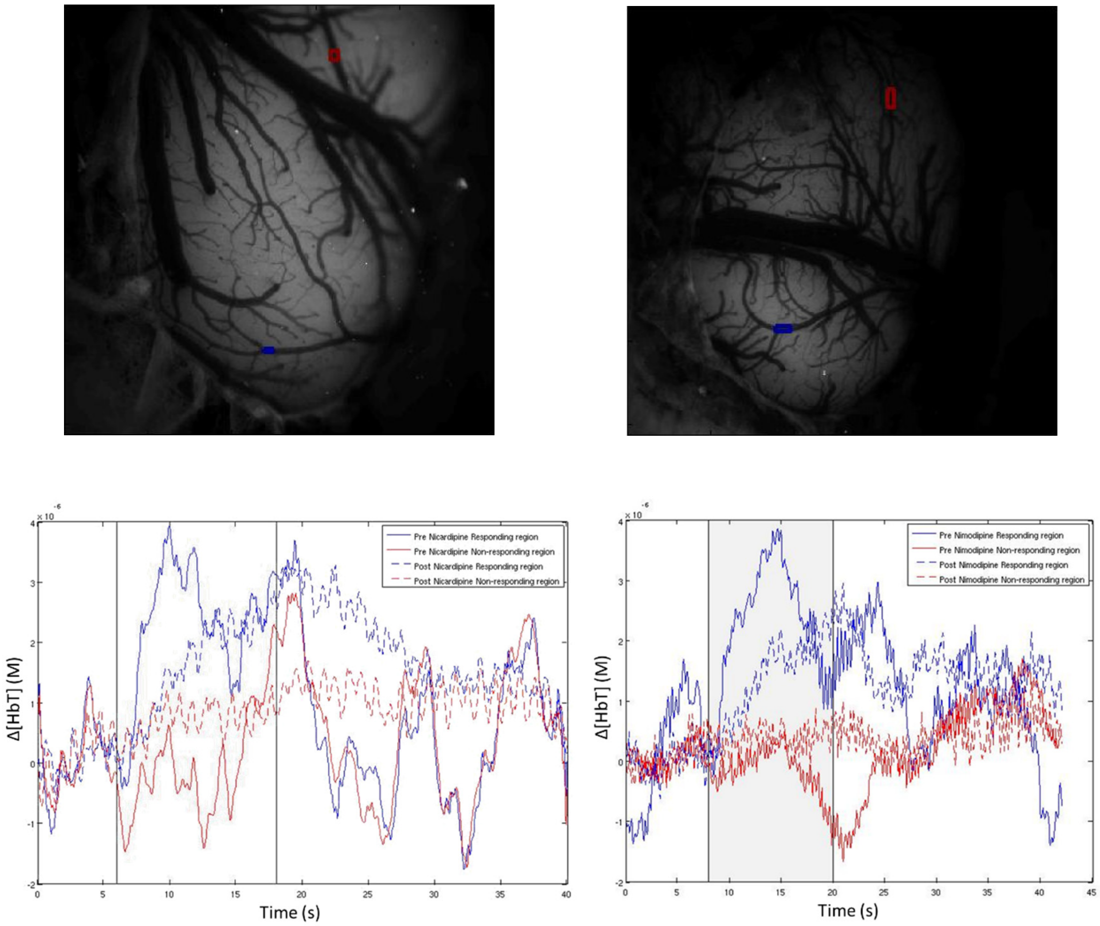

Fig 23. Effects of nicardipine and nimodipine on neurovascular coupling. Top: Arterial ROI selections in the responding (blue) and non-responding (red) arterial regions in two different animals administered nicardipine (left) and nimodipine (right) respectively. Bottom: Superimposed responses from the responding and non-responding arterial ROIs before and after administration of nicardipine (left) and nimodipine (right), respectively.

For both the calcium channel blockers and enalaprilat, there are significant changes in the blood pressure of the animal that is associated with a slower rate of increase of the hemodynamic response. While this change in hemodynamic response rise time could certainly be related directly to the blood pressure change, the resulting decrease in vascular tone and subsequent inability of the vasculature to change tone quickly, it also occurs after a hypercapnic challenge and in our own experiments involving light-dye mediated damage of the surface vasculature (Fig 24).

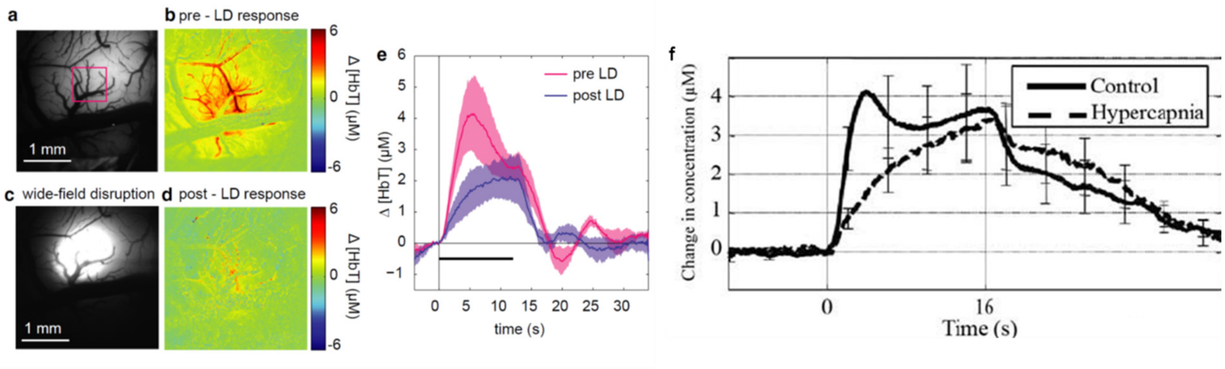

Fig 24. The hemodynamic response before and after wide-field light-dye treatment, adapted from(B. R. Chen et al., 2014) a, grayscale image of the exposed cortical surface (534 nm-centered reflectance). b, Pre-light-dye treatment functional map showing total hemoglobin (Δ[HbT]) "peak" response relative to baseline averaged over 4 to 6 seconds after stimulus onset (average of N=5 runs, 1 rat). c. Image showing the blue light used for wide-field light-dye treatment (~1 mm in diameter). d, Post-light-dye Δ [HbT] functional map (average of N=5 runs, 1 rat). e, Pre and post-light-dye Δ[HbT] time-course response to 12 seconds of stimulation averaged over n=7 rats, runs=5 per rat per condition, responses averaged per rat. f, Replicated from (Kennerley et al., 2012) – hemodynamic responses pre- and post- hypercapnia in the anesthetized rat.

With the hypercapnic challenge, the change in the blood flow response was attributed to a change in the underlying neural activity (Kennerley et al., 2012). In contrast, our light-dye experiments showed that the change in hemodynamic response was not associated with a change in neuronal activity as measured with electrophysiology.

In all of these cases (enalaprilat, calcium channel blockers, hypercapnia, light-dye), with long-duration stimuli, the hemodynamic response after the perturbation, towards the end of the stimulus, matches the control hemodynamic response. That is, the sustained plateau of the hemodynamic response is unaffected in these conditions, whereas the initial rate of change in the hemodynamic response is dramatically altered. Alternatively, with indomethacin and ketorolac, it appears that the overall amplitude of the hemodynamic response, including the sustained plateau, is significantly diminished. These findings set the stage for our discovery of a two-component hemodynamic response that can be pharmacologically altered, and will be discussed in depth in Chapter 5.

As alluded to earlier, there were several confounding factors in the experiments, including changing baseline blood pressure, blood flow in the brain and changes in neuronal activity that could be occurring due to the discussed manipulations. Furthermore, anesthetized preparations often change the nature of hemodynamics in the brain, without changing the nature of the underlying neuronal activity, as previously shown (Pisauro, Dhruv, Carandini, & Benucci, 2013). All these results prompted us to consider a better experimental paradigm to study the nature of neurovascular coupling, as well as the contribution of the endothelium to the blood flow response in the brain. It led us to develop a new imaging system, discussed in detail next, that allows for simultaneous measurement of changes in neuronal activity and hemodynamics in the awake behaving mouse.

4. Development of wide-field optical mapping (WFOM) method for simultaneous neural and hemodynamic imaging in awake mice.

I dedicated a significant amount of time to building a system capable of simultaneously capturing neuronal activity and hemodynamics in the awake mouse. I spent several months optimizing the head restraint gear, the animal surgical procedure, the whisker stimulus paradigm and the behavior recording cameras. With the combined efforts of me and Sharon H. Kim, the lab finally fully transitioned from relying predominantly on anesthetized animal preparations to conducting experiments in awake behaving animals.

However, we are not the first group to implement imaging of awake behaving animals in neuroscience. Several groups had previously developed systems for this purpose – initially, the most popular system was developed by David Tank's group. The animal has a small two-photon imaging window (i.e. full-thickness craniotomy with an implanted glass coverslip), is head-restrained and is free to run or sit still on a small floating Styrofoam ball. An optical encoder is used to measure the direction and speed of the ball's movement as a behavioral correlate. The imaging objective is obviously placed a few millimeters away from the surface of the brain, and the system is encased to prevent the imaging light from reaching the mouse's eyes and causing visual stimuli, or worse, damaging the rodent's eyes.

However, to conduct wide-field imaging, the imaging lens is placed several centimeters away from the surface of the brain. Hence, we needed to devise alternative approaches to protect the eyes from light exposure. Additionally, the Styrofoam ball seemed unnecessary and uncomfortable for the rodent. We decided instead to use a transparent circular wheel, where the animal is free to run or walk, based on groups that used a similar approach. In any case, when we started these experiments, there were few groups that were conducting wide-field imaging experiments in awake animals. Now, there are several groups that regularly conduct wide-field imaging in awake animals. In the next few sections, we will explore in depth the choices we made for building our system, as well as results from stimulus-evoked and resting state data collected from these animals.

4.1. Building the WFOM system

4.1.1. CCD vs. EMCCD vs. SCMOS cameras for capturing wide-field neuronal activity.

For our initial wide-field experiments with wide-field FAD or Thy1-GCaMP3 imaging, we used a Dalsa Pantera 1M60 CCD camera. While this camera could capture changes in wide-field fluorescence, it often involves using 4x4 binning on the camera (with 1024x1024) pixels, as well as using long exposure times in order to obtain enough SNR (signal-to-noise ratio) on the camera. However, we aimed to obtain images at high spatiotemporal resolution in order to capture fast changes in neuronal activity.

EMCCD (electron-multiplying charge coupled device) and SCMOS (scientific complementary metal-oxide-semiconductor) cameras are both designed to dramatically increase SNR of low light signals are allow for GCaMP imaging at high frame rates (maximum 30 Hz for EMCCD, >100 Hz for SCMOS cameras) at high resolution (512x512 or 1024x1024 pixels). While at very low light levels, EMCCD is superior to SCMOS, with increasing photon counts, SCMOS cameras are more useful, as seen in Fig 25. For all subsequent experiments, we used an Andor iXon EMCCD camera at 512x512 resolution at 31.22 Hz, with a linear EMCCD gain of 30 to 100. We discovered later that the GCaMP signal was bright enough to exploit the SNR advantage of SCMOS cameras over EMCCD. This allowed us to use a cheaper Andor Zyla camera (~1/3rd the cost), which also allows for frame rates much greater than 30 Hz.

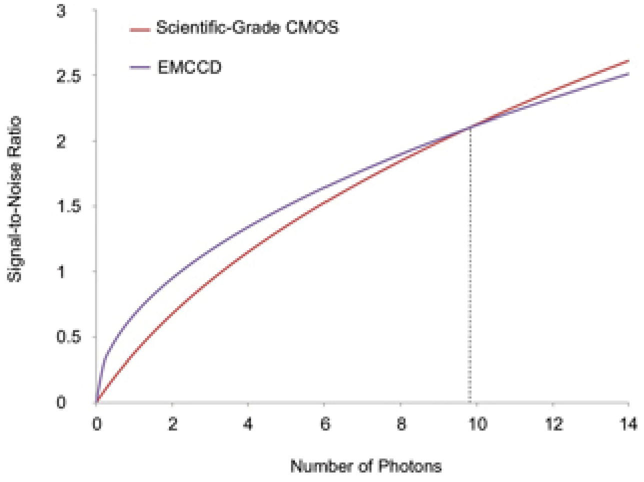

Fig 25. EMCCD vs. SCMOS SNR (replicated from www.photonics.com)

The SPLASSH software developed previously was modified to use the Andor iXon EMCCD camera with the same blue, green and red LEDs. However, a 500 long pass filter is placed in front of the camera, such that the blue channel contains fluorescence images rather than reflectance images. The next step involved developing an animal preparation suitable for wide-field imaging in awake animals.

4.1.2. Thinned-skull preparation for imaging activity over the entire dorsal surface of the mouse cortex.

Our anesthetized experiments often involved performing full-thickness craniotomies in mice over the region of interest, usually above the hindpaw region in the somatosensory cortex, followed by a re-sealing of the cranium with an imaging coverslip. This procedure is rather invasive – it effectively is a decompressive craniotomy that results in brain swelling. The ICP (intracranial pressure) is usually reduced by creating a small hole in the 4th ventricle, allowing for CSF to leak out and reduce acute swelling. However, this is not sustainable for long-term imaging as it causes physical distortion of the brain tissue.

At the time, one group had developed a thinned-skull preparation that involved careful thinning and polishing of the skull to the point that it was near transparent (Shih, Mateo, Drew, Tsai, & Kleinfeld, 2012). They demonstrated successful two photon imaging of the brain through this thinned-skull preparation – and inspired us to consider modifying it for our use. However, this preparation involves making a tiny imaging window for two-photon imaging, and results in a rather fragile skull that needs to be protected. We realized that if it were possible to thin the entire surface of the skull, we would have enough light penetration to conduct our wide-field imaging studies. In addition, we didn't need to excessively thin or polish the surface if we weren't planning on using these animals for two-photon imaging. The concept of being able to image the entire dorsal surface of the mouse brain was exciting – it meant that we could explore a range of phenomena related to neuronal activity and neurovascular coupling in the awake mouse longitudinally. Hence we developed our own surgical procedure. In addition to the surgical preparation of these animals, their breeding, training, and longitudinal imaging procedure is described below:

Breeding: One female mouse is bred with one male at a time. As soon as the female is observed to be pregnant, the male is removed and placed in a separate cage. The female remains alone throughout gestation, during the birth, and rearing of pups. Pups are weaned at day 21, at which time the male is reintroduced into the cage with the female for further breeding. Breeder chow is readily available, and nestlets are placed in the cage at the time pregnancy is noted.

Genotyping and identification: For all mouse lines, pups are genotyped by tail clipping before 14 days of age, preceding the ossification of vertebrae and avoiding pain, eliminating the need of anesthesia. In all cases of tail clipping, a 0.2-0.5 cm piece of tail is snipped using a scissor which is dipped in alcohol and wiped clean using a sterile 4x4 pad between all tail clippings. After completion of the tail clipping, bleeding is controlled with gently applied pressure to the site of excision. Samples are sent out to GeneTyper for analysis (www.genetyper.com). Where possible, we plan to transfer any surplus negative, wild type mice, to other laboratories in the Department of Biomedical Engineering who have a need (and approved protocols) for wild-type mice. Otherwise, unneeded mice are euthanized by CO2 inhalation followed by cervical dislocation. To identify individual animals, we will toe-tattoo the toe pads using a micro tattoo system (Fine Science Tools) which consists of forceps with a hypodermic needle at one end and a small metal cup containing green tattoo paste on the other. By squeezing the forceps together, the needle penetrates the toe, and injects a deposit of green tattoo paste into the animal. This humane method of permanently identifying animals elicits minimal pain, and can be used in mice as early as one day old without the use of anesthesia. Toe-tattooing is done in pups before 14 days of age at the same time genotyping samples are acquired. In all toe-tattooing cases, the animal's toe is cleaned using a sterile 4x4 alcohol pad before injection, and a new 26G1/2 sterilized hypodermic needle is used for each animal.

Awake imaging studies: There are four general stages to these experiments.

1. Pre-operative training (starting at least 2 days before surgery): The study mouse is individually housed in a cage with a Bio-Serv Fast-Trac Mouse Igloo and treadmill for acclimatization. The clearance height of the Fast-Trac treadmill does not allow for the wire top to be placed normally

in the cage. As an alternative, food and HydroGel or DietGel (as a substitute for the water bottle) is placed at the bottom of the cage. On the training days starting at least 2 days prior to surgery, the mouse is handled by a trainer for ~10 minutes or until the mouse moves freely from hand to hand. Training sessions will continue until the animal is comfortable with handling. If the animal is unresponsive to training on two successive days, it is used for acute, anesthetized imaging under a different protocol. Mice are weighed at the beginning of each session and monitored for distress continuously during training.

2. Day of surgery: The surgical preparation is performed using aseptic techniques (see surgical section for details). Animals is weighed, then receive pre-operative analgesia and be induced (if undergoing skull surgery) and maintained with isoflurane or ketamine/xylazine and monitored for depth of anesthesia throughout aseptic surgery to establish a cranial window. After the procedure, the animal is returned to a clean cage and monitored continuously as it recovers from anesthesia.

3. Recovery (1 day to 7 days): The animal is allowed to recover for at least 1 day and up to a week, depending on the health of the animal. If intraperitoneal buprenorphine injections are used, then they are provided every 8-12 hours after surgery for at least 48 hours or longer until normal behavior resumes. In the case of intraperitoneal injections, our plan is to perform surgeries starting in the morning coinciding with a first dose of buprenorphine, followed by second (8-12 hours after the initial dose), third, and fourth doses 8-12 hours apart. If there is any manipulation to the skull, carprofen (5mg/kg) is administered SQ at the time of the surgery, and then every 24 hrs for the next 48 hours. Animals are housed individually, with daily handling and enrichment (via supervised time on the mouse igloo/fast-track). The veterinarians are informed of the animal undergoing post-surgical recovery. The animal is weighed and monitored at least every 24 hours for the 72 hours following the return of the cage to animal facilities. Each time, the animals are inspected for signs of pain, distress or problems with the placed cranial windows. This will include looking for hunched posture, reduced activity, abnormal gait, labored, slow or rapid respiration, poor hydration (sunken eyes or reduced skin elasticity, poor coat, surgical wound swelling, redness, discharge, disrupted sutures, reduced eating or drinking, reduced or excessive

grooming and weight loss. Veterinarians are consulted immediately if these signs of pain and distress are noted for advice on whether analgesics, antibiotics or euthanasia are appropriate. In severe cases, immediate euthanasia with CO2 followed by cervical dislocation is performed and this outcome reported.

5. Awake Imaging: Any restraint and imaging does not exceed 2 hours per session, and the mouse is continuously monitored throughout this period for signs of distress. If significant distress is noted within this period, in the form of excessive vocalizations or movement, the restraint is immediately stopped and no further restraint or imaging is done that day. Depending on the speed of acclimatization of the animal, for the first 1-3 sessions, the restraint period may be shorter than 2 hours and may include the use of water-based reward as positive reinforcement. The animals are imaged 3-5 days a week and weighed at the beginning of each restraint/imaging period.

The utmost care is taken to avoid emotionally distressing the animals during restraint or imaging in order to decrease the chances of confounds to our data, especially those collected to study resting state brain activity. A distressed animal could potentially be undergoing physiological changes such as elevated cortisol levels or heart rate, which in turn could modify the neurovascular coupling and state of the brain. After the animals are removed from the restraint after each imaging session, grain-based treats will be used to help alleviate stress and reward restraint acclimatization.

Thinned-skull procedure: Monitoring and homeostasis during aseptic surgeries: Body temperature is maintained with a homeothermic heating pad with rectal probe (Harvard apparatus, Holliston, MA) during surgery. All animals are examined throughout the surgery to ensure that the level of anesthesia is sufficient to prevent hindpaw reflexes, whisking behavior or corneal reflexes. Heart rate is monitored continuously using a pulse oximeter (MouseSTAT, Kent Scientific), and recorded at least every 15 minutes throughout the surgery. Heart rate is maintained around 600 beats per minute and blood pressure below 120 mmHg (or less than 20%

above their established baseline values). After achieving stable anesthesia conditions, the same rate of anesthesia is maintained throughout the surgery.

Placing cranial windows (for chronic studies): The animal is induced either with ketamine/xylazine or isoflurane. Buprenorphine will be injected IP (0.05- 0.1 mg/kg IP). In cases where a full-thickness craniotomy is planned, Carprofen (5mg/kg is also be given subcutaneously). After no response to firm toe-pinch is observed, the animal is positioned into a sterotaxic frame with blunt, non-rupturing earbars. A pulse oximeter foot-clip (Kent Scientific) is attached to monitor the animal's heart rate and PaO2 levels throughout. Fur on the head is clipped and the skin cleaned using alcohol and iodine/povidine wipe alternated three times, and then injected subcutaneously with 2% lidocaine. A midline incision in the scalp is made and the skin and muscle gently pulled aside, minimizing tissue damage, to reveal the skull. The skull is cleared of membranes by gentle scraping with dry, sterile cottontipped applicators until clean in the area of interest, with at least a 1mm border. Our goal for resting state studies is to image as much of the bilateral, superficial cortex as possible. There are three different procedures that could be performed at this point:

(1) The skull is left intact. Cyanoacrylate is applied to the exposed surface of the skull to seal the bone and prevent regrowth. A custom-made head plate is then be attached to the surrounding skull using dental acrylic and / or cyanoacrylate. The head-plate is have holes that the dental acrylic / glue will flow over to ensure structural integrity. A uniform layer of Kwik-Sil elastomer is then be prepared and applied over the skull to protect it between imaging sessions.

(2) The superficial aspect of the skull is thinned over the region of interest using a sterile dental drill. This is done carefully, and sterile saline drops are applied every 30-60 seconds to cool the area and wash away bone dust. Saline drops also help visualize the brain underneath better, and the visualization of cortical vasculature guides the surgeon to the required thickness of the skull. Some recent reports, which we may follow, have polished the skull surface using autoclaved tin oxide powder and a premade, sterilized dental drill dipped in silicone aquarium sealant leaving a tail-whip (Shih et al., 2012). In this case, the drill bit is prepared and autoclaved. The tin oxide

powder is placed over the skull with a drop of sterile ACSF and the slurry is agitated using the dental drill and tail whip portion of the drill bit to polish the surface. After polishing, cyanoacrylate is applied over the thinned portion. If necessary, a glass coverslip is placed over the thinned skull region for protection, secured using cyanoacrylate. A custom-made head plate with holes is secured to the skull using dental acrylic or cyanoacrylate. The dental acrylic / glue is allowed to fill the holes to provide further structural integrity. Kwiksil is applied to protect the window until and between imaging sessions.

(3) A craniotomy is performed by drilling a circle around the region of interest, while frequently applying saline drops to cool the skull and remove bone dust. When the skull over the region of interest begins to give way, it is pulled off using sterile fine tipped forceps. Sterile Gelfoam soaked in sterile ACSF is applied to the exposed dura mater as needed to stop any bleeding. One or more glass coverslips is placed over the region on top of a drop of sterile ACSF. Dental acrylic (Henry Schein) is applied to the dry surrounding skull and spread with a needle / sharpened swab stick over the glass coverslip while making sure no acrylic gets underneath the coverslip on to the dura. Once secure, a custom-made head plate is secured to the surrounding skull using cyanoacrylate or dental acrylic. The dental acrylic is allowed to fill holes in the head plate to provide further structural integrity. Kwiksil is applied to protect the window until and between imaging sessions.

In all 3 cases, surrounding skin and muscle is positioned around the edge of the dental acrylic and fixation plate, with edges neatly sealed to minimize the possibility of infection. Immediately following cranial window placement, between 0.25 and 0.5 ml saline is given subcutaneously to replace lost body fluids. Once the window is in place, and checked for rigidity and integrity, the animal is allowed to recover under careful supervision to check for signs of pain, distress or hypothermia. A water-filled disposable glove, warmed to around 40 degrees may be placed next to the recovering mouse to provide warming if needed.

4.1.3. Head restrained imaging of the awake, behaving mouse.

An important aspect of head-restrained imaging is the head restraint plate that is implanted on the mouse itself. It has to be biocompatible, light, and non-obtrusive to the mouse, while also significantly diminishing motion artifacts. Most groups use thin, custom-made steel or titanium head plates that are attached to the surface of the skull with super glue or dental cement. However, we figured that the same could be accomplished by a thicker piece of plastic acrylic. There are several advantages that acrylic offers over custom-designed metal head plates. First, acrylic can be laser cut cheaply and within minutes – allowing us to customize head-plates for different animals or different experimental conditions. Second, super-glue, which we use to stabilize the skull surface, is also compatible with acrylic – it allows for welding the acrylic to the surface of the skull, creating an extremely strong bond that cannot be easily created with metal. In fact, with metal head plates, holes and rough surfaces are often created in order to increase the surface area between the metal and the skull, to allow for better stability of the head plate. Finally, a thick piece of black acrylic also helps block some of the light from the illuminating LEDs from the animal's eyes, protecting them from damage.

4.1.4. Experimental set-up for evoking whisker stimulus activity in the awake mouse.

We previously relied on hindpaw and forepaw electrical stimuli to elicit stimulus-evoked changes in neuronal activity and blood flow in the anesthetized rodent. However, this is not feasible in awake rodents – the animals are supposed to be able to move freely while head restrained, and an electrical stimulus, while appropriate in anesthetized animals, is certainly not acceptable for use in awake animals.

Instead, we chose to use a whisker stimulus paradigm. This had successfully been implemented before in awake animals (Takuwa et al., 2011). This group also demonstrated that the stimulus-evoked blood flow response was quite robust and minimally affected by the time of day or amount of locomotion by the animal.

The most common approach to whisker stimuli involves using a whisker "puff" paradigm, where an air puff from a pressurized system is delivered onto the whiskers, hence manipulating them with an air column. However, air puff stimuli are loud and result in "startle" responses in the awake mouse – these are non-physiological stimuli that employ mechanisms of vasodilation distinct from normal mechanisms of stimulus-evoked vasodilation (Bonder & McCarthy, 2014).

In our own experience, air puff stimuli caused significant distress and discomfort in the awake mice, prompting us to consider an alternative, gentler approach.

Given the constraints of our head-restraint system, we felt that the most feasible whisker stimulus paradigm would involve stroking the whiskers of the mouse in a dorsal-ventral (up/down) manner. In addition, for the purposes of neurovascular coupling, we did not see the need to isolate specific whisker barrels – we aimed to stimulate all the whiskers on one side of the mouse. A simple approach is to attach a stimulus bar onto a motor that is programmed to move in the up-down direction with a certain frequency, with stimuli starting at a specific time and ending at a specific time, as determined by a hardware trigger.

Three inexpensive motors include servo motors, DC motors and stepper motors. Servo motors are the easiest to use, and have internal circuitry that allows one to program a particular angle of rotation. However they are loud and slow. DC motors are the most common type of motor, with two wires that allow the motor to be run either forward or backward by reversing the polarity of the voltage across the two wires. These are not very accurate. Stepper motors are discretized versions of a normal motor, i.e. they have a number of coils oriented around a central axle, which rotates as it clicks from coil to coil as a series of "step" commands are given by the control circuitry. This design allows for precise, accurate control of the motor: with a proper signal, it can be turned in very accurate steps of set degree increments (e.g. one-degree increments, half-degree increments, etc.). Hence, stepper motors are extremely fast, precise and quiet – we chose to use a bipolar stepper motor to deliver whisker stimuli to the awake mouse. An open-source hardware system using an Arduino (a microcontroller) and an H-bridge (an electronic circuit that enables a voltage to be applied across a load in opposite direction) to run and program a stepper motor was developed by Clay Lacefield (www.openmaze.org) – we adopted this approach for our purposes. Our schematic for digitally controlling a bipolar stepper motor with two digital pins from an Arduino is shown in Fig 26 (directly replicated from OpenMaze).

Now, it is also important to ensure that the stimulus paradigm is delivered exactly at a certain time point during each experiment trial. The camera and LEDs are programmed to image a sequence of a certain number of trials (5, 10, 15 etc.) of a certain total duration (30 seconds) at a time (a "run"). We used 5 second (long) and 1 second (short) stimuli that are delivered at 10 seconds into the trial. It's important to ensure that the whisker stimulus is initiated at exactly 10 seconds – to accomplish this a NI-DAQ (National Instruments Data AcQuisition) board is used to synchronize the camera, and the stimulus signal.

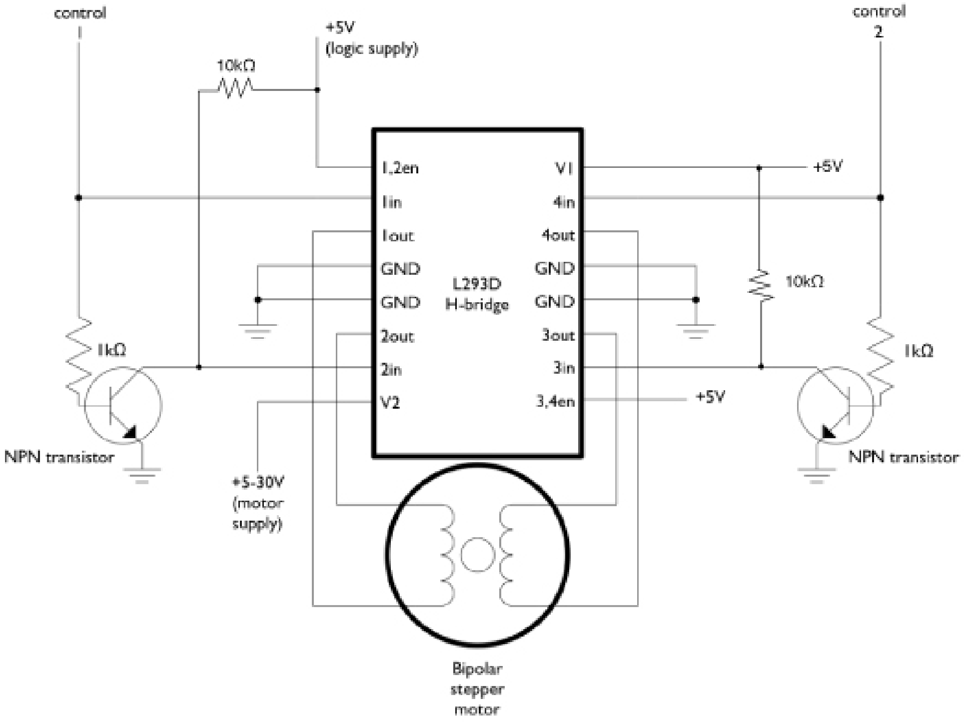

Fig 26. Bipolar stepper two-wire circuit. This circuit allows one to use just two Arduino control pins to drive the stepper motor. The step sequence is controlled by simultaneously sending combinations of "low" and "high" values to the two control pins.

The camera exposure signal is fed into the NI-DAQ board as a digital hardware trigger. The NI-DAQ board itself is programmed and controlled with MATLAB, and set up to deliver a "high" signal to the Arduino starting at 10 seconds, for the duration of the stimulus. A separate computer was traditionally used for this purpose (the "stimulus computer"), but is unnecessary with modern computing power. In any case, the stimulus computer is set up at the beginning of each trial to "listen" for the camera exposure hardware trigger signal – when it is received, it immediately initiates a counter for the stimulus paradigm. At 10 seconds into the trial, the DAQ board itself sends a "high" digital signal to the Arduino. The Arduino is also set up to listen to the DAQ signal as a hardware interrupt, which forces the microcontroller to initiate the stepper motor. The frequency and range of the motor is pre-programmed into the Arduino. These hardware triggers and interrupts are accurate and precise to the nanosecond scale – and ensure that changes in neuronal activity begin exactly at the specified time. Sometimes, however, hardware triggers are unavailable or unusable, requiring the use of software triggers, which are discussed below. As a final note, while the stimulus paradigm used for my experiments involves a 10 second pre-stim period, followed by a 5 second or 1 second stimulus, and a 15 second or 19 second post-stim period, these parameters can be easily changed in a simple custom-written MATLAB GUI that controls the DAQ board.

This whisker stimulus set up has worked extremely reliably for us over the past few years for our wide-field imaging set-up. However, it is not easily adapted for imaging with two-photon or our own light sheet (SCAPE) microscopy set-ups that require an imaging objective to be placed millimeters away from the imaging surface. Here, the stimulus bar is too physically constrained and can hit the imaging objective during stimulus delivery. In addition, the vibrations from the stepper motor introduce motion artifacts that are significant during microscopic imaging, while barely observed during wide-field imaging.

4.1.5. Cost-effective webcam imaging of various aspects of mouse behavior.

To complete our WFOM system, we wanted to capture the activity of the mouse during our imaging sessions. The OpenMaze website recommended using a PS3eye video camera – a USB webcam that was originally designed for use with the PlayStation gaming system. This $6 camera can capture up to 187 frames/second at 320x240 resolution, making it an extremely inexpensive solution for capturing mouse behavior. However, we could not use these cameras in the visible spectrum for recording behavior – the strobing of the blue, green and red LEDs make for a rather unusable behavior video. Instead, we decided to capture behavior with infrared illumination. An infrared LED is used to illuminate the mouse itself and an infrared light blocking filter is placed in the imaging camera. The PS3-eye webcam has an infrared blocking filter that is removed, and a second filter that blocks visible light but allows infrared light to pass is placed in front of the webcam. These modifications allow us to simultaneously capture mouse behavior with infrared illumination and neuronal activity and hemodynamics with strobed LEDs in the visible light spectrum.

However, it was also important to ensure that the webcam is synchronized with the main imaging camera. As mentioned previously, since we are using a USB webcam, without dissecting the actual circuitry of the camera, it's impossible to send a hardware trigger to the PS3-eye. Instead, we relied on software triggers. Software triggers are signals sent from a webcam recording program through the computer to the webcam to begin a recording sequence. Since there are delays with which this signal is processed and sent to the webcam, it takes a finite, variable amount of time before the webcam actually starts recording the data – this is referred to as "jitter". Since the average delay time was in the millisecond range, and our imaging camera itself is capturing data at ~10 Hz per channel, we decided that the webcam data delay and jitter were probably unobservable when comparing the behavioral data to the camera images. However, in an ideal situation, a hardware trigger should be used to properly synchronize all the imaging devices.

Finally, we wanted to record as many behavioral metrics as we could using our set-up. While initially we only used one webcam, this system is easily adaptable to simultaneously record for several webcams at once. In our final set up, three webcams (**Fig 27**) are used to image mouse behavior (synchronized to the imaging system) with infrared filters placed in front of them to prevent contamination from the imaging LEDs. A zoom lens placed on one webcam is used to image changes in pupil diameter. Another webcam is used to look at gross mouse behavior. Finally a third webcam is placed underneath the transparent disk the mouse is seated on and can be used to track the position of the paws and gait of the animal.

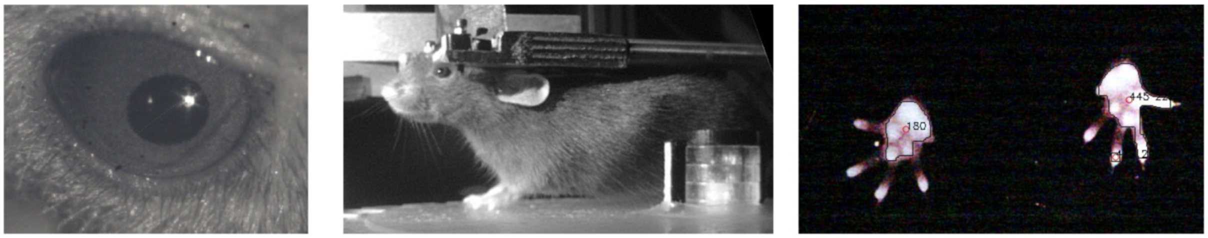

Fig 27. Behavioral measurements. Left: Pupillometry with zoomed in webcam. Middle: Imaging of gross mouse behavior. Right: Paw tracking of the animal with a webcam underneath the animal.

4.1.6. The complete WFOM system for imaging neuronal activity and hemodynamics in Thy1-GCaMP6f animals

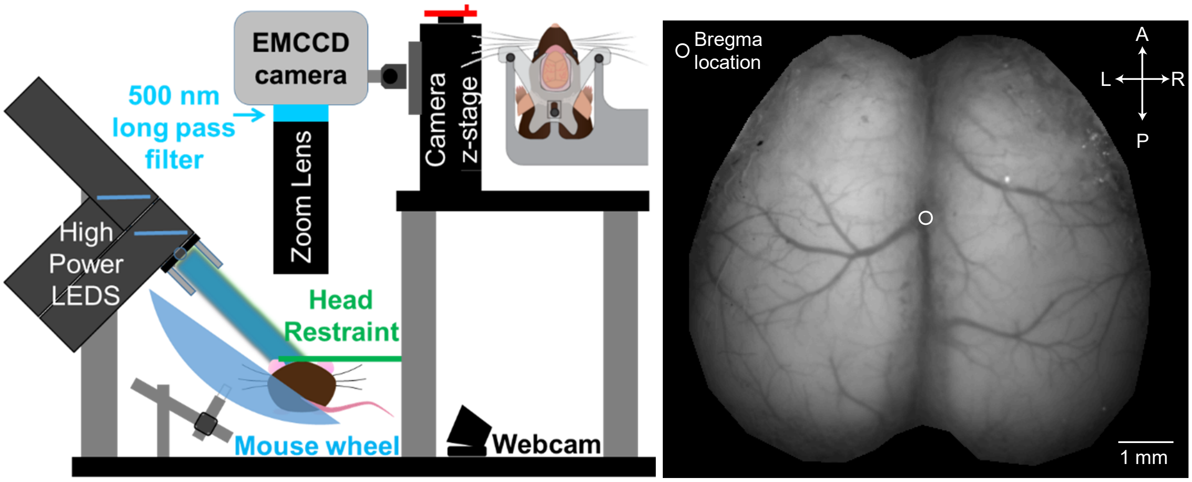

Fig 28. Left: High Power LEDs are strobed on the mouse window and are synchronized to the exposure signal of an EMCCD camera (Andor iXon 885) that acquires reflectance and fluorescence images of the pial surface. (1x1 binning, 35 fps / 3 channels). A top-down view of the head restrained animal is shown as a schematic on the top right. Right: Grayscale fluorescence image of a thinned-skull, awake and head-restrained Thy1-GCaMP6f mouse.

Shown in Fig 28 is the complete WFOM set-up and includes the imaging camera, the behavior webcam, the strobed LEDs and the mouse set up. Also shown is a schematic of the head restraint. A grayscale image of the fluorescence signal from a thinned-skull, awake, head-restrained animal is additionally shown. As seen, a large portion of the surface of the brain, including the arterial and venous surface vasculature can be adequately imaged using our technique.

4.2. Correction of the hemodynamic artifact in the fluorescence channel to obtain the pure neuronal signal.

For all our experiments, we used Thy1-GCaMP6f mice, (C57BL/6J-Tg(Thy1-GCaMP6f)GP5.17Dkim/J, strain purchased from Jackson Labs and bred in-house), where the GCaMP6f fluorophore is expressed in layer II/III and V excitatory neurons (Fig 29). The Thy1-GCaMP6f mouse line is readily available and allows us to image activity of neurons in the processing and output layers of the cortex, giving one a good overall gauge of activity in the brain. However, it is important to consider the effects of hemoglobin absorption on the fluorescence signal – this represents an important confound that changes the apparent nature of neuronal activity in the brain. However, we can actually estimate the contamination of hemodynamics in the fluorescence channel and remove it in order to obtain the pure neural signal – our Ex-Em approach (Ma, Shaik, Kim, et al., 2016) to this problem is described next.

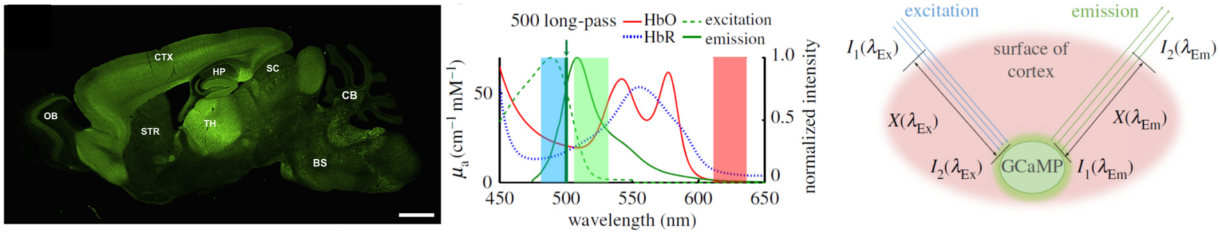

Fig 29. Left: Cross-section of a Thy1-GCaMP brain (www.jax.org). Middle: Excitation/Emission spectra of GCaMP alongside hemoglobin absorbance spectra. Right: Schematic of light paths in WFOM traveling to and from a GCaMP interaction.

Fig 29 (right) illustrates path taken by light to and from an interaction with a fluorophore. Excitation light must travel a path-length $X(\lambda_{ex})$ through the brain before reaching the fluorophore, and along this path will experience the absorption properties of the tissue it travels through. Light emitted from the tissue is similarly attenuated. As shown in Fig 29 (middle), the excitation and emission bands of GCaMP overlap with strong (and different) absorption bands of HbO and HbR. If background absorption properties remained constant, these effects would have minimal consequences; however, during neurovascular coupling, almost all neural activity is accompanied with functional hyperemia (Hillman, 2014). These changes in hemodynamics will thus modulate detected fluorescence, contaminating fluorescence recordings. We can write a simple model for this effect:

$$\frac{I_2(\lambda_{Ex})}{I_1(\lambda_{Ex})} = e^{-\mu_a(\lambda_{Ex})X(\lambda_{Ex})}$$

Equation 7

and

$$\frac{I_2(\lambda_{Em})}{I_1(\lambda_{Em})} = e^{-\mu_a(\lambda_{Em})X(\lambda_{Em})}$$

Equation 8

where $I_1(\lambda_{Ex})$ represents the initial intensity of excitation light entering the tissue, $I_2(\lambda_{Ex})$ represents the intensity of the excitation light reaching the fluorophore after travelling pathlength $X(\lambda_{Ex})$

through tissue with absorption coefficient $\mu_a(\lambda_{Ex})$. Similarly $I_1(\lambda_{Em})$ represents the initial intensity of fluorescent emission light and $I_2(\lambda_{Em})$ is the intensity of emission light exciting the tissue after travelling pathlength $X(\lambda_{Em})$ through tissue with absorption coefficient $\mu_a(\lambda_{Em})$. Conversion of excitation light to fluorescence by a fluorophore is a function of σ, the fluorophore's conversion efficiency and c_f, representing either the concentration of the fluorophore or the effect (e.g. concentration of calcium) that fluorescence is proportional to. Therefore,

$$I_1(\lambda_{Em}) = I_2(\lambda_{Ex}) \cdot \sigma \cdot c_f$$

Equation 9

By substituting Equation 7and Equation 8 into Equation 9, the intensity of fluorescence emission light emerging from the tissue is given by:

$$I_2(\lambda_{Em}) = I_1(\lambda_{Ex}) e^{-[\mu_a(\lambda_{Ex})X(\lambda_{Ex})+\mu_a(\lambda_{Em})X(\lambda_{Em})]} \cdot \sigma \cdot c_f$$

Equation 10

The measured fluorescence signal at time t, relative to a baseline state $F_{Meas}(t_0)$ gives us:

$$\frac{F_{Meas}(t)}{F_{Meas}(t_0)} = I_1(\lambda_{Ex}) e^{-[\Delta\mu_a(t,\lambda_{Ex})X(\lambda_{Ex})+\Delta\mu_a(t,\lambda_{Em})X(\lambda_{Em})]} \cdot \frac{c_f(t)}{c_f(t_0)}$$

Equation 11

The above equation demonstrates the multiplicative effects of absorption (hemodynamic) cross-talk with respect to the ratiometric change in intracellular calcium. This cross-talk is also dependent upon the traveled path-length. The spatial distribution of fluorophores can affect the magnitude of hemodynamic cross-talk affecting data. Thy1-GCaMP mice have a dense concentration of fluorophores in layers II/III, followed by layer V. In a uniformly fluorescence sample, most fluorescent light will be detected from superficial layers, photons that will have travelled a shorter path-length and will, therefore, carry exponentially less hemodynamic contamination than in measurements of fluorophores situated in deeper layers. Hence, most of the signal collected from the Thy1-GCaMP mice is from layers II and III.

There are several different approaches to removing the hemodynamic cross-talk from the fluorescence signal, as described previously (Ma, Shaik, Kim, et al., 2016). The technique that worked best for us is the Ex-Em method which corrects for attenuation changes at both the excitation and emission bands of the fluorophore. In practice, acquiring reflectance images at the fluorophore's excitation band is difficult to achieve for high frame-rate imaging using a single camera, since a long-pass filter would need to be modulated in front of the camera, or a second camera would be needed. Instead, we show here that an improved correction can be achieved via dual-wavelength reflectance measurements that do not necessarily include the fluorophore's excitation band.

GCaMP is excited at 488 nm and diffuse reflectance is measured at 530 and 630 nm. Based on the theoretical framework presented above, our analysis should be able to infer the corresponding time-varying changes in [HbO] and [HbR] for each pixel using these 530 and 630 nm reflectance measurements. Equation 3 can then be used to calculate the effective cortical $\Delta\mu_a$ at the 488 nm excitation wavelength at the same point in time. We can, therefore, formulate an absorption part of the correction factor as:

$$\begin{aligned}
&\Delta\mu_a(t,\lambda_{Ex})X(\lambda_{Ex}) + \Delta\mu_a(t,\lambda_{Em})X(\lambda_{Em}) \\
&\qquad\qquad \approx \big(\varepsilon_{HbO}(\lambda_{Ex})\Delta[HbO](t) + \varepsilon_{HbR}(\lambda_{Ex})\Delta[HbR](t)\big)X_{est}(\lambda_{Ex}) \\
&\qquad\qquad + \big(\varepsilon_{HbO}(\lambda_{Em})\Delta[HbO](t) + \varepsilon_{HbR}(\lambda_{Em})\Delta[HbR](t)\big)X_{est}(\lambda_{Em})
\end{aligned}$$

Path-length values X_{Est} need to be estimated, and in practice, values of $X_{est}(\lambda_{Ex}) = 0.3\text{-}0.56\ \mathrm{mm}^{-1}$ and $X_{est}(\lambda_{Ex}) = 0.3\text{-}0.57\ \mathrm{mm}^{-1}$ in Thy1-GCaMP mice have been found to yield corrected GCaMP images with minimal vessel artifacts and low-frequency trends resembling hemodynamic cross-talk.

Fig 30 demonstrates the effects of hemodynamic correction during functional activation of the whisker barrel during stimulus-evoked neurovascular coupling. The GCaMP image before correction shows strong vessel artifacts corresponding to absorption by hemoglobin, which are removed after correction. The time course of the uncorrected GCaMP trace for a 5 s tactile whisker stimulation, peaks at first and then dips below baseline as the hemodynamic response reaches its peak. After correction, the GCaMP signal stays positive for the duration of the stimulus, which is physiologically appropriate.

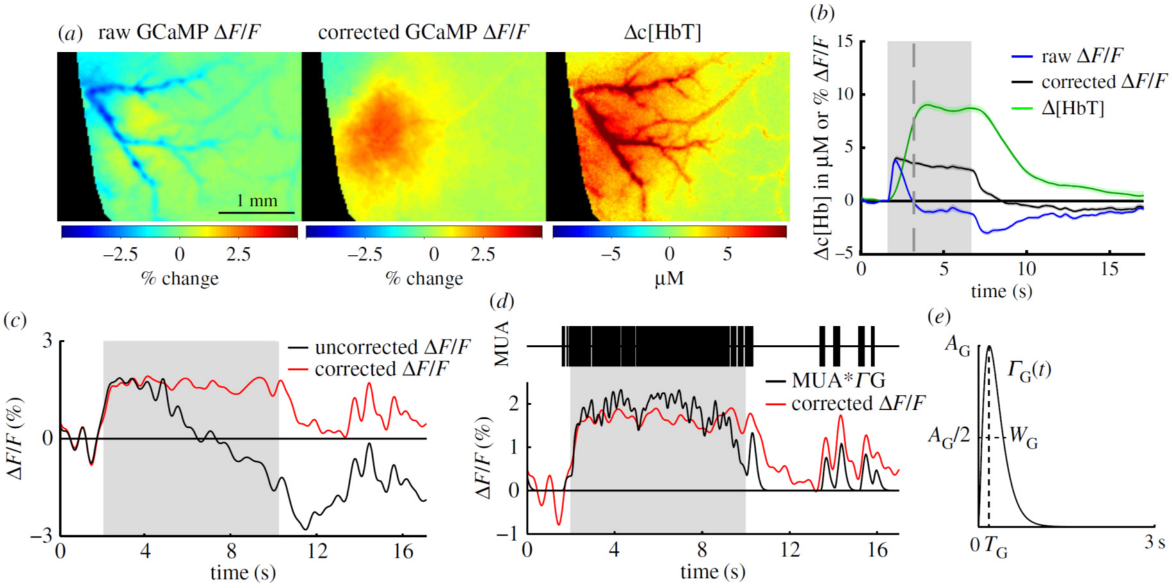

Fig 30. Hemodynamic correction of WFOM GCaMP data. (a) GCaMP data before and after hemodynamic correction. Maps are for 1.7 s after onset of a 5 s tactile whisker stimulus in an awake mouse. Corrected image shows vessel artifacts, whereas original response is dominated by the hemodynamic confound. (b) Time courses show the GCaMP signal before and after correction, in comparison with the [HbT] hemodynamic response. (c) Raw uncorrected and single-wavelength ratiometrically corrected and GCaMP signals acquired in a urethane-anaesthetized Thy1-GCaMP3 mouse undergoing an 8 s electrical hindpaw stimulation. (d) An electrode inserted into the responding region recorded multi-unit activity (MUA). The GCaMP fluorescence signal after hemodynamic correction can be closely replicated by convolving MUA with a gamma function (e) to model the combined dynamics of intracellular calcium and GCaMP fluorescence changes.

To verify whether hemodynamics-corrected GCaMP fluorescence signals reflect underlying neural activity (Fig 30), GCaMP fluorescence measurements were compared to simultaneously recorded multi-unit activity (MUA) in anesthetized animals (n=9 mice) at the same cortical locations. A gamma-variate function was chosen to mimic the fast onset and gradual decay kinetics of neural calcium and the kinetics of GCaMP fluorescence in response to calcium changes. As expected from the overlap of hemoglobin and GCaMP excitation and emission bands a correction for the contaminating effects of hemodynamics was applied to the raw GCaMP data. Spontaneous MUA recordings, along with the time-course of hemoglobin-corrected GCaMP fluorescence from the same region, and a prediction of GCaMP fluorescence based on the convolution of MUA with a best-fit gamma function (correlation coefficient = 0.86) are shown.

The quality of the fit between predicted GCaMP and measured data, before and after correction, shows an average correlation coefficient of 0.72 ± 0.01 for spontaneous activity and 0.70 ± 0.01 for stimulus-evoked activity after correction. The gamma function parameters describing the best-fit GCaMP fluorescence kernel also agree well with GCaMP characterization results using two-photon and cell-attached recordings (time to peak = 0.18 ± 0.01s and width = 0.35 ± 0.02s for spontaneous activity). This strong agreement between recorded GCaMP fluorescence and MUA-predicted fluorescence demonstrates that (hemodynamics-corrected) wide-field GCaMP signals in Thy1-GCaMP mice provides an accurate representation of the piking activity of excitatory neurons.

4.3. Resting-state neuronal activity and hemodynamics in the awake mouse.

Once we were confident in the hemodynamic and corrected GCaMP we were obtaining from the WFOM system in awake, behaving mice, we began to use our system to study normal and altered physiology in the mice. While my own studies focused on stimulus-evoked neurovascular coupling, my colleagues (Ying Ma, Sharon Kim) and I often collected resting state data from these animals. These were 1 minute – 3 minute trials where the animal was under not stimulus or task paradigms, and chose to stay stationary on the provided running wheel. The observations from this data, as well as the deconvolution analysis technique used to fully explore it became quite useful for studying stimulus-evoked neurovascular coupling in the brain. The results from our observations of resting state activity in the awake mouse are described below.

4.3.1. Spontaneous (and bilaterally synchronous) patterns of neuronal activity and linearly coupled hemodynamic activity is observed in the awake mouse.

A short sequence of neuronal activity and hemodynamic recordings in Fig 31E shows that GCaMP activity patterns are generally bilaterally synchronized. GCaMP patterns that occur at a certain time point (t=16.1 seconds), are mirrored in the hemodynamics 1.6 seconds later. This suggests that neuronal activity is coupled to hemodynamics in the resting state in awake mice. However, we needed to quantify the nature of neurovascular coupling further.

A commonly approach is to assume a linear model of neurovascular coupling, such that hemodynamics correspond to the convolution of neural activity and a gamma-shaped hemodynamic response function (HRF) (G. M. Boynton, S. A. Engel, G. H. Glover, & D. J. Heeger, 1996; Cardoso, Sirotin, Lima, Glushenkova, & Das, 2012). Two of the three strategies we developed for measuring the HRFs (Ma, Shaik, Kozberg, et al., 2016) are described: gamma-variate fitting and deconvolution.

Gamma-variate fitting analysis has been performed previously to analyze stimulus-evoked neurovascular coupling data (Cardoso et al., 2012; C. Martin, J. Martindale, J. Berwick, & J. Mayhew, 2006). Here, a three-parameter gamma-variate function was used to approximate an HRF. Parameters were optimized to yield the best-fit (minimized least-squares error) between measured Δ[HbT] and the HRF convolved with corrected GCaMP-based recordings of neural activity. The resulting best-fit HRF at each pixel was then convolved with the GCaMP time course of that pixel and compared with measured Δ[HbT] at the same position using Pearson's correlation coefficient to quantify the goodness of fit. This method assumes a clear linear model of neurovascular coupling where excitatory activity is expected to generate a proportional, localized increase in [HbT].

Deconvolution is an alternative approach that similarly assumes a linear convolved model of neurovascular coupling but does not impose constraints on the temporal shape of the convolved HRF. A diagonal loading method was used to de-convolve each pixel of Δ[HbT] data from corrected GCaMP data, yielding a similar spatially resolved HRF for each dataset. The resulting HRF at each pixel was the re-convolved with the pixel's GCaMP time course, and compared with the pixel's measured Δ[HbT] using Pearson's correlation.

Fig 31 shows fitting results for awake, resting-state mice. For two cortical locations within the same trial, traces of corrected GCaMP6f are plotted along with measured Δ[HbT], gamma-variate fit Δ[HbT], and deconvolution-predicted Δ[HbT]. Before fitting, both GCaMP6f and Δ[HbT] data were filtered using a 0.02-Hz high-pass filter (HPF) to remove slow drifts, as well as a 2-Hz low-pass filter (LPF) to reduce physiological noise. Both fits show good agreement with measured

Δ[HbT] and resemble the fluctuations of resting-state hemodynamics. HRFs derived using both methods exhibit similar temporal shapes and correlation coefficients (Fig 31C).

Performing fitting analysis for each pixel individually permits HRFs to vary spatially over the field of view. Fig 31D shows a map of the Pearson correlation coefficient between measured and gamma-variate modeled Δ[HbT], and maps of optimized fit parameters (gamma function amplitude A_H, peak time T_H, and width W_H) from the same trial shown in Fig 31B. Fit parameters vary somewhat across the cortex, with A tracing the arterial trees on the surface of the brain reflects the higher amplitude contribution of surface vessels to WFOM hemodynamics. Fig 31E shows a sequence of images from the same trial including corrected GCaMP6f, measured Δ[HbT], the best-fit (gamma-variate) prediction of Δ[HbT], and fit residuals over the full field of view.

Even though the spatial patterns of neural activity have a much faster pace compared with the observed hemodynamics, convolution of the GCaMP signal with fitted HRFs yields a predicted Δ[HbT] that is a close match to the measured Δ[HbT] dynamics. Both increases and decreases in Δ[HbT] are accurately modeled from the observed increases and decreases in excitatory neural activity. To summarize fit quality across all trials and all mice, a region over the somatosensory cortex was binned to 16 × 16 pixels (equivalent to a 1-mm^2 region) and analyzed using both deconvolution and gamma-variate fitting. Fig 31F shows average Pearson's correlation coefficients and their standard deviations over these regions for individual trials in chronological order for the deconvolution model. The overall distribution of averaged correlation coefficients across trials, days, and animals is also shown. Correlation coefficients ranged from 0.3 to 0.9, with an average across all animals and trials of 0.63 ± 0.02 over six animals (0.53 ± 0.03 for gamma-variate fitting, where the temporal shape of the HRF is more constrained).

These results strongly suggested the hemodynamic activity in the awake mouse is generally linearly coupled to excitatory neuronal activity in the awake mouse brain.

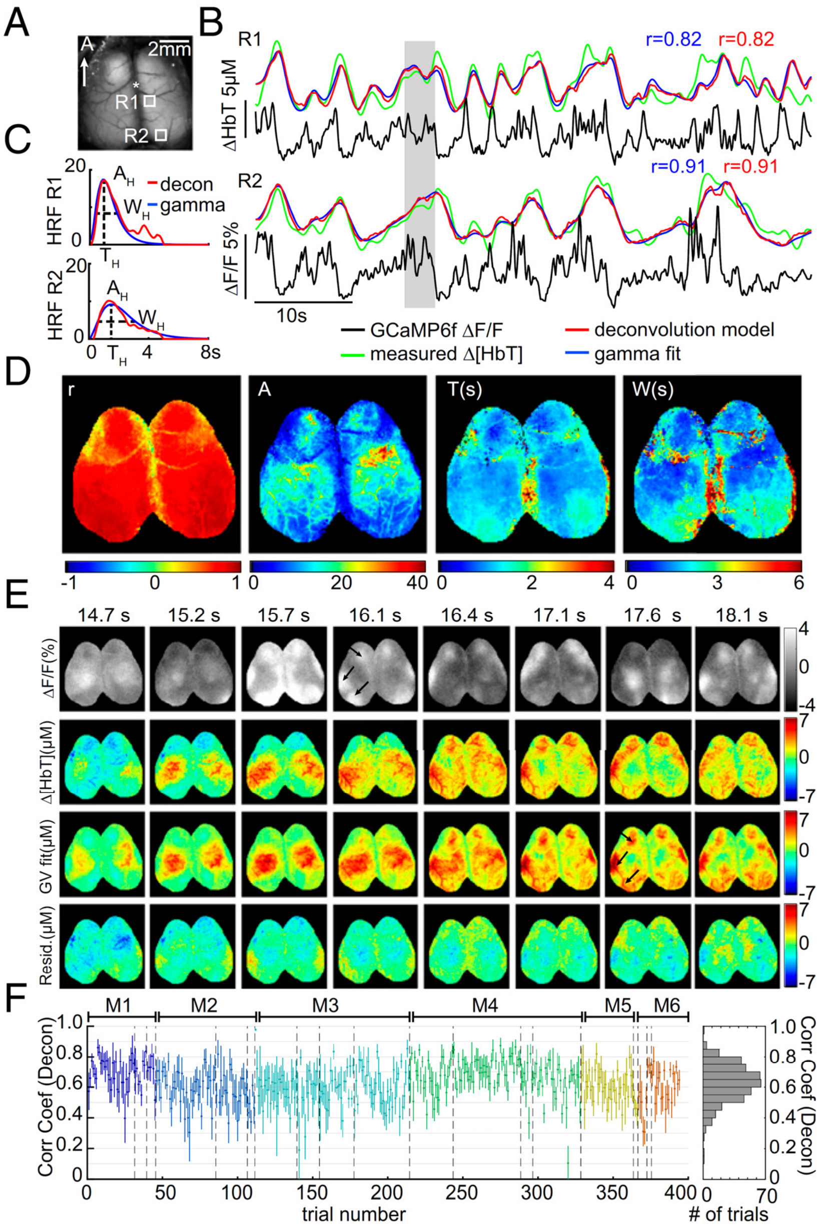

Fig 31. Adapted from (Ma, Shaik, Kozberg, et al., 2016) Spatiotemporal modeling of hemodynamics from wide-field Thy1- GCaMP6f recordings in the awake, resting brain. (A) Grayscale blue image of the cortex. (B) 60 second examples of awake, resting-state GCaMP6f and Δ[HbT] from the two regions indicated in A. Red and blue traces show the results of convolving corrected GCaMP fluorescence with hemodynamic response functions (HRFs) derived via deconvolution or gamma-variate fitting, respectively. (C) Deconvolved HRF and best-fit gamma-variate HRF for the time series shown in B illustrating the amplitude A_H, time of peak as T_H and width at half-maximum as W_H gamma-fit parameters. (D, Left) Map of gamma-variate fit Pearson's correlation coefficients. (Right) Gamma-variate HRF best-fit parameters (A_H, T_H, and W_H) for the trial shown in B. (E) Example epoch, top row: corrected Thy1-GCaMP6f ΔF/F; second row: Δ[HbT]; third row: gamma-variate model fit to Δ[HbT] based on the GCaMP signal; bottom row: fit residuals. Arrows highlight specific neural events that are mirrored in later hemodynamics. (F) Plot of mean average and SD [over 16 × 16 regions (1 mm^2) over S1] Pearson's correlation coefficients for the deconvolution model for all resting state epochs in all six mice (histogram at Right shows overall distribution for all trials). Values are chronological with dotted lines indicating different days and colors indicating different mice, M1–M6.

4.3.2. Effect of anesthesia and slow (<0.04 Hz) hemodynamic trends on neurovascular coupling.

We had conducted a similar set of resting-state imaging experiments as described above in urethane-anesthetized Thy1-GCaMP3 mice. We used the same analysis methods as described above and found our fits to be much more variable on the raw data, yielding correlation coefficients ranging from 0.19-0.87 (Ma, Shaik, Kozberg, et al., 2016). A trial with a correlation coefficient of 0.19 is shown in Fig 32B. The measured Δ[HbT] time course in this case exhibits a large decrease in [HbT] in the middle of the trial that is not accounted for in either deconvolution or gamma-variate–based model fitting. High-pass filtering of hemodynamic time courses at 0.04 Hz was found to remove these slow trends, yielding resting-state hemodynamics that more closely resemble those seen in awake data. Performing deconvolution and gamma-variate fitting after 0.04-Hz high-pass filtering of both GCaMP and Δ[HbT] data dramatically improved fit correlation coefficients as shown in Fig 32C. Repeated across all anesthetized animals, fitting before and after <0.04-Hz slow-trend removal, the average correlation coefficients across all anesthetized animals and trials improved from 0.44 ± 0.05 to 0.68 ± 0.04 for gamma variate fitting and 0.41 ± 0.06 to 0.70 ± 0.03 for deconvolution ($P = 0.005$ and $P = 0.006$, respectively; $n = 6$; paired t test) (Fig 32F and G).

We can visualize the spatiotemporal properties of <0.04-Hz slow hemodynamic trends. Fig 32D maps 0.04-Hz low-pass–filtered frames across the duration of the large decrease in [HbT] seen in Fig 32B, showing a large trend across the field of view with a clear structure of pial arterioles. Fig 32E shows a shorter epoch, separating frequency components of Δ[HbT] below and above 0.04 Hz, and demonstrates that faster [HbT] components >0.04 Hz are still modeled by gamma-variate fitting to Thy1-GCaMP3 data during slow hemodynamic trends. In all cases, slow trends in Δ[HbT] are not well predicted by Thy1- GCaMP data and have vascular structure. In animals with bilateral cortical exposures, slow trends exhibit bilateral symmetry.

To determine whether slow hemodynamic trends are unique to urethane anesthesia, <0.04-Hz slow-trend removal analysis was repeated on all awake data. High-pass filtering awake data at 0.04 Hz before fitting had a much smaller effect on fit correlation coefficients than for anesthetized data (Fig 32G) (average correlations changed from 0.51 ± 0.02 to 0.58 ± 0.02 for gamma-variate fitting and 0.64 ± 0.01 to 0.63 ± 0.01, n.s. $P = 0.63$, for deconvolution, all for $n = 6$, paired t test. Fig 32H shows that high-pass filtering at 0.04 Hz removes significantly more variance from anesthetized data than data acquired in the awake brain ($P = 0.015$; $n = 6$; paired t test).

In summary, some anesthetized animals were found to exhibit large, slow (<0.04-Hz) hemodynamic trends that were not well predicted by simultaneous GCaMP recordings. However, these periods did not represent complete "uncoupling," because removal of the slow hemodynamic component using a 0.04-Hz HPF left residual hemodynamics that could be well predicted by local GCaMP fluctuations. Also, Thy1-GCaMP fluorescence selectively reports spiking activity in excitatory neurons in layers 2/3 and 5. Slower hemodynamic trends could be driven by different types of neurons in the cortex, or by deep brain regions like the basal forebrain and locus coeruleus. Deep brain regions often use neurotransmitters that are potently vasoactive (acetylcholine, norepinephrine), which could be significantly altering blood flow in the brain.

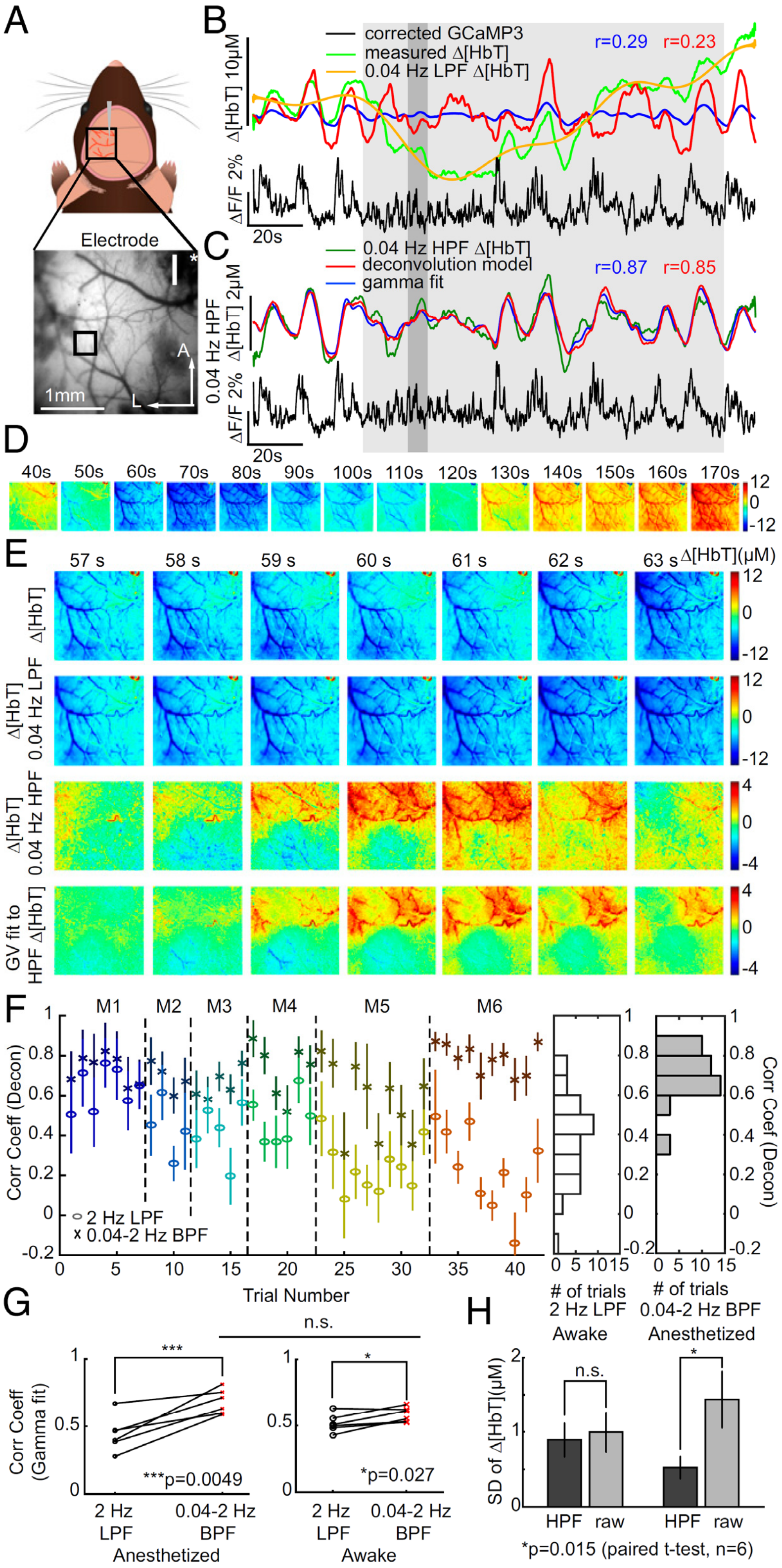

Fig 32. Analysis of urethane-anesthetized animals and the presence of slow hemodynamic trends. (A) A smaller, unilateral window over S1. (B) Time courses of original Δ[HbT] and Thy1-GCaMP3 fluorescence (2-Hz LPF only) with "best-fit" deconvolution and gamma-variate fits. Yellow shows <0.04-Hz slow trend in [HbT]. (C) Plots as in B after 0.04- to 2-Hz bandpass filtering (BPF) of both [HbT] and GcaMP3 fluorescence to remove slow trends yielding improved fits. (D) Image sequence showing <0.04-Hz component of Δ[HbT] from 40 to 170 s for the same trial. (E) Image sequence from 57 to 63 s showing from Top to Bottom: original [HbT] (<2-Hz LPF), slow trend [HbT] (<0.04-Hz LPF), [HbT] >0.04- to 2-Hz BPF, gamma-variate fit to 0.04- to 2-Hz BPF Δ[HbT] from 0.04 to 2-Hz BPF-corrected GCaMP3. (F) Mean average Pearson's correlation coefficients and SD over S1 for deconvolution model for all anesthetized animals (M1–M6) before (circles) and after (crosses) >0.04-Hz HPF of [HbT] and GCaMP3 fluorescence. Histogram to Right shows summary distributions for before (white) and after (gray) >0.04-Hz HPF. (G) Pearson's correlation coefficients for gamma-variate fitting with only a 2-Hz LPF and after 0.04- to 2-Hz BPF of Δ[HbT] for both anesthetized and awake data for each mouse. n.s., P = 0.05. (H) SD of Δ[HbT] (2-Hz LPF) over time before and after >0.04-Hz HPF for awake and anesthetized data.

4.3.3. Comparison of resting state neurovascular coupling in awake vs. anesthetized animals.

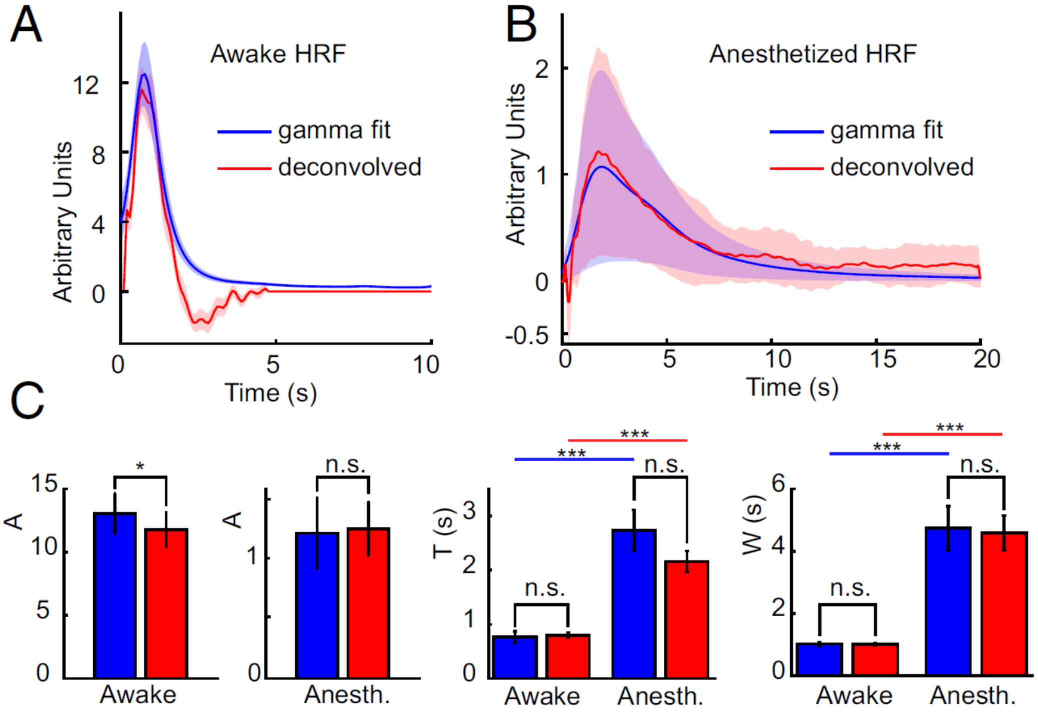

*Fig 33. Summary of HRFs derived from multiple analysis methods. (A and B) Comparisons of HRFs derived from gamma-variate fitting (blue) and deconvolution (red) in awake (A) and anesthetized (B) animals within the somatosensory cortex. Shaded regions show SEM across n = 6 mice in each group. (C) Parametric comparison of values from gamma-variate fits (averaged over S1), A (*P = 0.024, n.s. P = 0.66), T (n.s. awake P = 0.76, anesth P = 0.094, ***P < 0.005), W (n.s. awake P = 0.88, n.s. anesth P = 0.76, ***P < 0.005) (all paired-wise t test, n = 6) group.*

After accounting for the slow hemodynamic drifts seen in the anesthetized animal, it was also important to compare the nature of neurovascular coupling between anesthetized and awake animals. HRFs generated in awake and anesthetized conditions across all trials and mice, calculated using both gamma-variate fitting and deconvolution are compared in Fig 33. The HRF in awake Thy1-GCaMP6f animals (using 0.02- to 2-Hz BPF) was consistently found to have a shorter time to peak ($P < 0.005$ for both models) and a narrower peak than anesthetized Thy1-GCaMP3 mice (0.04- to 2-Hz BPF) (Fig 33C) ($P < 0.005$ for both models, double-sided Student's t test; n = 6). This is consistent with previous observations of fast, robust hemodynamics in awake animals versus slower, lower amplitude hemodynamics in urethane-anesthetized animals (Pisauro et al., 2013).

4.3.4. Spontaneous vs. wave-like neuronal activity in the resting animal.

Previous reports using both wide-field GCaMP and voltage sensitive dye imaging have demonstrated cortical propagating waves (Vanni & Murphy, 2014) even demonstrating similar patterns of bilateral symmetry as described above (Mohajerani, McVea, Fingas, & Murphy, 2010). The symmetry of spontaneous neural activity has also been demonstrated in both animals (Liu, Zhu, Zhang, & Chen, 2013; Lu et al., 2007) and awake human subjects (Nir et al., 2008) via electrophysiological recordings from bilaterally symmetric regions. Widespread correlations and apparent waves of activity given by correlations between fMRI and discrete LFP recordings have also been noted in the awake primate brain (Shmuel & Leopold, 2008).

However, the presence of these waves of neural activity in the awake brain remains controversial (Logothetis et al., 2009). Waves and bursts of neural activity in the cortex are more usually reported under conditions of non-rapid eye movement (REM) sleep (Destexhe, Contreras, & Steriade, 1999), anesthesia (urethane, ketamine), and quiet wakefulness (Gentet, Avermann, Matyas, Staiger, & Petersen, 2010; Mohajerani et al., 2010). Such events are often characterized by alternating subthreshold cortical membrane depolarization and hyperpolarization (UP/DOWN states), where UP states envelop faster brain activity (e.g. gamma oscillations), while DOWN states are accompanied by cortical silence. This slow wave activity has been associated with memory consolidation (Destexhe & Contreras, 2006), and shaping responses to incoming stimulation (Petersen, Hahn, Mehta, Grinvald, & Sakmann, 2003). Although the role of thalamic inputs is not well understood, several studies suggest that UP states are generated in layer 5 neurons (Chauvette, Volgushev, & Timofeev, 2010; Lorincz et al., 2015) and propagate through local neural circuitry (Mohajerani et al., 2010; Stroh et al., 2013; Townsend et al., 2015). Although rhythmic UP and DOWN states are best described in anesthetized states, slow-wave activity has been reported in the awake mouse brain (Mohajerani et al., 2010). In humans, slow-wave activity has also been recorded in the awake brain (Nir et al., 2008), although was enhanced and most synchronized bilaterally during REM and stage 2 sleep.

To better understand wave-like activity in the cortex in our own WFOM system, we decided to conduct an experiment with anesthetic depth levels of ketamine/xylazine in a Thy1-GCaMP6f mouse. On initial observation, we found repeated rostro-caudal waves of high amplitude traveling across the cortex at ~1 Hz. This neuronal activity was significantly distinct from the activity we observed in the awake mouse. However, while the rostro-caudal waves were relatively consistent from one wave to the next, there were small differences in the origin and localization of these waves, suggesting a more complicated underlying process. Using phase-aligned spectral filtering (PASF), a technique developed by one of our collaborators for extracting wave-like behavior from three-dimensional data (Meng & Zheng, 2016), we were able to extract a more stereotyped rostro-caudal wave. After subtracting this wave from the raw data, the residual signal begins to appear more like neuronal activity that occurs in the awake mouse.

To further confirm that the residual activity superimposed with the PASF derived ketaminergic wave is similar to our previously observed patterns of spontaneous, bilaterally synchronous activity, we used non-negative matrix factorization (NNMF) to decompose the three dimensional data into different spatial and temporal components. The spatial components were found to be bilaterally synchronous, and demarcated functionally distinct regions of the cortex, hence consistent with our previous finding in awake animals. The NNMF derived spatial and temporal components were re-constructed and color-coded to better visualize the underlying neuronal activity in the ketamine-anesthetized mouse.

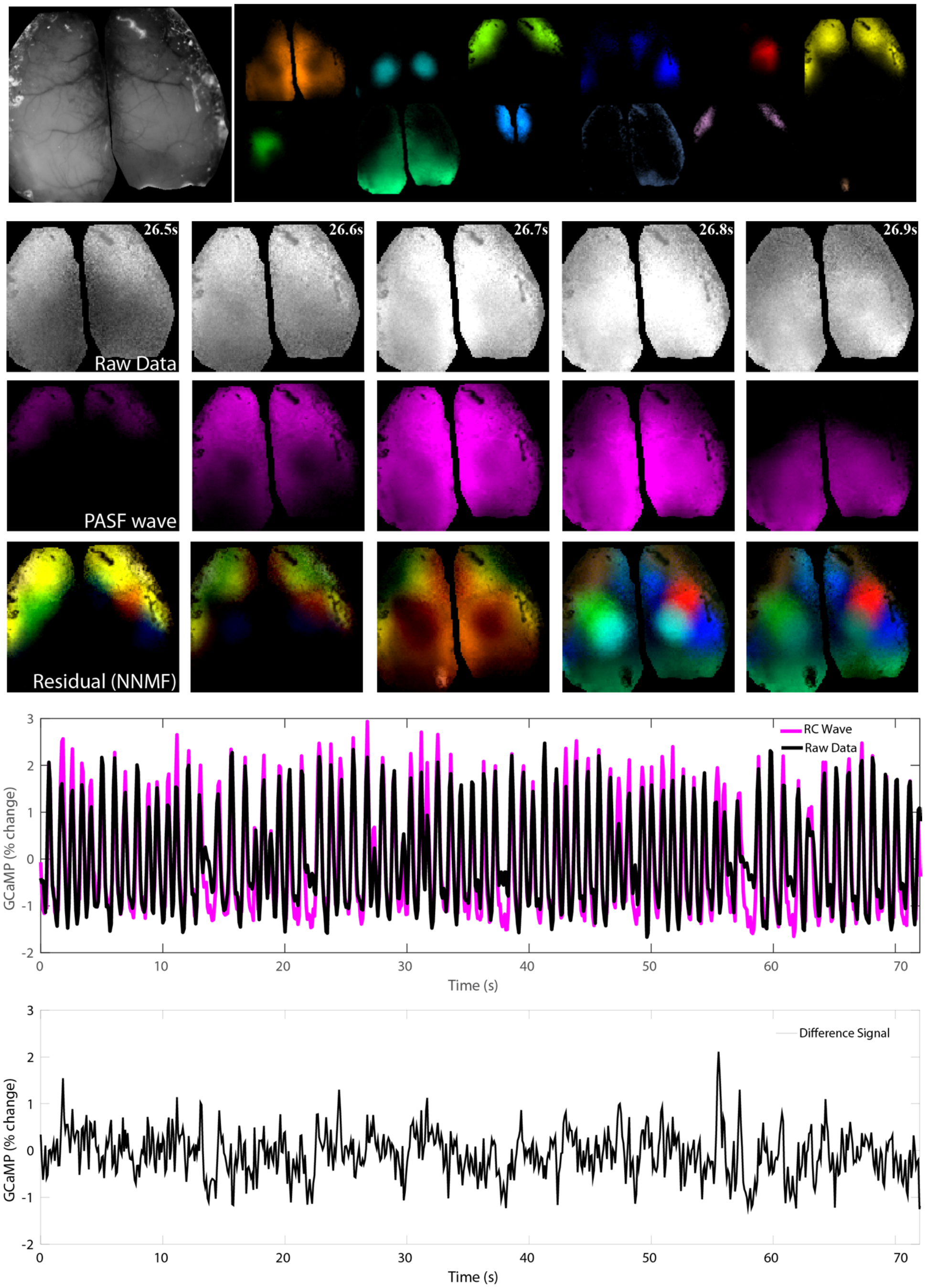

Fig 34. Top left: Grayscale fluorescence image. Top right: Decomposed spatial components after NNMF was applied to the residual GCaMP signal after subtracting the PASF-derived wave. Middle: A short temporal sequence demonstrating the rostro-caudal wave in the raw data and the PASF-derived wave, as well as the bilateral synchronicity of the underlying GCaMP signal (as shown after decomposing and reconstructing the residual data with NNMF). Bottom: Time course of the raw GCaMP data superimposed with the time course of the PASF-derived wave in the hindpaw region. Also shown is the difference between these signals, i.e. the residual GCaMP activity, which appears similar in nature to the GCaMP activity that occurs in normal, awake animals at rest.

These preliminary results strongly suggest that wave-like and spontaneous behavior are distinct "modes" of brain-wide activity that that could occur simultaneously in the rodent cortex. Further experiments using our WFOF imaging system, combined with techniques for analyzing resting state neuronal data (including PASF, NNMF and other dimensionality reduction techniques), can help us further elucidate the nature of brain-wide neuronal activity patterns in rodent mice under different behavioral conditions.

4.3.5. Effects of cholinergic modulation on resting state and stimulus-evoked neuronal activity and hemodynamics in the awake mouse.

While most of my studies involved attempting to perturb endothelial activity without affecting neuronal function, a few experiments revealed that some pharmacological manipulations can have dramatic effects on neuronal activity in the brain. One such experiment involved observing the effects of scopolamine, a nonselective, blood-brain barrier permeable anti-muscarinic agent. Acetylcholine is a potent vasodilator, and is the neurotransmitter used in the basal forebrain, which is an essential brain region involved in the etiology of Alzheimer's disease. Previous studies have found that direct stimulation of the basal forebrain increases cerebral blood flow (Lecrux, Kocharyan, Sandoe, Tong, & Hamel, 2012), whereas subthreshold stimulation of the basal forebrain augments whisker-stimulus evoked increases in cerebral blood flow (Lecrux et al., 2017). Acetylcholine also is a potent initiator of endothelium-derived hyperpolarization (EDH) and vasodilation (Tallini et al., 2007) – and we were curious what the effects of cholinergic inhibition would do the hemodynamic response. In anesthetized animals, previous studies found that scopolamine had no effect on hemodynamic responses, however, the anesthetic state of the animal is a significant confound with baseline cholinergic tone in the cortex (Constantinople & Bruno, 2011). Hence, we decided to intraperitoneally administer scopolamine at a 3 mg/kg concentration to observe its effects on stimulus-evoked and resting state activity in the mouse brain. Surprisingly, the drug had a rather profound effect on resting state neuronal activity, where it dramatically increased the amplitude of neuronal activity in the cortex across the frequency spectrum. Perhaps this was not so surprising, given that at the administered dosage, scopolamine is a potent amnestic (Rush, 1986). Interestingly, the drug had little effect on the frequency spectrum of the resting state hemodynamic fluctuations in the brain (Fig 35).

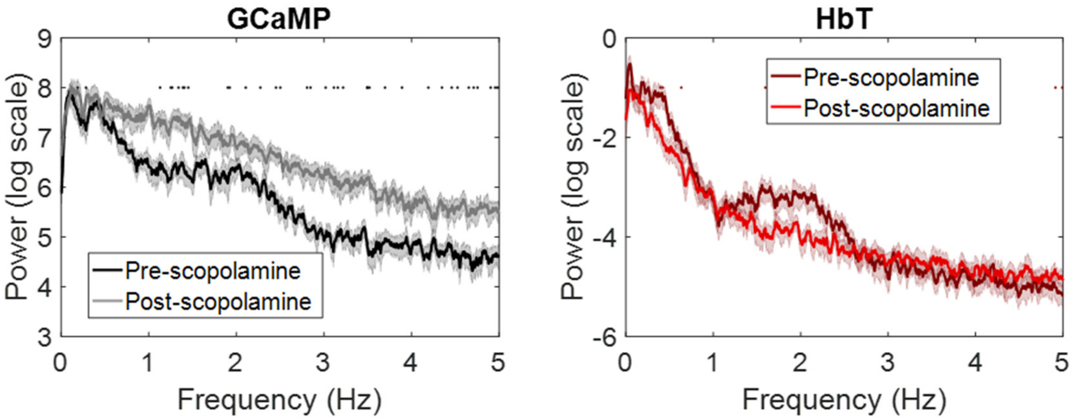

Fig 35. Effect of scopolamine on resting state neuronal activity in the brain. Left: Frequency spectrum of resting state neuronal activity before and after scopolamine administration (5 trials from 1 animal). Right: Frequency spectrum of resting hemodynamic activity from the same trials pre- and post- scopolamine.

During whisker stimulus neuronal activity, under normal conditions, there is widespread recruitment of the cortex (including the motor, visual and somatosensory cortices) that then localizes to the whisker barrel. After scopolamine administration, however, the GCaMP activity immediately localizes to the whisker barrel at a significantly reduced amplitude. Brain hemodynamics reflect these changes – the overall hemodynamic response localizes to the whisker barrel and is significantly lower in amplitude. The hemodynamic response in the whisker ("central") region is significantly lower in amplitude, whereas in regions surrounding the whisker barrel ("periphery"), the average stimulus-evoked neuronal and hemodynamic responses are virtually non-existent (Fig 36).

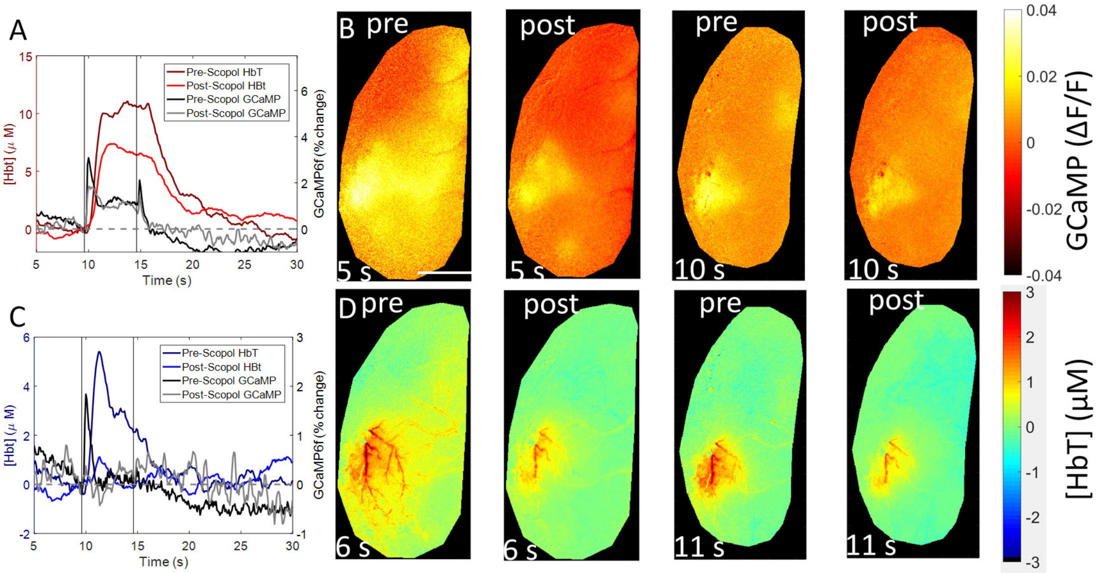

Fig 36. Effect of scopolamine on stimulus-evoked neuronal activity and hemodynamics in the awake mouse (n=1).

We hypothesize that the dramatic increase in baseline neuronal activity prevents the evolution of the normal stimulus-evoked neuronal response in the brain – which is then reflected in the hemodynamic response. In this situation, we have changes in both neuronal activity and hemodynamics during stimulus-evoked vasodilation, as a consequence of changes in resting neuronal activity. We additionally hypothesize that the nature of neurovascular coupling itself is probably unaltered. More experiments need to be conducted to further validate and explore this finding. Nonetheless, this preliminary result represents an exciting way to explore the relationship between cholinergic activity in the brain and neurovascular coupling in ways that were not possible in previous experiments.

5. Endothelial mechanism dissection in awake, behaving mice

Over the course of the previous few chapters, we explored the development of our toolset for studying the endothelial mechanisms of neurovascular coupling, from analysis techniques (deconvolution) to optical tools and the development of the WFOM system. Our primary goal, however, was to explore the spatiotemporal properties of hemodynamics in stimulus-evoked neurovascular coupling. Our experiments in the rat model provided us with several insights into the possible contribution of endothelial cells to neurovascular coupling. In this chapter, we focus exclusively on stimulus-evoked neurovascular coupling. We describe the spatiotemporal properties of the whisker stimulus-evoked neuronal and hemodynamic response before and after the administration of pharmacological agents meant to perturb endothelial function.

5.1 Detailed methods for pharmacological experiments

Experimental paradigm: For each pharmacological experiment, each animal was imaged for ~2 hours consisting of intermixed trials of 5s and 1s stimuli of 30 seconds total duration for each trial along with a few resting state trials that were 180 seconds in duration. The animal was allowed to rest for at least 15-20 minutes before intraperitoneal injection of the drug, followed by another imaging session of ~2 hours with trials consisting of resting state data, 5s stimuli and 1s stimuli as in the first imaging session. For animals where drug experiments were repeated, at least 1 week was allowed to pass before a new experiment (either with the same or different drug) was conducted.

Drug Concentrations: Drug concentrations were chosen to have the maximal effect on hemodynamic activity (based on concentrations used in other studies), while staying below the LD50 as well as concentrations that have previously been shown to have effects on systemic vascular resistance and blood pressure. All drugs were delivered via an intraperitoneal injection at <0.1 mL volumes. Ketorolac (Butler Schein, 30 mg/mL vials in 10% ethanol), was used at 50 mg/kg. Ketoconazole (Sigma Aldrich), was initially dissolved in 100% ethanol before being mixed with normal saline at 50:50 v/v and delivered at a concentration of 20 mg/kg. Carbenoxolone (Sigma-Aldrich) was dissolved in normal saline and delivered at concentrations of 100-150 mg/kg. Finally, indomethacin was dissolved in 100% ethanol before being mixed with normal saline at 10:90 v/v and delivered at concentrations ranging from 5-30 mg/kg.

Analysis methods: Overall, 5s and 1s stimulus evoked trials were averaged and compared before and after drug administration. Each experiment (i.e. before and after drug administration in an animal during a single imaging day) was considered as a separate n. For all statistical calculations (unless otherwise indicated), a paired, two-tailed Student's t-test was used to test for statistical significance. Unless otherwise indicated, all error bars and error patches on the time course data are ±SEM (standard error of the mean).

As will be described below, "central" and "peripheral" regions of interest (ROIs) were selected to demonstrate the effects of the pharmacological agents on the spatiotemporal properties of the hemodynamic response. Central ROIs were selected in the whisker barrel where there is a sustained GCaMP response, i.e., it has a fast offset at the end of a 5s sustained whisker stimulus. Peripheral ROIs are selected right outside the central region where there is no sustained GCaMP response, but there is a sustained hemodynamic response. Note that peripheral regions can be selected that are well outside the whisker barrel and also have no sustained hemodynamic response, these regions are considered to be well away from the vasculature immediately supplying the whisker barrel.

In most trials, the animal moves in response to the stimulus. In some cases, the animal continues to move (walk or run) for a large segment of the trial after stimulus onset, resulting in sustained GCaMP responses in the somatosensory cortex and sustained HbT responses that do not return to baseline by the end of the stimulus period. These trials were excluded from the pre- and post-data sets by averaging the last 5 seconds of each trial and setting an upper HbT threshold to exclude trials that did not return to baseline. This upper threshold was kept constant between the pre- and post- trials. Generally, the upper HbT threshold was adjusted until the trial-averaged time course average over the last 5 seconds was within 1 μM.

Deconvolution and NNLS fitting: As will be described below, HRFs (hemodynamic response functions) can be used to describe our data and test linearity, where

$$\boldsymbol{HbT(t) = GCaMP(t) \otimes HRF}$$

Since direct deconvolution often does not work to calculate HRFs, we instead use a diagonal loading least-squares deconvolution method described in (Ma, Shaik, Kozberg, et al., 2016) to calculate deconvolved HRFs.

Non-negative least squares (NNLS) fitting is used to visualize the spatial extent and manifestation of the different components of endothelium-dependent vasodilation described below. Each pixel was fitted to the three different components (EDHF, slow sustained vasodilation, slow local vasodilation) using the lsqnonneg fitting algorithm in MATLAB. Slow sustained vasodilation and slow local vasodilation are shown superimposed whereas EDHF-dependent vasodilation is shown separately.

5.2. The initial fast rise and subsequent sustained nature of the whisker stimulus-evoked response in the awake mouse

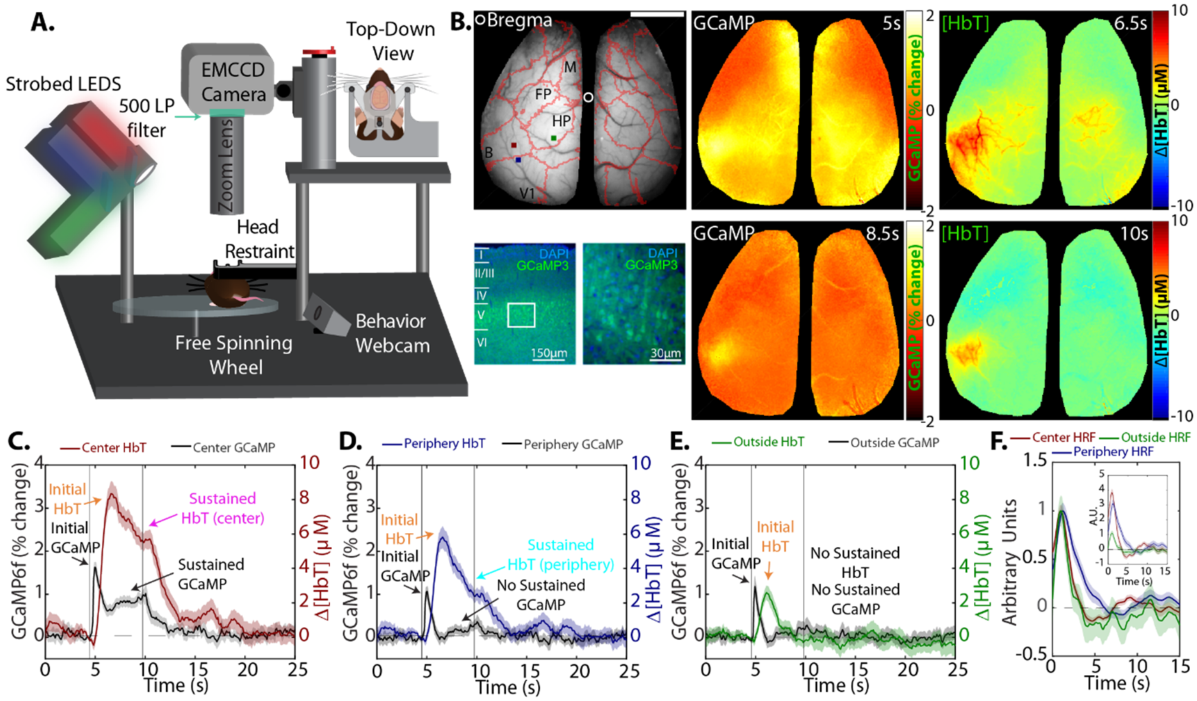

Fig 37. Wide-field optical mapping (WFOM) of the stimulus-evoked hemodynamic response (A) WFOM set-up. (B) Fluorescence image of a thinned-skull awake mouse, showing relevant brain regions: (B-barrel, V1-visual, HP-hindpaw, FP-forepaw, M-motor). Also shown are GCaMP and hemodynamic responses to a 5s stimulus during initial and sustained phases. (C, D, E) GCaMP and hemodynamic responses in the central, peripheral and "outside" region. (F) Deconvolved HRFs for those regions (scaled to peak value). Inset: Unscaled deconvolved HRFs.

A continuous whisker stimulus of 5 seconds in an awake mouse results in biphasic GCaMP and hemodynamic responses. Initially, neuronal activity increases in a somewhat global manner (the initial phase), recruiting areas of the brain responsible for processing and responding to the stimulus (Sreenivasan, Kyriakatos, Mateo, Jaeger, & Petersen, 2017), before localizing to the whisker barrel at a lower amplitude (the sustained phase). The hemodynamic response, on the other hand, initially shows strong recruitment of the entire surface artery feeding the whisker barrel, before also localizing to the whisker barrel during the sustained phase. This spatiotemporal behavior of stimulus-evoked blood flow has been observed previously with similar optical intrinsic signal imaging methods (Berwick et al., 2008a; C. Martin, Y. Zheng, N. R. Sibson, J. E. Mayhew, & J. Berwick, 2013). However, here we additionally observe that large initial vascular recruitment in other regions of the brain is not observed despite the global nature of the GCaMP response (**Fig 37**B). In addition, the sustained hemodynamic response over-extends the region of sustained neuronal activity. In the "central" region of stimulus-evoked activity, both GCaMP and hemodynamic responses have a sustained phase (**Fig 37**C). In the "peripheral" region, downstream of the surface artery feeding the whisker barrel, no sustained GCaMP activity is observed (**Fig 37**D), while there still exists a sustained hemodynamic response. In regions of the brain outside the area around the vessel supplying the whisker barrel, neither sustained GCaMP nor sustained hemodynamic activity is observed (**Fig 37**E). The spatiotemporal differences between neuronal and hemodynamic responses also result in the non-linearities observed in the hemodynamic response function (HRF) under stimulus-evoked conditions. While the shape of the deconvolved HRFs of the central region and "outside" region are similar, their amplitudes are very different. The deconvolved HRF in the periphery is wider than that in the center in concordance with the unexpected sustained hemodynamic response in the periphery (**Fig 37**F). We hypothesize that these phenomena arise from a contribution of endothelial-derived vasodilation to neurovascular coupling.

Similar to the rat experiments described before, we decided to inhibit slow calcium-wave dependent vasodilation in the mouse endothelium using ketorolac. However, instead of using enalaprilat to study fast vasodilation given its massive effects on blood pressure, we decided to use ketoconazole and carbenoxolone. Ketoconazole is a non-blood brain barrier permeable (Daneshmend & Warnock, 1988) cytochrome P450 (CYP-450) inhibitor previously shown to inhibit EDH-dependent vasodilation in human arterioles (Coats, Johnston, MacDonald, McMurray, & Hillier, 2001) and monkey cerebral arteries (Geddawy, Shimosato, Tawa, Imamura, & Okamura, 2010). CYP-450 variants have been shown to produce epoxy-eicosatrienoic acids (EETs) that activate calcium dependent potassium channels (KCa), initiating endothelial hyperpolarization (Spector, 2009). Ketoconazole was previously used to treat systemic and superficial fungal infections in humans (Gupta & Lyons, 2015). Its action is similarly limited to the vasculature, and would affect the initial increase in the hemodynamic response and recruitment of the surface vasculature. Carbenoxolone, a non-blood brain barrier permeable (Leshchenko, Likhodii, Yue, Burnham, & Perez Velazquez, 2006), non-specific gap junction inhibitor was used to ascertain the role of vascular gap junctions during conducted or propagated vasodilation (Behringer, Socha, Polo-Parada, & Segal, 2012). As a control for ketorolac, we additionally measured the effects of indomethacin, a blood brain barrier permeable, non-selective COX inhibitor.

5.3 Ketorolac and ketoconazole have different temporal and spatial effects on stimulus-evoked neurovascular coupling

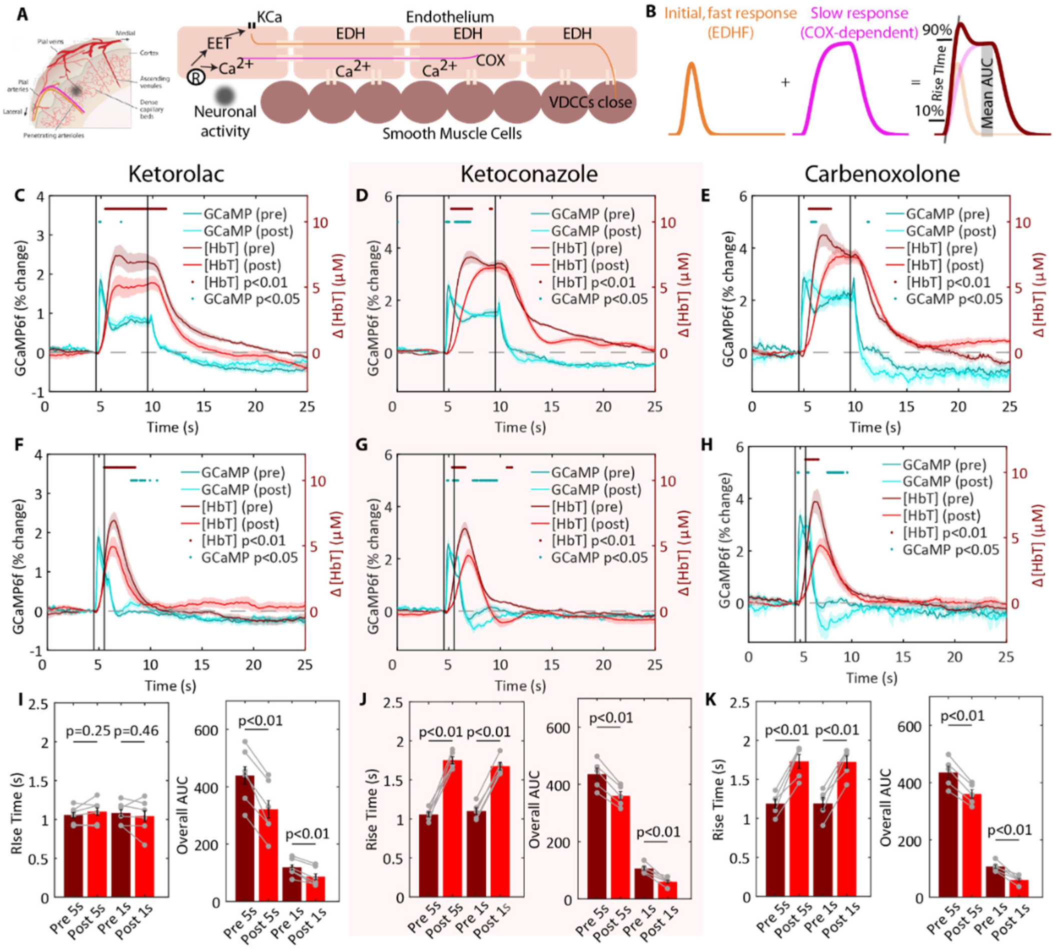

Fig 38. Ketorolac (n=6 recording sessions from 4 animals), ketoconazole (n=4 recording sessions from 4 animals) and carbenoxolone (n=5 recording sessions from 5 animals) have different spatiotemporal effects on the hemodynamic response. (A) Cross-section of the mouse cortex illustrating the organization of the vasculature including capillaries, diving arterioles and venules and surface arteries and veins. (B) Schematic illustrating dual mechanisms of endothelial vasodilation: long range EDH derived from EET activity on KCa channels that eventually inactivate voltage dependent calcium channels (VDCCs) and short-range Ca2+ wave dependent release of COX metabolites. (C) Illustration of the superposition of fast, long-range and slow, short range vasodilation. Also illustrated are the calculation for rise time and sustained HbT activity. (C, D, E) 5s stimulus evoked GCaMP and HbT responses for ketorolac, ketoconazole and carbenoxolone. (F, G, H) 1s stimulus evoked GCaMP and HbT responses for the the drugs. (I, J, K) Rise time and sustained mean HbT values for the three drugs.

In anticipation of the superposition of fast and slow vasodilation contributing to the overall HbT response, we measured the rise time and sustained amplitudes (towards the end of the response) of the HbT responses in the central region of stimulus-evoked activity (**Fig 38**B).

Ketorolac (COX inhibitor) significantly attenuates the amplitude of the stimulus-evoked HbT response, regardless of stimulus duration, without affecting the rise time of these responses. It has minimal effects on the evoked GCaMP activity (**Fig 38**C, F, I). Indomethacin has a similar effect on hemodynamic responses in the central region (Fig 46). Ketoconazole, the CYP-450 inhibitor (**Fig 38**D G, J) and carbenoxolone, the non-speciifc gap junction blocker (**Fig 38**E, H, K) on the other hand have remarkable effects on the initial rise of the HbT response for both 1s and 5s stimuli. Neither drug, however, has an effect on the sustained part of the hemodynamic response.

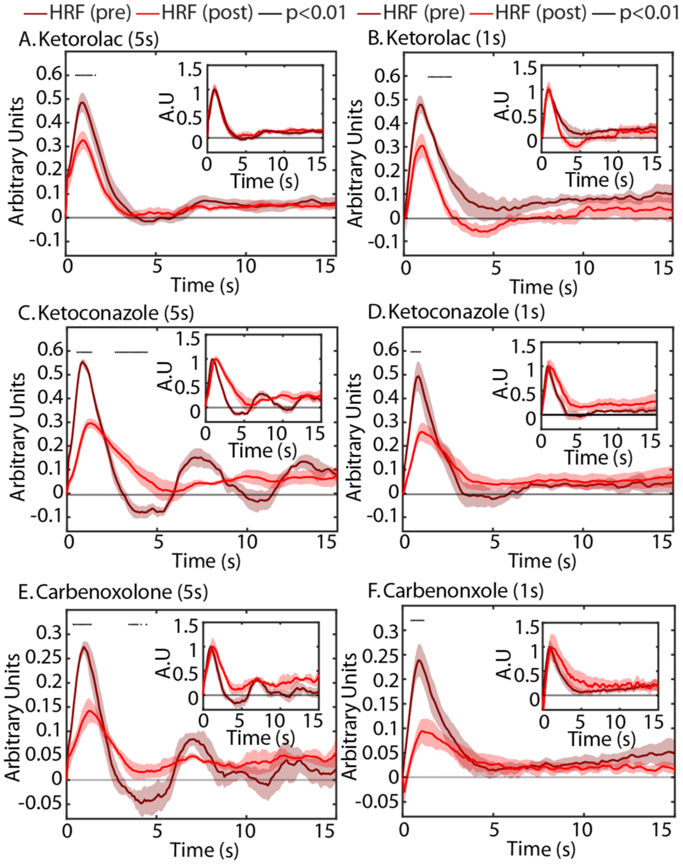

Fig 39. Deconvolved hemodynamic response functions (HRFs) for ketorolac (A, B), ketoconazole (C, D) and carbenoxolone (E, F) for 5s and 1s whisker stimuli.

Ketoconazole and carbenoxolone also have significant effects on the evoked GCaMP activity (albeit at p<0.05 & p>0.01). Neither drug affects the overall shape of the 5s GCaMP response; post-drug responses still show an increase in signal followed by a decrease to a sustained plateau for the duration of the whisker stimulation. However, the transition between peak and sustained values are significantly different.

To further explore the potential impact of this altered neural activity, we deconvolved the HbT and GCaMP responses for all three pharmacological agents (Fig 39). The deconvolved HRFs are all significantly different (p<0.01) after administration of ketorolac, ketoconazole and carbenoxolone, though each drug affects the HRFs in different ways. Ketorolac (and indomethacin) changes the amplitude of the HRF, while ketoconazole and carbenoxolone change both the amplitude and shape of the post-drug HRFs. This confirms that (1) small changes in

GCaMP activity, while relevant, are not responsible for the overall change in neurovascular coupling, and (2) there are different effects of ketorolac versus ketoconazole and carbenoxolone on the stimulus-evoked HbT response.

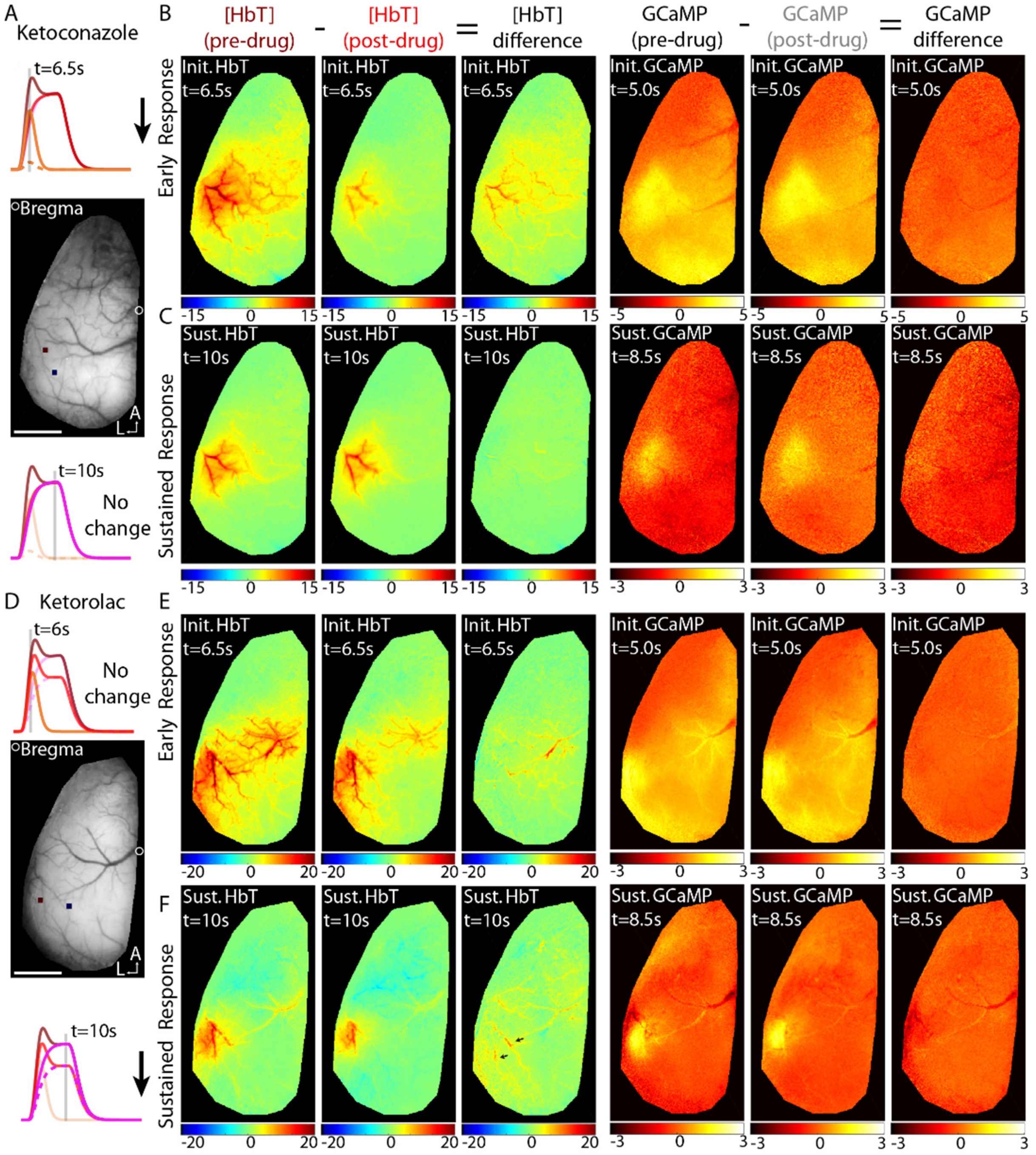

Fig 40. Distinct spatial effects of ketorolac and ketoconazole on the stimulus-evoked hemodynamic response. (A) Grayscale fluorescence image showing ROIs for central (red) and peripheral (blue) regions. Also shown are schematics for diminished early response and unaffected sustained responses after ketoconazole administration. Effect of ketoconazole on the early (B) and late (C) HbT and GCaMP responses. (D) Central (red) and peripheral (blue) ROI selections in another mouse. Also shown are

schematics for unchanged early response and diminished sustained responses after ketorolac administration. Effect of ketorolac on the early (E) and late (F) HbT and GCaMP responses. The decreased recruitment of downstream sections of surface artery after ketorolac administration during the sustained responses is highlighted (arrows).

These drugs also affect the spatial properties of the hemodynamic response in different ways (**Fig 40**). To demonstrate these spatial differences and to control for any spatial effect on GCaMP activity, we look at snapshots of activity at the beginning of the stimulus (GCaMP, t=5 s, HbT, t=6.5 s) and towards the end of the stimulus (GCaMP t=8.5 s, HbT t=10 s).

The HbT time points are chosen 1.5s ahead of the GCaMP responses given the 1-2s response time of HbT to the neuronal activity. Ketoconazole dramatically affects the initial spatial recruitment of the surface vasculature (**Fig 40**B), without affecting the initial spatial spread of the GCaMP activity. It has no effect on the sustained nature of either the HbT or GCaMP responses (**Fig 40**C). Carbenoxolone has a similar effect on the spatial spread of the initial recruitment of the surface vasculature without affecting the sustained response (not shown). Separately, ketorolac has no effect on the spatial spread of the early GCaMP or hemodynamic response (**Fig 40**E). The sustained HbT response, however, localizes more tightly to the whisker barrel (**Fig 40**F), while there is no observable change in the GCaMP signal localization. In **Fig 40**, the ROI selections for the central and peripheral regions are shown in the grayscale fluorescence images. The diminished recruitment of the downstream surface artery in the HbT response after ketorolac administration occurs in the peripheral region and will be further explored later.

To summarize, it is clear that these drugs have different spatiotemporal effects on the stimulus-evoked HbT response in the awake mouse. Consistent with their proposed action on fast, long range, EDH-dependent vasodilation, ketoconazole and carbenoxolone decrease the contribution of the surface arteries to fast vasodilation. Ketorolac, on the other hand, has no effect on the surface arterial recruitment, but rather the amplitude and localization of the sustained response, consistent with activity derived from COX activation of a slow Ca^{2+} wave.

As mentioned previously, we expect that these two components of vasodilation superimpose, implying that there exists an underlying non-linearity to the stimulus-evoked hemodynamic response. We therefore conducted further analysis to elucidate the nature of this non-linearity.

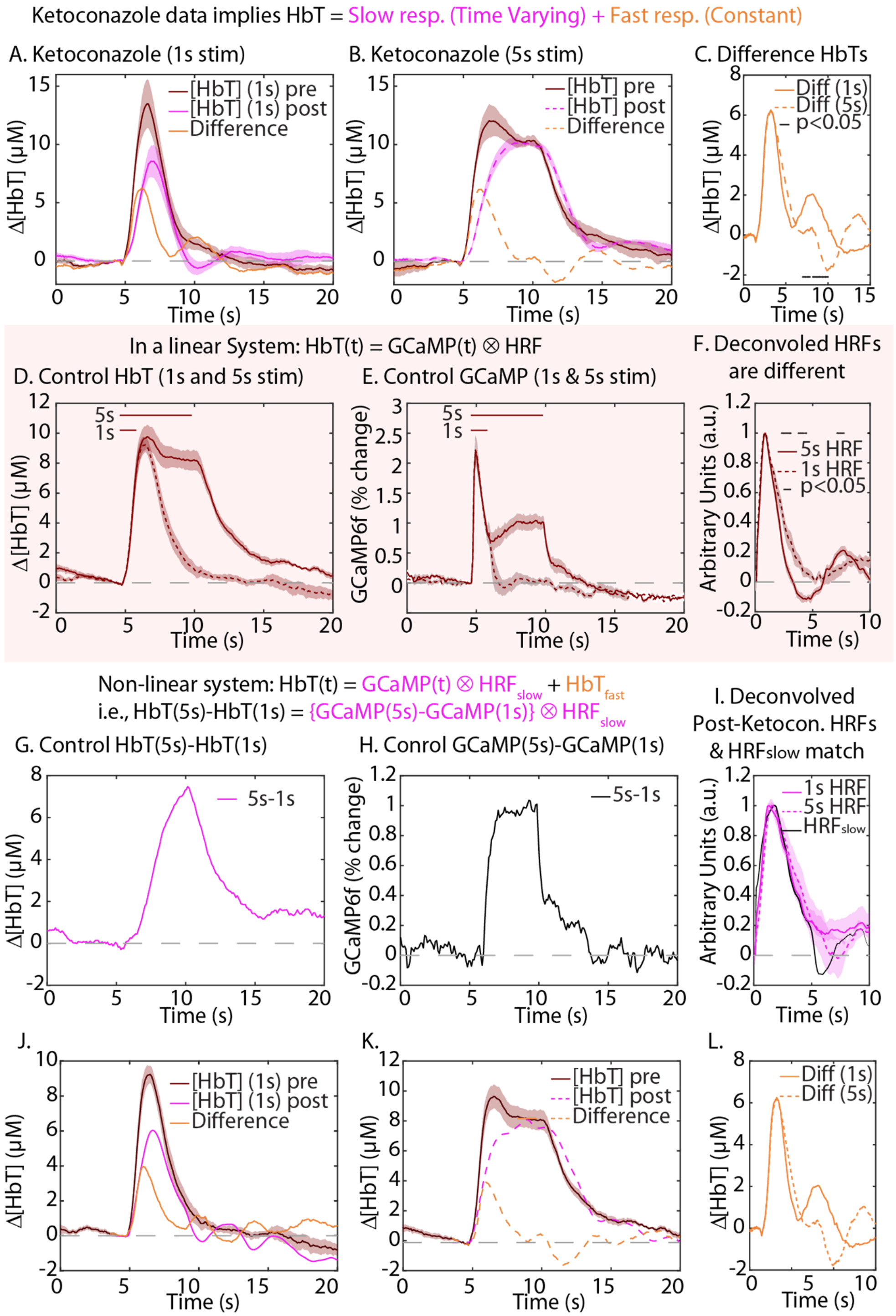

Fig 41. Linear System Hypothesis: The difference between the hemodynamic responses for both 1s and 5s stimuli (A, B) after ketoconazole administration is shown (C), implying a non-linear response. Deconvolution of control 5s and 1s data results in deconvolved HRFs that are different from each other (D-F). Subtracting the HbT responses (G) and the GCaMP responses (H) for control data and subsequently deconvolving results in an HRFslow identical to post-ketoconazole deconvolved HRFs (I). Reconvolving HRFslow with control GCaMP data reveals the slow and fast responses in the control data (J-L).

5.4. The central HbT response can be modeled as a superposition of a fast, stimulus-duration invariant HbT response and a slow, stimulus-duration dependent HbT response.

The component of the HbT response attenuated by ketoconazole is identical for 1s and 5s stimuli (**Fig 41**A-C). Hence the fast component of vasodilation appears to be stimulus duration-independent, suggesting that the fast component itself is the important non-linearity. In a truly linear system, the GCaMP input could simply be convolved with an HRF to obtain the HbT output response.

$$\boldsymbol{HbT(t) = GCaMP(t) \otimes HRF}$$

Equation 12

To prove whether the hemodynamic response is linear or not, we deconvolved control HbT data against evoked GCaMP activity for 1s and 5s stimuli. The resulting HRFs are significantly different from each other, confirming the non-linearity. So we proposed the following modification:

$$\boldsymbol{HbT(t) = GCaMP(t) \otimes HRF_{slow} + HbT_{fast}}$$

Equation 13

where the slow component of the hemodynamic response is a simple linear convolution with an HRF_{slow}, that adds linearly with the EDH-dependent HbT_{fast} to obtain the overall HbT response.

This formulation implies that:

$$\boldsymbol{HbT(5s) - HbT(1s) = [GCaMP(5s) - GCaMP(1s)] \otimes HRF_{slow}}$$

Equation 14

HRF_{slow} is therefore calculated by taking the difference between 5 second and 1 second HbT data and deconvolving against the difference between 5 second and 1 second GCaMP responses ((**Fig 41**D-E). The resulting HRF_{slow} is nearly identical to the deconvolved HRFs for the post-ketoconazole data (**Fig 41**F), consistent with ketoconazole eliminating HbT_{fast}. Finally, we can reconvolve HRF_{slow} with the GCaMP data (**Fig 41**J-K). These predicted slow responses appear remarkably similar to the post-ketoconazole HbT responses. The residual unexplained data (HbT_{fast}) is identical between the two stimulus durations, also consistent with the ketoconazole effect.

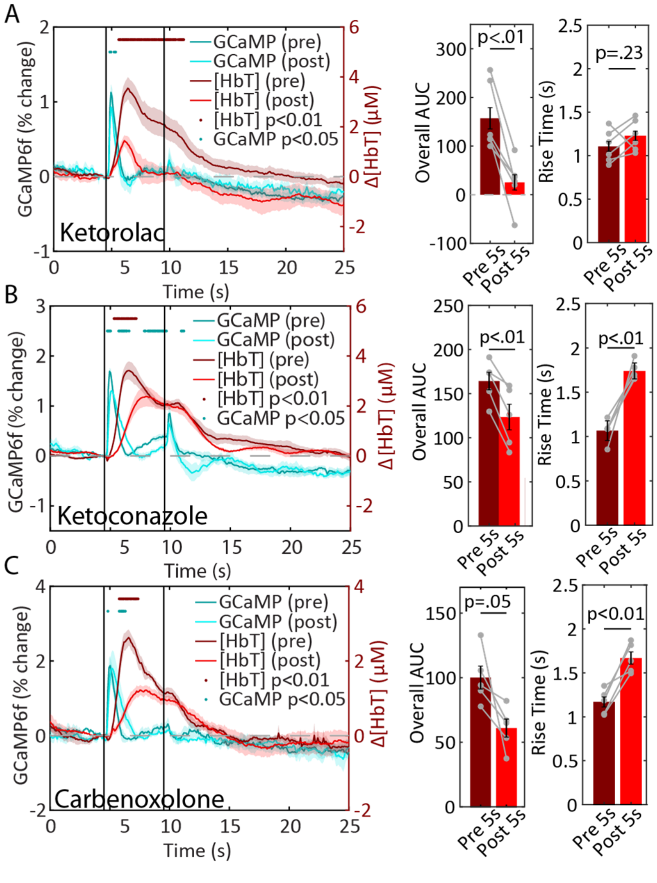

Fig 42. Peripheral responses. GCaMP and HbT responses with associated HbT rise times and sustained HbT amplitudes for ketorolac (A), ketoconazole (B) and carbenoxolone (C).

HRFs that vary as a function of stimulus duration, evident with long duration stimuli, have been observed previously in the human brain with fMRI (N. K. Logothetis, J. Pauls, M. Augath, T. Trinath, & A. Oeltermann, 2001) and in the rat barrel cortex with optical imaging (J. Martindale et al., 2005). Similar use of superimposed "initial" and "sustained" components (J. Martindale et al., 2005) have helped explain this phenomenon. However, our current results, in combination with previous results showing that light-dye mediated damage of the endothelium strongly attenuates the initial fast HbT response (B. R. Chen et al., 2014), confirms that the underlying biological mechanism responsible is EDH-dependent vasodilation.

We have also asserted that a slow calcium wave propagates along the endothelium over a short distance and results in COX-mediated vasodilation. In **Fig 37**D, we show that the HbT response in the periphery (outside the barrel cortex but downstream of the artery supplying the barrel) has a sustained phase, inconsistent with the lack of a sustained GCaMP response in the periphery and has a wide HRF (**Fig 37**F). A calcium wave that propagates from the whisker barrel, along the surface vasculature to outside the whisker barrel causing sustained vasodilation could account for this observation.

A more spatially-localized, sustained HbT response after ketorolac administration (**Fig 40**F), suggests that this sustained vasodilation in the periphery is affected. Hence we further analyzed the temporal properties of the peripheral region after our pharmacological manipulations.

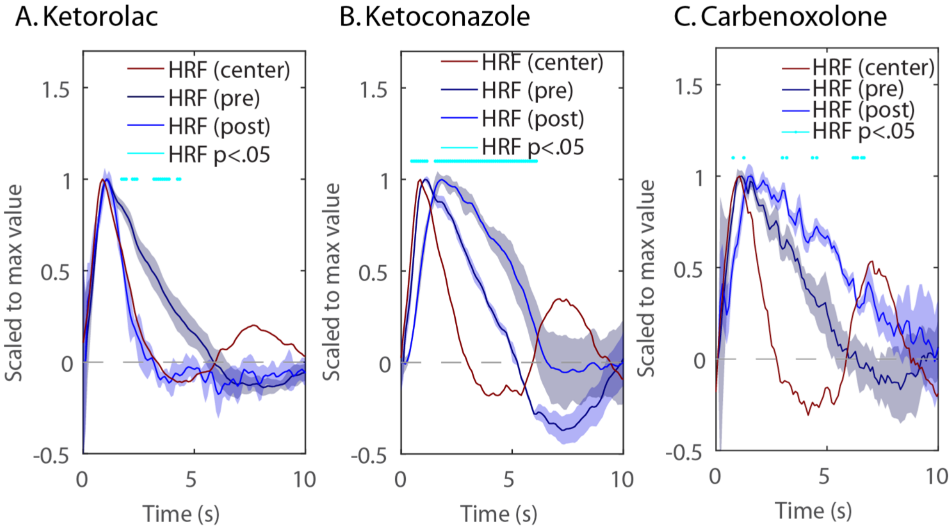

Fig 43. Peripheral HRFs. Deconvolved HRFs for ketorolac (A), ketoconazole (B) and carbenoxolone (C) in the periphery pre and post drug administration. Also shown in red are deconvolved central HRFs before drug administration.

5.5 Ketorolac attenuates the slow hemodynamic component of vasodilation and eliminates its propagation to the "periphery" of the responding cortical region.

Distinct from the effect of ketorolac in the central region, in the periphery it doesn't just attenuate the amplitude of the HbT response, but also eliminates the sustained component entirely (**Fig 42**A), without affecting the rise time of the peripheral response. Indomethacin has a similar effect on the peripheral hemodynamic responses to 5 second stimuli (Fig 46C). The shape of the deconvolved peripheral response after ketorolac administration shrinks and begins to appear similar to the deconvolved central HRF (Fig 43). Hence the spatial non-linearity observed in the periphery is introduced by slow propagated vasodilation and can be significantly attenuated with COX inhibition.

Ketoconazole and carbenoxolone (**Fig 42**B, C), attenuate the rise time of the peripheral HbT response, consistent with their effect on the recruitment of the entire surface artery that passes through the whisker barrel into the peripheral region during EDH-dependent vasodilation. They do not, however, affect the sustained component of vasodilation.

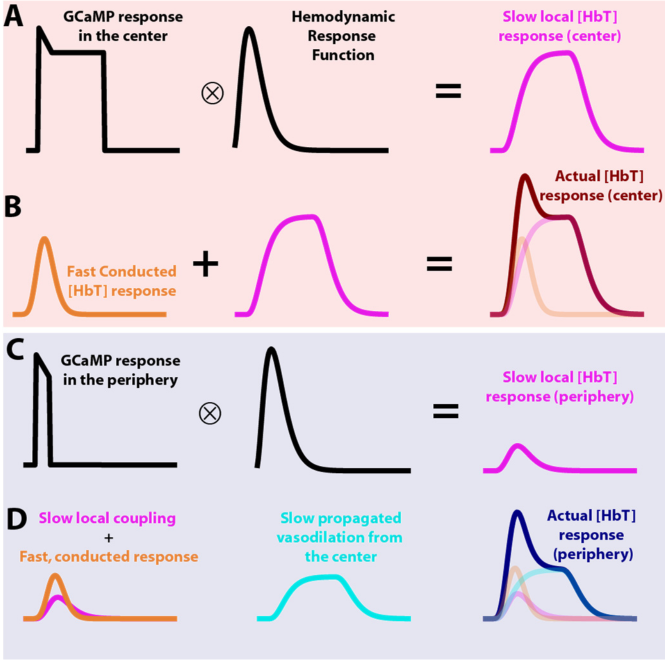

Fig 44. Complete model *(A) The central GCaMP response convolved with an HRF elicits the slow local HbT response. (B) The fast conducted response superimposes with the slow local response to obtain the full HbT response. (C) The peripheral GCaMP response when convolved with an HRF results in slow local coupling. (D) This superimposes with the fast conducted response and slow propagated vasodilation from the center to explain the peripheral HbT response.*

As before, changes in the GCaMP response do not account for the attenuation of fast HbT responses in the periphery, as evident from significantly different deconvolved HRFs (Fig 43). Based on these results, in addition to the central region's hemodynamic response,

Center: $\boldsymbol{HbT_c(t) = GCaMP_c(t) \otimes HRF_s + HbT_{fast}}$

Equation 15

we hypothesize that the hemodynamic response in the periphery consists of hyperpolarization dependent fast conducted vasodilation as well as endothelial calcium wave dependent slow propagated vasodilation, giving us:

Periphery: $\boldsymbol{HbT_p(t)} =$

$$\boldsymbol{GCaMP_p(t) \otimes HRF_s + HbT_{fast} + \mathrm{S}\,(GCaMP_c(t) \otimes HRF_s) + F\,\left(HbT_{fast}\right)}$$

Equation 16

Here, S (slow propagated vasodilation) and F (fast conducted vasodilation) are constants that dictate the extent to which fast, conducted and slow, propagated hemodynamic responses occur in the peripheral region in addition to the locally evoked neurovascular coupling, akin to the central region. The schematic for this complete model is shown in **Fig 44**. As for the analysis in the central region, we can take the difference of the peripheral HbT responses for 1s and 5s stimuli to obtain:

Peripheral Region: $\boldsymbol{HbT_p(5s) - HbT_p(1s)} =$

$$\boldsymbol{[GCaMP_p(5s) - GCaMP_p(1s)] \otimes HRF_s + \mathrm{S}\,([GCaMP_c(5s) - GCaMP_c(1s)] \otimes HRF_s)}$$

Equation 17

However, the peripheral GCaMP response does not include a sustained phase (**Fig 45**A, B). If these signals are identical, then we have:

Peripheral Region: $\boldsymbol{HbT_p(5s) - HbT_p(1s)} =$

$$\boldsymbol{\mathrm{S}\,([GCaMP_c(5s) - GCaMP_c(1s)] \otimes HRF_s)}$$

Equation 18

This analysis therefore allows us to ascertain exactly how much slow propagated vasodilation contributes to neurovascular coupling in the periphery. As shown in **Fig 45**C, in control data the differential peripheral HbT response (5s-1s, dotted line) is identical to a scaled version of the differential central HbT response (5s-1s, cyan), confirming the validity of the model. In addition, ketorolac fully attenuates the slow propagated component from the center to the periphery, i.e. the HbT response for a 5s stimulus is identical to the HbT response for a 1s stimulus (**Fig 45**D). The scaling factor was calculated by matching the peak amplitude of the central HbT differential response to the peripheral HbT differential response.

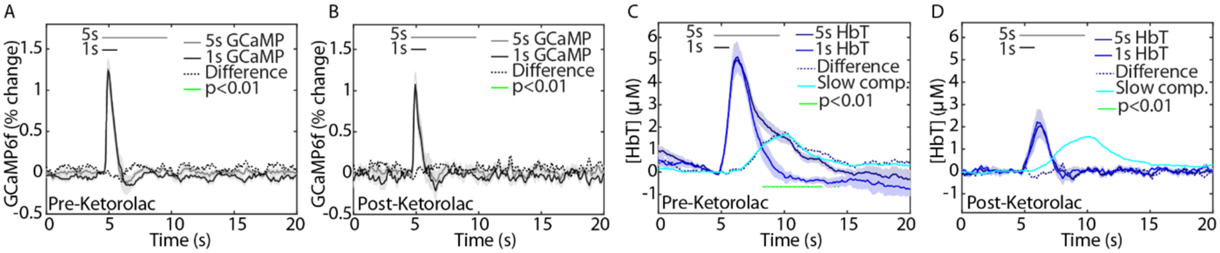

*Fig 45. Ketorolac attenuates the slow propagated component in the periphery (n=6 recording sessions from 4 animals)***.** *(A, B) Peripheral GCaMP responses before and after ketorolac administration are identical between 1s and 5s stimuli. (C) Before*

ketorolac administration the 5s stimulus response has a sustained phase, unlike the 1s response in the periphery (p<.001). Scaling the differential HbT (5s-1s) response from the center (cyan) matches the shape of the differential HbT (5s-1s) in the periphery (dotted blue). After ketorolac administration there is no sustained peripheral response in the 5s data, the peripheral HbT responses are identical between 1s and 5s stimuli.

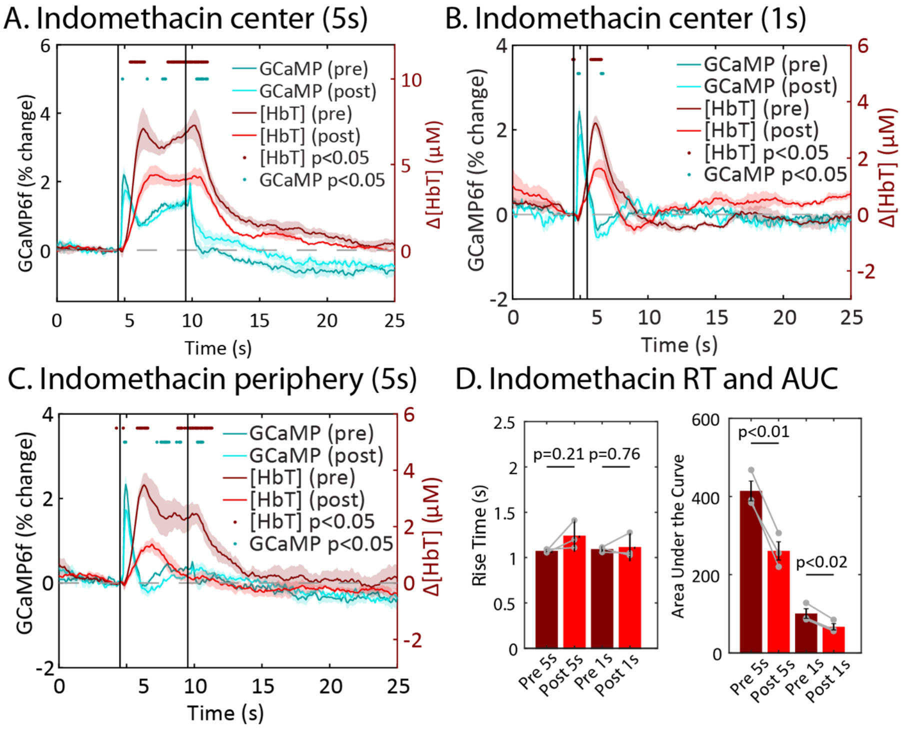

Fig 46. Effect of indomethacin (10 mg/kg) on neurovascular coupling (n=3 recording sessions from 3 animals). (A, B) Indomethacin significantly reduces the amplitude of hemodynamic responses in the center region (p<0.05) for both 1s and 5s hemodynamic responses, but also may have a small effect on neuronal activity. (C) Indomethacin has a significant effect on the sustained phase of the hemodynamic response in the periphery, similar to ketorolac (p<0.05). (D) Indomethacin has no effect on the rise time of the 1s or 5s central hemodynamic responses, whereas it significantly attenuates the average AUC for both 5s and 1s stimuli.

5.6 Visualization of the spatial extent of the model-derived fast and slow components of vasodilation.

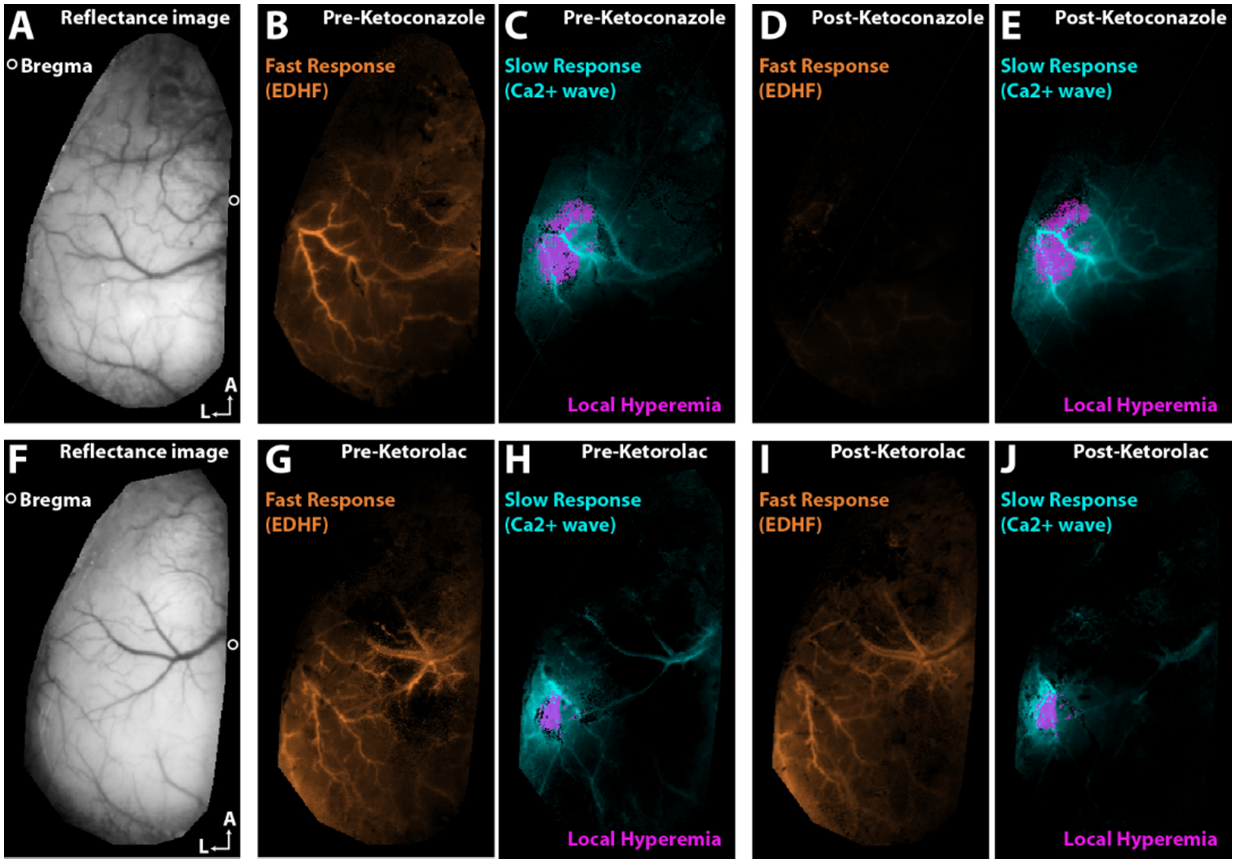

Fig 47. (A, F) Blue channel fluorescence images for two animals. (B, G) The fast hemodynamic response recruits the entire arterial tree supplying the whisker barrel. (C, H) Local hyperemia is shown in purple. The surrounding regions in cyan depicts pixels that are influenced by this local hyperemia during slow propagated vasodilation. (D, E) Ketoconazole attenuates the fast HbT response without affecting local or propagated coupling. (I, J) Ketorolac does not attenuate the fast response or local hyperemia, but limits the spatial extent of slow propagated vasodilation.

For a better visualization of these different components and their spatial extent, non-negative least squares (nnls) fitting was applied to each pixel in the datasets to scale fast and slow vasodilation components to their appropriate values. This results in spatial maps for fast conducted vasodilation and slow propagated vasodilation. In control data, fast conducted vasodilation dominates along the arterial tree supplying the whisker barrel (**Fig 47b, g**). To better visualize the extent of slow propagated vasodilation, only the local coupling of the central region is shown. The convolved slow HbT response from that region was used for all surrounding pixels in the nnls algorithm as their slow propagated component, which is superimposed with the region of local coupling in the central region. In control data, slow propagated vasodilation extends beyond the central region to the surrounding parenchyma and to some segments of the overlying arterial tree (**Fig 47c, h**). However, the spatial extent of this slow propagated component is much more restricted than the fast conducted component. Ketoconazole completely eliminates the fast conducted component, as expected, while having no effect on the extent of slow propagated vasodilation to the periphery (**Fig 47d, e**). Ketorolac on the other hand has no effect on fast conducted vasodilation, but as expected, restricts the extent of slow propagated vasodilation to the parenchyma just around the central region and prevents recruitment of distal segments of the overlying arterial tree (**Fig 47i, j**).

Now, fast conducted responses from the center are indistinguishable in shape from fast conducted responses evoked in the periphery. Hence, any conduction of vasodilation from the center would be encoded in the amplitude of the fast conducted component in each pixel. We therefore need a better method to measure the amplitude of both fast conducted and slow propagated responses that make up the spatial HbT response.

5.7 Along an arterial tree, fast conducted vasodilation manifests in the amplitude of the fast HbT response.

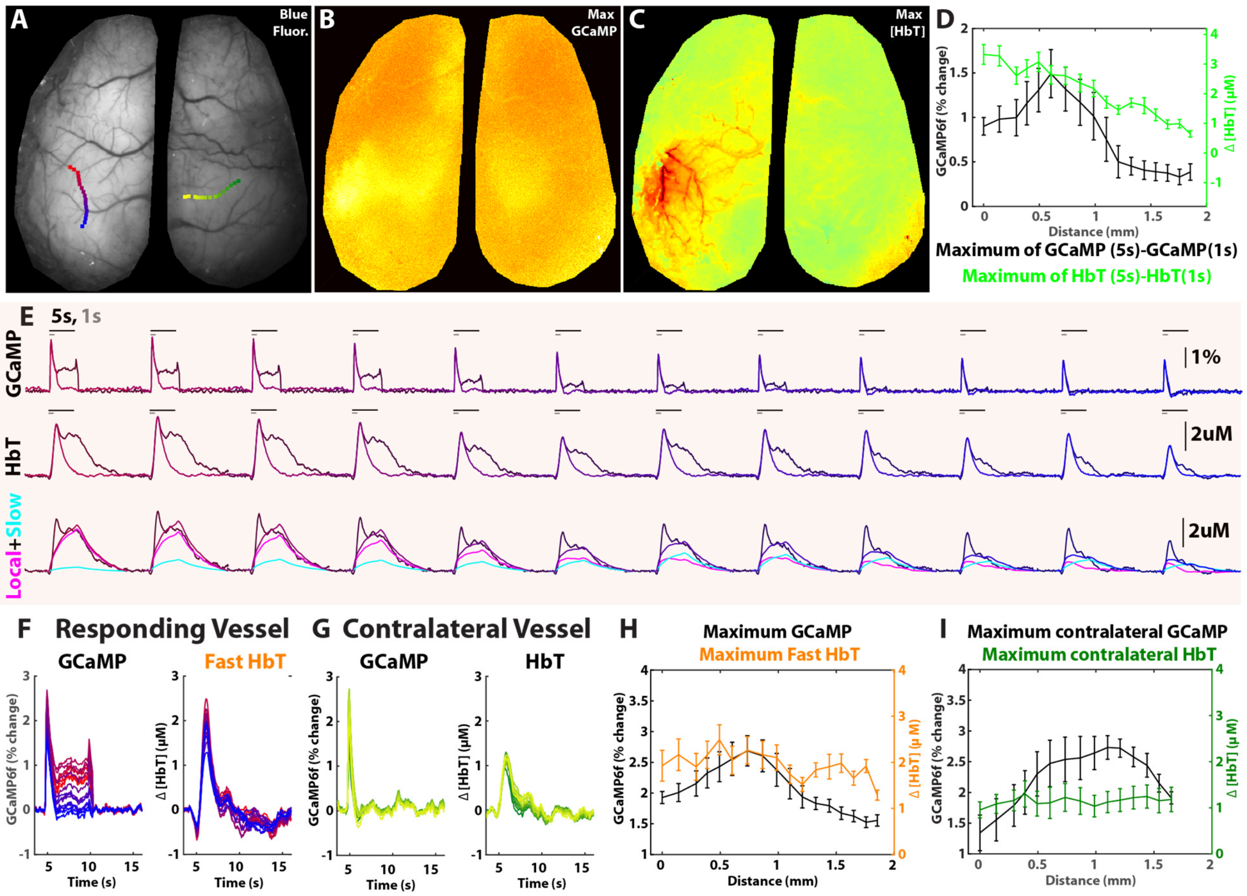

Fig 48. (A) Blue reflectance image with ROIs selected along the responding vessel in the whisker barrel on the left and a contralateral vessel on the right. (B) Maximum brain-wide GCaMP signal. (C) Maximum brain-wide HbT signal. (E) GCaMP and HbT signal in the ROIs along the responding vessel. Also shown are the superimposed slow local and propagated components of the hemodynamic response. (D) The maximum of the difference of the 1s and 5s GCaMP signal and the difference of the 1s and 5s HbT signal are shown on the same plot. (F) The responding region GCaMP response is shown alongside the fast HbT response from the responding vessel. The fast HbT response is calculated by removing the local and slow components from the original 5s HbT signal. (G) For reference, also shown are GCaMP and HbT traces from the contralateral side. (H) The maximum values of GCaMP and fast HbT responses are shown along the responding vessel. (I) Also, shown are the maximum values of the contralateral GCaMP and HbT values along the contralateral vessel.

We selected time courses along an arterial tree in a vessel in the whisker barrel and in a contralateral artery. For each location, we took the difference of the 5s and 1s GCaMP and hemodynamic signals. At the location where maximal GCaMP activity was occurring (the central region), we assumed to have purely local coupling, i.e. no slow propagation. For every other location, the slow propagation constant, SP was calculated as it was in **Fig 45**. The locally evoked hemodynamic response was calculated by convolving GCaMP activity with HRF$_{slow}$ at each location. HRF_{slow} itself was calculated by de-convolving the difference signals in the central region as in **Fig 41**. The local and slow components are shown alongside the original GCaMP activity and hemodynamic responses from the central region to the downstream arteriole in **Fig 48e**. The difference between the measured hemodynamic responses in every region and the local and slow propagated components, now precisely calculated, results in the pure HbT_{fast} components shown alongside the evoked GCaMP activity in **Fig 48f**. For reference, also shown are the GCaMP and hemodynamic responses on the contralateral side. On this side, fast GCaMP activity occurs with corresponding HbT responses without any sustained activity. Hence, on the contralateral side, we mostly expect fast HbT responses. By comparing these two sides, we see that HbT_{fast} on the responding side has higher amplitudes than HbT_{fast} on the contralateral side, despite having comparable GCaMP responses (**Fig 48h, i**). This strongly suggests that propagation of EDHF from the responding whisker barrel is encoded in the amplitude of the fast hemodynamic response. We therefore see that both fast conducted vasodilation and slow propagated vasodilation occur in the awake mouse under stimulus-evoked conditions, and can be pharmacologically inhibited using different drugs.

5.8 Relevance to fMRI

Hemodynamic signals in the human brain are usually measured with fMRI. Clinically, task-evoked fMRI is used for pre-operative brain mapping during neurosurgical procedures (Dimou, Battisti, Hermens, & Lagopoulos, 2013) to, for example, guide resections and appropriately place stimulus or probe electrodes. It's also used study "effective connectivity", i.e. the influence of activity in one neuronal system on another (K. J. Friston, 2011). This effective connectivity offers certain advantages over resting-state functional connectivity, for instance, the ability to better map direct axonal projections (Bauer et al., 2017). Task-evoked fMRI studies have been used to study alterations in cognitive function in schizophrenia (Zhou et al., 2014), Parkinson's disease (Ekman et al., 2014), Alzheimer's disease (Gordon et al., 2015), and neurodevelopment. Previously, it was shown that during development, the hemodynamic (HbT) response to positive changes in neuronal activity changes from predominantly negative (vasoconstrictive) to positive (vasodilatory), hence altering the interpretation of task-evoked fMRI studies conducted during development (Kozberg et al., 2016).

In adult neurovascular coupling, there are two issues to consider. Firstly, our studies suggest that effective connectivity mapping is certainly affected to some extent by the hemodynamic non-linearities imposed by endothelial-dependent vasodilation. In addition, in diseases like Alzheimer's (Csanyi et al., 2012; Kelleher & Soiza, 2013; L. Zhang, Papadopoulos, & Hamel, 2013) endothelial vasoactivity is altered. Even in subjects with normal cognitive function, endothelial dysfunction occurs in other contexts such as with cardiovascular (Rochette et al., 2013) metabolic disease (Virdis, Neves, Duranti, Bernini, & Taddei, 2013; J. Y. Zhang, Cao, Xu, & Edvinsson, 2006), and with aging (Toth et al., 2014). Now, while all this might confound fMRI signals to some extent, more importantly, purposefully altering endothelial function can be used as a tool to study both neuronal and neurovascular dysfunction. For example, drugs altering endothelial vasoactivity can be administered to subjects to study how the spatiotemporal properties of the fMRI signal change with and without appropriate endothelial function under different task-evoked paradigms. Pharmacological agents affecting endothelial have been used in several studies to assess peripheral vascular health (Casey & Joyner, 2011; Halcox, Narayanan, Cramer-Joyce, Mincemoyer, & Quyyumi, 2001; Kasprzak, Klosinska, & Drozdz, 2006) previously in humans – here similar experiments would be conducted in functional brain imaging studies. With these kind of experiments, we can not only begin to answer questions about hemodynamic non-linearities in fMRI, but also use them as an assay for studying neurovascular dysfunction in the healthy and diseased brain.

One concern remains. Our experiments so far assume that our pharmacological manipulations selectively targets the endothelium, but we have yet to provide evidence that the targeted mechanisms of vasodilation are active in the brain endothelium. Specifically, we focused on the expression of COX1 and COX2 in the brain endothelium, since few studies had properly checked for the expression of these molecules in the brain endothelium. In addition, there is a significant debate regarding the role of COX1 and COX2 in neurovascular coupling, which will also be discussed.

5.9 Expression of COX1 and COX2 in the brain

We now turn to the controversies regarding the vasoactivity of COX1 and COX2 during neurovascular coupling, and their cellular origin. Several neurovascular coupling studies have suggested that COX1 is expressed predominantly in astrocytes, while COX2 expresses in neurons (Lacroix et al., 2015; Mishra et al., 2014). COX1 expression in neurons and endothelial cells in the brain in different animal models has also been previously shown. Similarly COX2 expression in endothelial cells, is supported by literature on COX2 expression in endothelial cells of the brain (Table 1). What remains consistent across many studies, however, is that COX2 also always expresses in the soma of neurons, while excluding their nuclei. All these differing results suggest that selective inhibition of these molecules does not immediately guarantee that subsequent changes (or lack of changes) in hemodynamic activity in the brain can be ascribed to specific cell types in the brain.

Nevertheless, the differing roles of these cyclooxygenases in maintaining resting blood flow and inducing blood flow changes in response to external stimuli and systemic changes have been studied in detail. Some studies have shown that COX1 inhibition at high doses of the COX1-selective inhibitor SC-560 inhibit stimulus-evoked functional hyperemia (Liu, Li, Falck, Harder, & Koehler, 2012; Petzold, Albeanu, Sato, & Murthy, 2008), while others have shown no effect of selective COX1 inhibition at lower doses of the drug (Lecrux et al., 2011; Rosenegger et al., 2015). COX2 selective inhibition on the other hand has always been found to affect stimulus-evoked functional hyperemia with its strong expression in neuronal soma suggesting a neuronal origin of COX2 activity. In other experimental stimulus paradigms, COX1 activity appears to be often dependent upon calcium release (see Table 1) and exerts autoregulatory control over the brain vasculature. The differential expression of COX1 and COX2 in the vascular endothelium may help resolve some of the discrepancies in these findings – however, it would require using pharmaceuticals with low blood brain barrier permeability and high selectivity for one of the isoforms. Endothelial COX2 expression can also be selectively manipulated in acute inflammatory disease paradigms, which can be used to study not only the effect of COX2 expression in the endothelium, but also the effect of acute inflammation on neurovascular coupling in the brain.

Table 1. Cyclo-oxygenases in the brain – Expression patterns in neurons, astrocytes and endothelium. COX1 and COX2-dependent vasodilation has been studied under different experiment paradigms. The activation patterns under these paradigms in different experiments is also summarized.

	COX1 expression	**COX2 expression**
Neurons		^{Ms} (Lacroix et al., 2015)
Endothelium	Capillaries^{Ms} (Uekawa et al., 2016)	RNA-seq^{Ms} (Y. Zhang et al., 2014)
Astrocytes		RNA-seq^{Ms} (Y. Zhang et al., 2014)
	COX1 Activity	**COX2 activity**
Resting Blood Flow	^{Ms} (Niwa, Haensel, Ross, & Iadecola, 2001)	
Stimulus-Evoked Blood Flow		Vibrissa stim^{Ms} (Niwa et al., 2001) Visual stim^{H} (Hahn et al., 2011)
Calcium increase	Ca^{2+} ionophore^{Ms} (Niwa et al., 2001) Ca^{2+} uncaging^{Ms} (Takano et al., 2006)	
Acetylcholine		^{Ms} (Niwa et al., 2001)
Hypercapnia	^{Ms} (Niwa et al., 2001; Uekawa et al., 2016)	

Experiment in: Mouse (Ms) , Rat (R), Monkey (Mo) , Human (H)

5.10 Mechanisms of endothelium-derived vasodilation in the brain.

In this study we were able to demonstrate the existence of two separate mechanisms of endothelium-derived vasodilation with pharmacological inhibition of endothelial activity. However, the details of the pathways involved in fast EDH-dependent and slow calcium wave dependent vasodilation in the brain endothelium have yet to be fully elucidated. This involves studying the role of the different mediators of hyperpolarization – TRPV4 channels (Sonkusare et al., 2012; L. Zhang et al., 2013), endothelial IP3 receptors, calcium-dependent potassium channels (KCa) (Longden et al., 2011), Kir channels (Longden et al., 2017) and endothelial-endothelial and myo-endothelial gap junctions as well as the voltage dependent calcium channels in the smooth muscle cells. The initiation of the hyperpolarization cascade at and before the activation of cytochrome P450 and the relationship between EETs and hyperpolarization also need to be further explored. With respect to slow propagated vasodilation, using genetically encoded indicators of calcium activity in the endothelium, actual propagation of calcium waves in the endothelium *in vivo* needs to be observed. Separate from calcium waves, transient calcium events localized to myo-endothelial gap junctions (Earley & Brayden, 2015; Kansui, Garland, & Dora, 2008) might be involved in mediating hyperpolarization – hence it might be possible to visualize both components of endothelial dependent vasodilation with calcium imaging. Several studies have already observed calcium activity in the brain endothelium, however, calcium activity in the endothelium must be observed under physiological stimulus paradigms in awake animals.

5.11 SCAPE imaging for microscopic-level 3D volumetric imaging of endothelial-dependent vasodilation

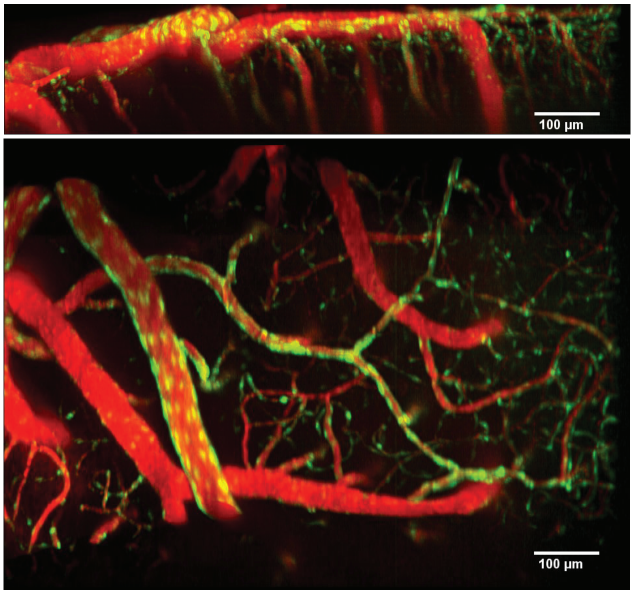

Fig 49 SCAPE imaging at 10 volumes per second in awake mouse brain during whisker stimulation. *Red = Texas red dextran, green = GFP in endothelial cells. Dilations of pial and diving arterioles can be clearly observed, even in single-trial data, allowing unique quantification of 3D vascular dynamics.*

SCAPE microscopy was developed in our lab in order to image three-dimensional volumes of tissue at high frame rates, making them ideal for simultaneous imaging of cortical vessels, diving vessels and capillaries during neurovascular coupling in the awake mouse in vivo. Recently, we have acquired mice expressing the GCaMP fluorophore cdh5-GCaMP8 in endothelial cells and are using SCAPE microscopy to observe simultaneous changes in GCaMP activity in the endothelium and changes in vessel diameter of diving arterioles and surface vessels. In order to visualize the lumen of these vessels, Texas-Red dextran, a fluorescent red dye that remains in the vasculature is injected intravenously during imaging. Hence, calcium changes in endothelial cells are visualized with green fluorescence while dilations are visualized with red fluorescence. I conducted preliminary experiments using Tie2-GFP mice (**Fig 49**), where the static GFP fluorophore is expressed in the endothelium. With SCAPE microscopy we are able to observe stimulus-evoked dilations on the surface vessels and in diving vessels 100-200 um below the cortical surface at over 10 volumes per second. Experiments in cdh5-GCaMP8 mice will be conducted in the future. Importantly, this imaging allows for a complete picture of the neurovascular unit – from capillaries to the surface vasculature, and will allow us to draw appropriate conclusions regarding the role of endothelial cells in neurovascular coupling at these various levels.

5.12 Behavioral manifestations of cognitive impairment arising from endothelial dysfunction in the mouse cortex

Finally, we have asserted that endothelial dysfunction can have cognitive effects. However, we haven’t yet quantified what those effects might be. To begin considering this issue, we were initially concerned that the whisker stimulus may sometimes cause startle responses, which engage pathways of vasodilation distinct from those used during normal evoked activity. Given that, in control animals, increases in pupil diameter during a whisker stimulus could be associated with a startle response in the animal, we decided to exploit our simultaneous pupillometry measurements to further explore the issue.

Pupil diameter changes measure changes are correlated with changes in locus coeruleus (LC) activity (Joshi, Li, Kalwani, & Gold, 2016) – the LC is a deep brain structure responsible for modulating arousal and wakefulness in the animal. The LC can have an important modulatory role on stimulus-evoked blood flow in the brain (Bekar, Wei, & Nedergaard, 2012; Toussay, Basu, Lacoste, & Hamel, 2013), hence making it important to isolate the effect of the LC on neurovascular coupling. However, by separating trials based on changes in pupil diameter (**Fig 50**), we show that initial increases in GCaMP activity and hemodynamics are unaffected between the two conditions, hence suggesting that fluctuations in arousal may not be important during neurovascular coupling.

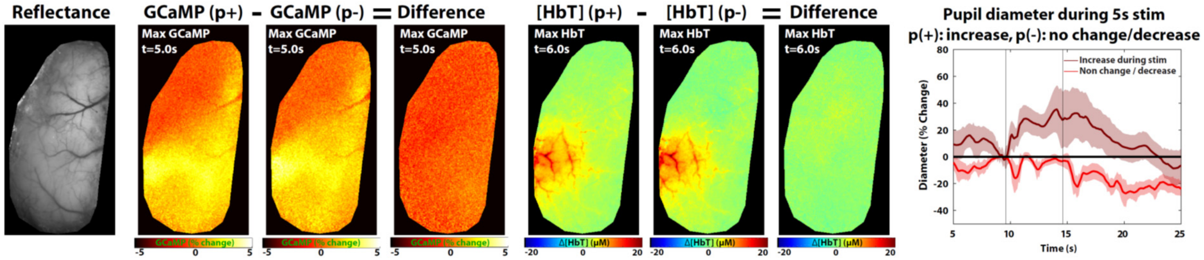

Fig 50. Pupil diameter changes “startle effect” has no effect on stimulus-evoked GCaMP or hemodynamic responses. Pupil diameters were measured in awake animals during a 5s whisker stimulus. Trials were separated into 2 groups: either where the pupil diameter increased, p(+) or where it decreased or did not change, p(-). The trial-averaged spatial spread of the neuronal or hemodynamic data does not change between the two groups during the early phase of the response. Hence we believe that pupil diameter increases arising from a startle reflex minimally affect stimulus-evoked responses.

Separately, we previously mentioned that only trials where the animal doesn't move during the stimulus period are analyzed. This is important because it is inappropriate to average data where the motion of the animal changes neuronal activity and hemodynamics in the cortex. However, this excluded data also provides an opportunity to measure the responsiveness of the animal to the whisker stimulus. The next step involves observing the animals' proclivity to begin moving and stay moving after stimulus onset. Changes in the animal's average responsivity to the whisker stimulus might manifest if endothelial dysfunction is affecting cognitive activity during our pharmacological manipulations in the short term.

One recent study found that decreased eNOS (endothelium nitric oxide synthase) activity in the brain endothelium and subsequent decreases in brain blood flow due to a high salt diet caused measurable changes in cognitive function (Faraco et al., 2018) after several weeks of a high salt diet. These changes were reversible, however, once the brain vascular activity returned to normal. Hence, while we may find that there are acute changes in cognitive function with our acute studies of pharmacological modulation of endothelial function, a more powerful and clinically relevant approach to studying the effect of endothelial dysfunction in our mice on cognitive performance is to do these studies longitudinally. This would involve significantly reducing the concentrations of the drugs used to clinically relevant levels, and administering them to the animals over several days (or months). Then, we can follow changes in neurovascular coupling, and cognitive performance, and carefully measure whether one occurs before the other.

We did quantify the acute effects of ketorolac, carbenoxolone and ketoconazole on the animals' response to the 5 second whisker stimulus. Given that ketoconazole and carbenoxolone reduced the rise time of the HbT response and fast hemodynamics, we hypothesized that this might affect the animals' physical response to the stimulus as opposed to ketorolac, which may have a small or different effect on the behavioral response. We quantified three parameters in this regard: the time taken after stimulus onset for the animal to move (start time), the total amount of time during the stimulus the animal spent moving (total time) as well as the number of trials where the animal had any physical response to the stimulus. The acquired webcam data was processed as follows: Each webcam frame was subtracted from the previous frame and the average standard deviation of the resulting image was calculated for each pair of frames during the stimulus. A threshold was set to determine whether or not the standard deviation of this differential frame was changing, which would occur if the animal moved. The three parameters were extracted from this thresholded webcam signal.

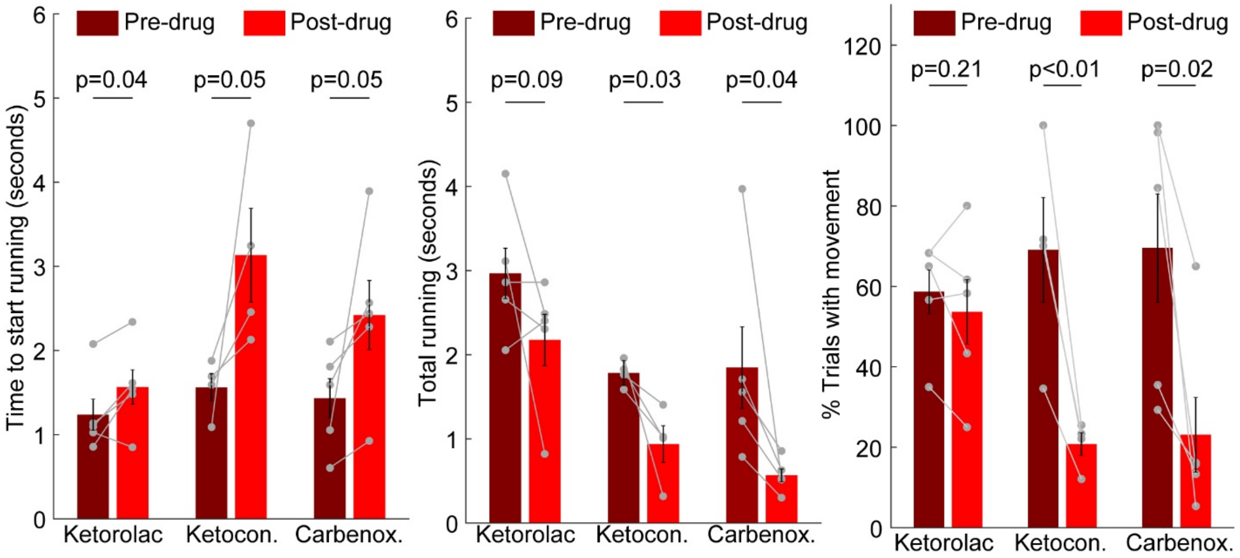

Fig 51. Acute behavioral effects of ketorolac, ketoconazole and carbenoxolone. Left: The time after stimulus onset at which the animal moves for the three drugs. Middle: The total amount of time during the stimulus that the animal is actively moving. Right: The percentage of trials during which the animal moved during the stimulus.

Ketorolac significantly increases the time to start running, but has no statistically significant effect on the overall time spent running or on the number of trials with movement. Ketoconazole and carbenoxolone dramatically increase the time to start running and also significantly attenuate the amount of time the animal spends running during the stimulus. In addition, ketoconazole and carbenoxolone significantly decrease the number of trials during which the animal had any physical response to the 5 second stimulus.

These results strongly suggest that the removal of the fast EDHF component during vasodilation has a dramatic effect on the animals' physical response to the stimulus. We hypothesize that the EDHF response allows for perhaps a metabolic potentiation of the brain and a change in neuronal excitability that allows for the animal to robustly respond to an external stimulus. The fast widespread hemodynamic response may therefore play a role in helping coordinate neuronal activity in separate regions of the brain. An attenuation of the slow component of vasodilation via ketorolac has an effect on the time to start running, but the relative magnitude of this effect is significantly smaller than that of ketoconazole or carbenoxolone. Several hypotheses can be derived to explain this effect – including an increase in the pain threshold and sensitivity of the whiskers to the stimulation, resulting in an altered response time.

Taken together, our results strongly suggest that alterations to the dynamic blood supply of the brain can have quite dramatic effects on brain activity and the behavioral manifestation of this activity, cementing our initial assumption that endothelial dysfunction will lead to changes in neurovascular coupling that will then have a direct consequence on brain function.

As mentioned earlier, new approaches to quantifying the exact sequence of events as well as the underlying metabolic and neuronal changes that result from changes in endothelial dependent vasodilation need to be further explored in the context of both acute, severe endothelial dysfunction as well as more subtle, chronic insults to the brain endothelium seen in several systemic disease states and in neurological disorders.

Summary and Future Studies

In this work, we set out to study the contribution of the brain endothelium to neurovascular coupling in the brain. The overwhelming evidence linking vascular dysfunction to impaired brain health motivated us to understand the mechanisms of endothelium-dependent vasodilation and to test whether they were active in the brain. We theorized that fast EDHF and slow, calcium-wave (COX) dependent mechanisms of endothelial vasodilation, as seen in peripheral vasculature, were also active during neurovascular coupling. Our experiments in anesthetized rats with light-dye mediated damage of the endothelium, pharmacological manipulation of COX activity, as well as experiments with ACE inhibition and calcium channel blockade gave us several clues regarding the spatiotemporal properties of the stimulus-evoked hemodynamic response and the role of the endothelium in the evolution of this response.

We needed a better experimental paradigm, however, to study neurovascular coupling – one where we could adequately control for changes in neuronal activity and a model where the effects of changing anesthetic depths on neuronal activity, brain and systemic blood flow were accounted for. Previous studies of whisker-stimulus evoked hemodynamics in awake mice, and thinned-skull preparations for long-term imaging were promising, leading us to develop our own imaging system (WFOM) and brain-wide thinned-skull preparation for conducting experiments in awake behaving Thy1-GCaMP mice. We developed correction methods to extract the true neuronal signal from the measured fluorescence signal, which is contaminated with hemodynamic artifacts. We developed analysis tools to appropriately quantify neurovascular coupling via hemodynamic response functions (HRFs), and validated them in our observations of resting state neuronal activity and hemodynamics in the brain.

Using our new experimental paradigm and analysis tools, we returned to studying endothelial mechanisms of vasodilation in the mouse brain. Ketorolac (a non-BBB permeable COX inhibitor), reduced the amplitude of hemodynamic responses in the whisker barrel, whereas ketoconazole (a non-BBB permeable CYP-450 inhibitor) altered the rate of change of hemodynamic responses, suggesting that it inhibited fast EDH-dependent vasodilation. Using deconvolved HRFs, we found that there is a non-linearity in the neurovascular coupling response that is stimulus-duration dependent – a fast hemodynamic response that occurs at the beginning of the overall hemodynamic response. We found that this non-linearity disappeared after ketoconazole administration, and that it was a stimulus-duration independent response that manifested strongly in the surface arterial vasculature. The properties of this fast response are therefore consistent with EDH-dependent vasodilation.

In addition to ketorolac diminishing the amplitude of the hemodynamic response in the whisker barrel, it eliminated the propagation of the sustained hemodynamic response to the periphery of the whisker barrel, which is consistent with this sustained response originating from a traveling calcium wave. Future experiments studying calcium waves in the brain vascular endothelium during neurovascular coupling are needed to confirm that this mechanism of vasodilation is active in the brain.

Finally, variants of the pharmacological drugs we used for our experiments are used clinically for a variety of reasons, one of which includes purposeful manipulation of systemic endothelial function. Our experiments suggest that adequate overall vascular health is required for normal neurovascular coupling and blood flow in the brain. Our observations, coupled with reports of cognitive function changes in rodent models with endothelial insults, strongly suggest that normal neuronal function relies significantly on a normal vasculature and a healthy endothelium.

Future experiments that carefully explore alterations to neuronal activity in the brain as a direct result of endothelial dysfunction, as well as downstream effects on cognitive function will help us fully understand the consequences of impaired vasoactivity on brain health. With the WFOM system, simultaneous experiments testing changes in neuronal activity and behavior can be conducted – by implementing task paradigms while imaging the animal instead of using a passive whisker stimulus paradigm. In addition, better methods of direct manipulation of brain endothelial vasoactivity (for example, optogenetic tools) can be used to mitigate confounds associated with systemic manipulation of endothelial function.

References

Allen, G. S., Ahn, H. S., Preziosi, T. J., Battye, R., Boone, S. C., Boone, S. C., . . . Transou, C. R. (1983). Cerebral arterial spasm--a controlled trial of nimodipine in patients with subarachnoid hemorrhage. *N Engl J Med, 308*(11), 619-624. doi: 10.1056/NEJM198303173081103

Attwell, D., Mishra, A., Hall, C. N., O'Farrell, F. M., & Dalkara, T. (2016). What is a pericyte? *J Cereb Blood Flow Metab, 36*(2), 451-455. doi: 10.1177/0271678X15610340

Bakalova, R., Matsuura, T., & Kanno, I. (2002). The cyclooxygenase inhibitors indomethacin and Rofecoxib reduce regional cerebral blood flow evoked by somatosensory stimulation in rats. *Exp Biol Med (Maywood), 227*(7), 465-473.

Baraghis, E., Devor, A., Fang, Q., Srinivasan, V. J., Wu, W., Lesage, F., . . . Sakadzic, S. (2011). Two-photon microscopy of cortical NADH fluorescence intensity changes: correcting contamination from the hemodynamic response. *J Biomed Opt, 16*(10), 106003. doi: 10.1117/1.3633339

Bauer, A. Q., Kraft, A. W., Baxter, G. A., Wright, P. W., Reisman, M. D., Bice, A. R., . . . Culver, J. P. (2017). Effective Connectivity Measured Using Optogenetically Evoked Hemodynamic Signals Exhibits Topography Distinct from Resting State Functional Connectivity in the Mouse. *Cereb Cortex*, 1-17. doi: 10.1093/cercor/bhx298

Bederson, J. B., Connolly, E. S., Jr., Batjer, H. H., Dacey, R. G., Dion, J. E., Diringer, M. N., . . . American Heart, A. (2009). Guidelines for the management of aneurysmal subarachnoid hemorrhage: a statement for healthcare professionals from a special writing group of the Stroke Council, American Heart Association. *Stroke, 40*(3), 994-1025. doi: 10.1161/STROKEAHA.108.191395

Behringer, E. J., Socha, M. J., Polo-Parada, L., & Segal, S. S. (2012). Electrical conduction along endothelial cell tubes from mouse feed arteries: confounding actions of glycyrrhetinic acid derivatives. *Br J Pharmacol, 166*(2), 774-787. doi: 10.1111/j.1476-5381.2011.01814.x

Bekar, L. K., Wei, H. S., & Nedergaard, M. (2012). The locus coeruleus-norepinephrine network optimizes coupling of cerebral blood volume with oxygen demand. *J Cereb Blood Flow Metab, 32*(12), 2135-2145. doi: 10.1038/jcbfm.2012.115

Berwick, J., Johnston, D., Jones, M., Martindale, J., Martin, C., Kennerley, A. J., . . . Mayhew, J. E. (2008a). Fine detail of neurovascular coupling revealed by spatiotemporal analysis of the hemodynamic response to single whisker stimulation in rat barrel cortex. *J Neurophysiol, 99*(2), 787-798. doi: 10.1152/jn.00658.2007

Berwick, J., Johnston, D., Jones, M., Martindale, J., Martin, C., Kennerley, A. J., . . . Mayhew, J. E. W. E. W. (2008b). Fine Detail of Neurovascular Coupling Revealed by Spatiotemporal

Analysis of the Hemodynamic Response to Single Whisker Stimulation in Rat Barrel Cortex. *Journal of Neurophysiology, 99*, 787-798. doi: 10.1152/jn.00658.2007

Blinder, P., Tsai, P. S., Kaufhold, J. P., Knutsen, P. M., Suhl, H., & Kleinfeld, D. (2013). The cortical angiome: an interconnected vascular network with noncolumnar patterns of blood flow. *Nat Neurosci, 16*(7), 889-897. doi: 10.1038/nn.3426

Bonder, D. E., & McCarthy, K. D. (2014). Astrocytic Gq-GPCR-linked IP3R-dependent Ca2+ signaling does not mediate neurovascular coupling in mouse visual cortex in vivo. *J Neurosci, 34*(39), 13139-13150. doi: 10.1523/JNEUROSCI.2591-14.2014

Bouchard, M. B., Chen, B. R., Burgess, S. A., & Hillman, E. M. (2009). Ultra-fast multispectral optical imaging of cortical oxygenation, blood flow, and intracellular calcium dynamics. *Opt Express, 17*(18), 15670-15678. doi: 10.1364/OE.17.015670

Boynton, G. M., Engel, S. A., Glover, G. H., & Heeger, D. J. (1996). Linear systems analysis of functional magnetic resonance imaging in human V1. *J Neurosci, 16*(13), 4207-4221.

Boynton, G. M., Engel, S. A., Glover, G. H., & Heeger, D. J. (1996). Linear systems analysis of functional magnetic resonance imaging in human V1. *The journal of neuroscience, 16*(13), 4207-4221.

Brennan, A. M., Connor, J. A., & Shuttleworth, C. W. (2006). NAD(P)H fluorescence transients after synaptic activity in brain slices: predominant role of mitochondrial function. *J Cereb Blood Flow Metab, 26*(11), 1389-1406. doi: 10.1038/sj.jcbfm.9600292

Buckley, M. M., & Brogden, R. N. (1990). Ketorolac. A review of its pharmacodynamic and pharmacokinetic properties, and therapeutic potential. *Drugs, 39*(1), 86-109.

Buxton, R. B., Wong, E. C., & Frank, L. R. (1998). Dynamics of blood flow and oxygenation changes during brain activation: the balloon model. *Magnetic resonance in medicine, 39*(6), 855-864.

Cardoso, M. M., Sirotin, Y. B., Lima, B., Glushenkova, E., & Das, A. (2012). The neuroimaging signal is a linear sum of neurally distinct stimulus- and task-related components. *Nat Neurosci, 15*(9), 1298-1306. doi: 10.1038/nn.3170

Casey, D. P., & Joyner, M. J. (2011). Prostaglandins do not contribute to the nitric oxide-mediated compensatory vasodilation in hypoperfused exercising muscle. *Am J Physiol Heart Circ Physiol, 301*(1), H261-268. doi: 10.1152/ajpheart.00222.2011

Chauvette, S., Volgushev, M., & Timofeev, I. (2010). Origin of active states in local neocortical networks during slow sleep oscillation. *Cereb Cortex, 20*(11), 2660-2674. doi: 10.1093/cercor/bhq009

Chen, B. R., Bouchard, M. B., McCaslin, A. F., Burgess, S. A., & Hillman, E. M. (2011). High-speed vascular dynamics of the hemodynamic response. *Neuroimage, 54*(2), 1021-1030. doi: 10.1016/j.neuroimage.2010.09.036

Chen, B. R., Kozberg, M. G., Bouchard, M. B., Shaik, M. A., & Hillman, E. M. (2014). A critical role for the vascular endothelium in functional neurovascular coupling in the brain. *J Am Heart Assoc, 3*(3), e000787. doi: 10.1161/JAHA.114.000787

Chen, T. W., Wardill, T. J., Sun, Y., Pulver, S. R., Renninger, S. L., Baohan, A., . . . Kim, D. S. (2013). Ultrasensitive fluorescent proteins for imaging neuronal activity. *Nature, 499*(7458), 295-300. doi: 10.1038/nature12354

Coats, P., Johnston, F., MacDonald, J., McMurray, J. J., & Hillier, C. (2001). Endothelium-derived hyperpolarizing factor : identification and mechanisms of action in human subcutaneous resistance arteries. *Circulation, 103*(12), 1702-1708.

Constantinople, C. M., & Bruno, R. M. (2011). Effects and mechanisms of wakefulness on local cortical networks. *Neuron, 69*(6), 1061-1068. doi: 10.1016/j.neuron.2011.02.040

Csanyi, G., Gajda, M., Franczyk-Zarow, M., Kostogrys, R., Gwozdz, P., Mateuszuk, L., . . . Chlopicki, S. (2012). Functional alterations in endothelial NO, PGI(2) and EDHF pathways in aorta in ApoE/LDLR-/- mice. *Prostaglandins Other Lipid Mediat, 98*(3-4), 107-115. doi: 10.1016/j.prostaglandins.2012.02.002

Daneshmend, T. K., & Warnock, D. W. (1988). Clinical Pharmacokinetics of Ketoconazole. *Clin Pharmacokinet, 14*(1), 13-34. doi: Doi 10.2165/00003088-198814010-00002

Destexhe, A., & Contreras, D. (2006). Neuronal computations with stochastic network states. *Science, 314*(5796), 85-90. doi: 10.1126/science.1127241

Destexhe, A., Contreras, D., & Steriade, M. (1999). Spatiotemporal analysis of local field potentials and unit discharges in cat cerebral cortex during natural wake and sleep states. *J Neurosci, 19*(11), 4595-4608.

Devor, A., Dunn, A. K., Andermann, M. L., Ulbert, I., Boas, D. A., & Dale, A. M. (2003). Coupling of total hemoglobin concentration, oxygenation, and neural activity in rat somatosensory cortex. *Neuron, 39*(2), 353-359.

Dimou, S., Battisti, R. A., Hermens, D. F., & Lagopoulos, J. (2013). A systematic review of functional magnetic resonance imaging and diffusion tensor imaging modalities used in presurgical planning of brain tumour resection. *Neurosurg Rev, 36*(2), 205-214; discussion 214. doi: 10.1007/s10143-012-0436-8

Domeier, T. L., & Segal, S. S. (2007). Electromechanical and pharmacomechanical signalling pathways for conducted vasodilatation along endothelium of hamster feed arteries. *J Physiol, 579*(Pt 1), 175-186. doi: 10.1113/jphysiol.2006.124529

Dunn, A. K. (2012). Laser speckle contrast imaging of cerebral blood flow. *Ann Biomed Eng, 40*(2), 367-377. doi: 10.1007/s10439-011-0469-0

Dunn, A. K., Bolay, H., Moskowitz, M. A., & Boas, D. A. (2001). Dynamic imaging of cerebral blood flow using laser speckle. *J Cereb Blood Flow Metab, 21*(3), 195-201. doi: 10.1097/00004647-200103000-00002

Earley, S., & Brayden, J. E. (2015). Transient receptor potential channels in the vasculature. *Physiol Rev, 95*(2), 645-690. doi: 10.1152/physrev.00026.2014

Ekman, U., Eriksson, J., Forsgren, L., Domellof, M. E., Elgh, E., Lundquist, A., & Nyberg, L. (2014). Longitudinal changes in task-evoked brain responses in Parkinson's disease patients with and without mild cognitive impairment. *Front Neurosci, 8*, 207. doi: 10.3389/fnins.2014.00207

Faraco, G., Brea, D., Garcia-Bonilla, L., Wang, G., Racchumi, G., Chang, H., . . . Iadecola, C. (2018). Dietary salt promotes neurovascular and cognitive dysfunction through a gut-initiated TH17 response. *Nat Neurosci*. doi: 10.1038/s41593-017-0059-z

Figueroa, X. F., & Duling, B. R. (2008). Dissection of two Cx37-independent conducted vasodilator mechanisms by deletion of Cx40: electrotonic versus regenerative conduction. *Am J Physiol Heart Circ Physiol, 295*(5), H2001-2007. doi: 10.1152/ajpheart.00063.2008

Filosa, J. A., Morrison, H. W., Iddings, J. A., Du, W., & Kim, K. J. (2016). Beyond neurovascular coupling, role of astrocytes in the regulation of vascular tone. *Neuroscience, 323*, 96-109. doi: 10.1016/j.neuroscience.2015.03.064

Friston, K. J. (2011). Functional and effective connectivity: a review. *Brain Connect, 1*(1), 13-36. doi: 10.1089/brain.2011.0008

Friston, K. J., Mechelli, A., Turner, R., & Price, C. J. (2000). Nonlinear responses in fMRI: the Balloon model, Volterra kernels, and other hemodynamics. *Neuroimage, 12*(4), 466-477.

Galeffi, F., Somjen, G. G., Foster, K. A., & Turner, D. A. (2011). Simultaneous monitoring of tissue PO2 and NADH fluorescence during synaptic stimulation and spreading depression reveals a transient dissociation between oxygen utilization and mitochondrial redox state in rat hippocampal slices. *J Cereb Blood Flow Metab, 31*(2), 626-639. doi: 10.1038/jcbfm.2010.136

Geddawy, A., Shimosato, T., Tawa, M., Imamura, T., & Okamura, T. (2010). Mechanism underlying endothelium-dependent relaxation by 2-methylthio-ADP in monkey cerebral artery. *J Pharmacol Sci, 114*(2), 180-188.

Gentet, L. J., Avermann, M., Matyas, F., Staiger, J. F., & Petersen, C. C. (2010). Membrane potential dynamics of GABAergic neurons in the barrel cortex of behaving mice. *Neuron, 65*(3), 422-435. doi: 10.1016/j.neuron.2010.01.006

Gordon, B. A., Zacks, J. M., Blazey, T., Benzinger, T. L., Morris, J. C., Fagan, A. M., . . . Balota, D. A. (2015). Task-evoked fMRI changes in attention networks are associated with preclinical Alzheimer's disease biomarkers. *Neurobiol Aging, 36*(5), 1771-1779. doi: 10.1016/j.neurobiolaging.2015.01.019

Gupta, A. K., & Lyons, D. C. (2015). The Rise and Fall of Oral Ketoconazole. *J Cutan Med Surg, 19*(4), 352-357. doi: 10.1177/1203475415574970

Hahn, T., Heinzel, S., Plichta, M. M., Reif, A., Lesch, K. P., & Fallgatter, A. J. (2011). Neurovascular coupling in the human visual cortex is modulated by cyclooxygenase-1 (COX-1) gene variant. *Cereb Cortex, 21*(7), 1659-1666. doi: 10.1093/cercor/bhq236

Halcox, J. P., Narayanan, S., Cramer-Joyce, L., Mincemoyer, R., & Quyyumi, A. A. (2001). Characterization of endothelium-derived hyperpolarizing factor in the human forearm microcirculation. *Am J Physiol Heart Circ Physiol, 280*(6), H2470-2477.

Heeger, D. J., & Ress, D. (2002). What does fMRI tell us about neuronal activity? *Nature Reviews Neuroscience, 3*(2), 142-151.

Herron, T. J., Lee, P., & Jalife, J. (2012). Optical imaging of voltage and calcium in cardiac cells & tissues. *Circ Res, 110*(4), 609-623. doi: 10.1161/CIRCRESAHA.111.247494

Hewson-Stoate, N., Jones, M., Martindale, J., Berwick, J., & Mayhew, J. (2005). Further nonlinearities in neurovascular coupling in rodent barrel cortex. *Neuroimage, 24*(2), 565-574.

Hillman, E. M. (2014). Coupling Mechanism and Significance of the BOLD Signal: A Status Report. *Annu Rev Neurosci, 37*, 161-181. doi: 10.1146/annurev-neuro-071013-014111

Hirano, Y., Stefanovic, B., & Silva, A. C. (2011). Spatiotemporal evolution of the functional magnetic resonance imaging response to ultrashort stimuli. *The journal of neuroscience, 31*(4), 1440-1447.

Hu, X., & Yacoub, E. (2012). The story of the initial dip in fMRI. *Neuroimage, 62*(2), 1103-1108. doi: 10.1016/j.neuroimage.2012.03.005

Huang, S., Heikal, A. A., & Webb, W. W. (2002). Two-photon fluorescence spectroscopy and microscopy of NAD(P)H and flavoprotein. *Biophys J, 82*(5), 2811-2825. doi: 10.1016/S0006-3495(02)75621-X

Iadecola, C., Yang, G., Ebner, T. J., & Chen, G. (1997). Local and propagated vascular responses evoked by focal synaptic activity in cerebellar cortex. *J Neurophysiol, 78*(2), 651-659.

Joshi, S., Li, Y., Kalwani, R. M., & Gold, J. I. (2016). Relationships between Pupil Diameter and Neuronal Activity in the Locus Coeruleus, Colliculi, and Cingulate Cortex. *Neuron, 89*(1), 221-234. doi: 10.1016/j.neuron.2015.11.028

Kansui, Y., Garland, C. J., & Dora, K. A. (2008). Enhanced spontaneous Ca2+ events in endothelial cells reflect signalling through myoendothelial gap junctions in pressurized mesenteric arteries. *Cell Calcium, 44*(2), 135-146. doi: 10.1016/j.ceca.2007.11.012

Kasischke, K. A., Lambert, E. M., Panepento, B., Sun, A., Gelbard, H. A., Burgess, R. W., . . . Nedergaard, M. (2011). Two-photon NADH imaging exposes boundaries of oxygen diffusion in cortical vascular supply regions. *J Cereb Blood Flow Metab, 31*(1), 68-81. doi: 10.1038/jcbfm.2010.158

Kasischke, K. A., Vishwasrao, H. D., Fisher, P. J., Zipfel, W. R., & Webb, W. W. (2004). Neural activity triggers neuronal oxidative metabolism followed by astrocytic glycolysis. *Science, 305*(5680), 99-103. doi: 10.1126/science.1096485

Kasprzak, J. D., Klosinska, M., & Drozdz, J. (2006). Clinical aspects of assessment of endothelial function. *Pharmacol Rep, 58 Suppl*, 33-40.

Kelleher, R. J., & Soiza, R. L. (2013). Evidence of endothelial dysfunction in the development of Alzheimer's disease: Is Alzheimer's a vascular disorder? *Am J Cardiovasc Dis, 3*(4), 197-226.

Kennerley, A. J., Harris, S., Bruyns-Haylett, M., Boorman, L., Zheng, Y., Jones, M., & Berwick, J. (2012). Early and late stimulus-evoked cortical hemodynamic responses provide insight into the neurogenic nature of neurovascular coupling. *J Cereb Blood Flow Metab, 32*(3), 468-480. doi: 10.1038/jcbfm.2011.163

Kozberg, M. G., Ma, Y., Shaik, M. A., Kim, S. H., & Hillman, E. M. (2016). Rapid Postnatal Expansion of Neural Networks Occurs in an Environment of Altered Neurovascular and Neurometabolic Coupling. *J Neurosci, 36*(25), 6704-6717. doi: 10.1523/JNEUROSCI.2363-15.2016

Kunz, W. S., & Kunz, W. (1985). Contribution of different enzymes to flavoprotein fluorescence of isolated rat liver mitochondria. *Biochim Biophys Acta, 841*(3), 237-246.

Lacroix, A., Toussay, X., Anenberg, E., Lecrux, C., Ferreiros, N., Karagiannis, A., . . . Cauli, B. (2015). COX-2-Derived Prostaglandin E2 Produced by Pyramidal Neurons Contributes to

Neurovascular Coupling in the Rodent Cerebral Cortex. *J Neurosci, 35*(34), 11791-11810. doi: 10.1523/JNEUROSCI.0651-15.2015

Lecrux, C., Kocharyan, A., Sandoe, C. H., Tong, X. K., & Hamel, E. (2012). Pyramidal cells and cytochrome P450 epoxygenase products in the neurovascular coupling response to basal forebrain cholinergic input. *J Cereb Blood Flow Metab, 32*(5), 896-906. doi: 10.1038/jcbfm.2012.4

Lecrux, C., Sandoe, C. H., Neupane, S., Kropf, P., Toussay, X., Tong, X. K., . . . Hamel, E. (2017). Impact of Altered Cholinergic Tones on the Neurovascular Coupling Response to Whisker Stimulation. *J Neurosci, 37*(6), 1518-1531. doi: 10.1523/JNEUROSCI.1784-16.2016

Lecrux, C., Toussay, X., Kocharyan, A., Fernandes, P., Neupane, S., Levesque, M., . . . Hamel, E. (2011). Pyramidal neurons are "neurogenic hubs" in the neurovascular coupling response to whisker stimulation. *J Neurosci, 31*(27), 9836-9847. doi: 10.1523/JNEUROSCI.4943-10.2011

Leshchenko, Y., Likhodii, S., Yue, W., Burnham, W. M., & Perez Velazquez, J. L. (2006). Carbenoxolone does not cross the blood brain barrier: an HPLC study. *BMC Neurosci, 7*, 3. doi: 10.1186/1471-2202-7-3

Lind, B. L., Brazhe, A. R., Jessen, S. B., Tan, F. C., & Lauritzen, M. J. (2013). Rapid stimulus-evoked astrocyte Ca2+ elevations and hemodynamic responses in mouse somatosensory cortex in vivo. *Proc Natl Acad Sci U S A, 110*(48), E4678-4687. doi: 10.1073/pnas.1310065110

Lind, B. L., Jessen, S. B., Lonstrup, M., Josephine, C., Bonvento, G., & Lauritzen, M. (2017). Fast Ca2+ responses in astrocyte end-feet and neurovascular coupling in mice. *Glia*. doi: 10.1002/glia.23246

Liu, X., Li, C., Falck, J. R., Harder, D. R., & Koehler, R. C. (2012). Relative contribution of cyclooxygenases, epoxyeicosatrienoic acids, and pH to the cerebral blood flow response to vibrissal stimulation. *Am J Physiol Heart Circ Physiol, 302*(5), H1075-1085. doi: 10.1152/ajpheart.00794.2011

Liu, X., Zhu, X. H., Zhang, Y., & Chen, W. (2013). The change of functional connectivity specificity in rats under various anesthesia levels and its neural origin. *Brain Topogr, 26*(3), 363-377. doi: 10.1007/s10548-012-0267-5

Logothetis, N. K., Murayama, Y., Augath, M., Steffen, T., Werner, J., & Oeltermann, A. (2009). How not to study spontaneous activity. *Neuroimage, 45*(4), 1080-1089. doi: 10.1016/j.neuroimage.2009.01.010

Logothetis, N. K., Pauls, J., Augath, M., Trinath, T., & Oeltermann, A. (2001). Neurophysiological investigation of the basis of the fMRI signal. *Nature, 412*(6843), 150-157.

Logothetis, N. K., Pauls, J., Augath, M., Trinath, T., & Oeltermann, A. (2001). Neurophysiological investigation of the basis of the fMRI signal. *Nature, 412*(6843), 150-157. doi: 10.1038/35084005

Longden, T. A., Dabertrand, F., Koide, M., Gonzales, A. L., Tykocki, N. R., Brayden, J. E., . . . Nelson, M. T. (2017). Capillary K+-sensing initiates retrograde hyperpolarization to increase local cerebral blood flow. *Nat Neurosci, 20*(5), 717-726. doi: 10.1038/nn.4533

Longden, T. A., Dunn, K. M., Draheim, H. J., Nelson, M. T., Weston, A. H., & Edwards, G. (2011). Intermediate-conductance calcium-activated potassium channels participate in neurovascular coupling. *Br J Pharmacol, 164*(3), 922-933. doi: 10.1111/j.1476-5381.2011.01447.x

Lorincz, M. L., Gunner, D., Bao, Y., Connelly, W. M., Isaac, J. T., Hughes, S. W., & Crunelli, V. (2015). A distinct class of slow (~0.2-2 Hz) intrinsically bursting layer 5 pyramidal neurons determines UP/DOWN state dynamics in the neocortex. *J Neurosci, 35*(14), 5442-5458. doi: 10.1523/JNEUROSCI.3603-14.2015

Lu, H., Zuo, Y., Gu, H., Waltz, J. A., Zhan, W., Scholl, C. A., . . . Stein, E. A. (2007). Synchronized delta oscillations correlate with the resting-state functional MRI signal. *Proc Natl Acad Sci U S A, 104*(46), 18265-18269. doi: 10.1073/pnas.0705791104

Ma, Y., Shaik, M. A., Kim, S. H., Kozberg, M. G., Thibodeaux, D. N., Zhao, H. T., . . . Hillman, E. M. (2016). Wide-field optical mapping of neural activity and brain haemodynamics: considerations and novel approaches. *Philos Trans R Soc Lond B Biol Sci, 371*(1705). doi: 10.1098/rstb.2015.0360

Ma, Y., Shaik, M. A., Kozberg, M. G., Kim, S. H., Portes, J. P., Timerman, D., & Hillman, E. M. (2016). Resting-state hemodynamics are spatiotemporally coupled to synchronized and symmetric neural activity in excitatory neurons. *Proc Natl Acad Sci U S A, 113*(52), E8463-E8471. doi: 10.1073/pnas.1525369113

Martin, C., Martindale, J., Berwick, J., & Mayhew, J. (2006). Investigating neural-hemodynamic coupling and the hemodynamic response function in the awake rat. *Neuroimage, 32*, 33-48. doi: 10.1016/j.neuroimage.2006.02.021

Martin, C., Martindale, J., Berwick, J., & Mayhew, J. (2006). Investigating neural-hemodynamic coupling and the hemodynamic response function in the awake rat. *Neuroimage, 32*(1), 33-48. doi: 10.1016/j.neuroimage.2006.02.021

Martin, C., Zheng, Y., Sibson, N. R., Mayhew, J. E., & Berwick, J. (2013). Complex spatiotemporal haemodynamic response following sensory stimulation in the awake rat. *Neuroimage, 66*, 1-8. doi: 10.1016/j.neuroimage.2012.10.006

Martin, C., Zheng, Y., Sibson, N. R., Mayhew, J. E. W., & Berwick, J. (2013). Complex spatiotemporal haemodynamic response following sensory stimulation in the awake rat. *Neuroimage, 66*, 1-8. doi: 10.1016/j.neuroimage.2012.10.006

Martindale, J., Berwick, J., Martin, C., Kong, Y., Zheng, Y., & Mayhew, J. (2005). Long duration stimuli and nonlinearities in the neural-haemodynamic coupling. *J Cereb Blood Flow Metab, 25*(5), 651-661. doi: 10.1038/sj.jcbfm.9600060

Martindale, J., Berwick, J., Martin, C., Kong, Y., Zheng, Y., & Mayhew, J. (2005). Long duration stimuli and nonlinearities in the neural-haemodynamic coupling. *Journal of cerebral blood flow and metabolism : official journal of the International Society of Cerebral Blood Flow and Metabolism, 25*, 651-661. doi: 10.1038/sj.jcbfm.9600060

McCaslin, A. F., Chen, B. R., Radosevich, A. J., Cauli, B., & Hillman, E. M. (2011). In vivo 3D morphology of astrocyte-vasculature interactions in the somatosensory cortex: implications for neurovascular coupling. *J Cereb Blood Flow Metab, 31*(3), 795-806. doi: 10.1038/jcbfm.2010.204

Meng, L., & Zheng, T. (2016). Phase-Aligned Spectral Filtering for Decomposing Spatiotemporal Dynamics. *arXiv:1604.04899*.

Mishra, A., O'Farrell, F. M., Reynell, C., Hamilton, N. B., Hall, C. N., & Attwell, D. (2014). Imaging pericytes and capillary diameter in brain slices and isolated retinae. *Nat Protoc, 9*(2), 323-336. doi: 10.1038/nprot.2014.019

Mohajerani, M. H., McVea, D. A., Fingas, M., & Murphy, T. H. (2010). Mirrored bilateral slow-wave cortical activity within local circuits revealed by fast bihemispheric voltage-sensitive dye imaging in anesthetized and awake mice. *J Neurosci, 30*(10), 3745-3751. doi: 10.1523/JNEUROSCI.6437-09.2010

Mroszczak, E. J., Lee, F. W., Combs, D., Sarnquist, F. H., Huang, B. L., Wu, A. T., . . . Cho, D. K. (1987). Ketorolac tromethamine absorption, distribution, metabolism, excretion, and pharmacokinetics in animals and humans. *Drug Metab Dispos, 15*(5), 618-626.

Nir, Y., Mukamel, R., Dinstein, I., Privman, E., Harel, M., Fisch, L., . . . Malach, R. (2008). Interhemispheric correlations of slow spontaneous neuronal fluctuations revealed in human sensory cortex. *Nat Neurosci, 11*(9), 1100-1108.

Niwa, K., Haensel, C., Ross, M. E., & Iadecola, C. (2001). Cyclooxygenase-1 participates in selected vasodilator responses of the cerebral circulation. *Circ Res, 88*(6), 600-608.

Nizar, K., Uhlirova, H., Tian, P., Saisan, P. A., Cheng, Q., Reznichenko, L., . . . Devor, A. (2013). In vivo stimulus-induced vasodilation occurs without IP3 receptor activation and may precede astrocytic calcium increase. *J Neurosci, 33*(19), 8411-8422. doi: 10.1523/JNEUROSCI.3285-12.2013

Pellerin, L., Pellegri, G., Bittar, P. G., Charnay, Y., Bouras, C., Martin, J. L., . . . Magistretti, P. J. (1998). Evidence supporting the existence of an activity-dependent astrocyte-neuron lactate shuttle. *Dev Neurosci, 20*(4-5), 291-299.

Petersen, C. C., Hahn, T. T., Mehta, M., Grinvald, A., & Sakmann, B. (2003). Interaction of sensory responses with spontaneous depolarization in layer 2/3 barrel cortex. *Proc Natl Acad Sci U S A, 100*(23), 13638-13643. doi: 10.1073/pnas.2235811100

Petzold, G. C., Albeanu, D. F., Sato, T. F., & Murthy, V. N. (2008). Coupling of neural activity to blood flow in olfactory glomeruli is mediated by astrocytic pathways. *Neuron, 58*(6), 897-910. doi: 10.1016/j.neuron.2008.04.029

Pickard, J. D., Murray, G. D., Illingworth, R., Shaw, M. D., Teasdale, G. M., Foy, P. M., . . . et al. (1989). Effect of oral nimodipine on cerebral infarction and outcome after subarachnoid haemorrhage: British aneurysm nimodipine trial. *BMJ, 298*(6674), 636-642.

Pisauro, M. A., Dhruv, N. T., Carandini, M., & Benucci, A. (2013). Fast hemodynamic responses in the visual cortex of the awake mouse. *J Neurosci, 33*(46), 18343-18351. doi: 10.1523/JNEUROSCI.2130-13.2013

Prakash, N., Biag, J. D., Sheth, S. A., Mitsuyama, S., Theriot, J., Ramachandra, C., & Toga, A. W. (2007). Temporal profiles and 2-dimensional oxy-, deoxy-, and total-hemoglobin somatosensory maps in rat versus mouse cortex. *Neuroimage, 37 Suppl 1*, S27-36. doi: 10.1016/j.neuroimage.2007.04.063

Rabinstein, A. A., Weigand, S., Atkinson, J. L., & Wijdicks, E. F. (2005). Patterns of cerebral infarction in aneurysmal subarachnoid hemorrhage. *Stroke, 36*(5), 992-997. doi: 10.1161/01.STR.0000163090.59350.5a

Rice, A. S., Lloyd, J., Bullingham, R. E., & O'Sullivan, G. (1993). Ketorolac penetration into the cerebrospinal fluid of humans. *J Clin Anesth, 5*(6), 459-462.

Rochette, L., Lorin, J., Zeller, M., Guilland, J. C., Lorgis, L., Cottin, Y., & Vergely, C. (2013). Nitric oxide synthase inhibition and oxidative stress in cardiovascular diseases: possible therapeutic targets? *Pharmacol Ther, 140*(3), 239-257. doi: 10.1016/j.pharmthera.2013.07.004

Rosenegger, D. G., Tran, C. H., Wamsteeker Cusulin, J. I., & Gordon, G. R. (2015). Tonic Local Brain Blood Flow Control by Astrocytes Independent of Phasic Neurovascular Coupling. *J Neurosci, 35*(39), 13463-13474. doi: 10.1523/JNEUROSCI.1780-15.2015

Roy, C. S., & Sherrington, C. S. (1890). On the Regulation of the Blood-supply of the Brain. *J Physiol, 11*(1-2), 85-158 117.

Rush, D. K. (1986). Reversal of scopolamine-induced amnesia of passive avoidance by pre- and post-training naloxone. *Psychopharmacology (Berl), 89*(3), 296-300.

Segal, S. S. (2015). Integration and Modulation of Intercellular Signaling Underlying Blood Flow Control. *J Vasc Res, 52*(2), 136-157. doi: 10.1159/000439112

Sheth, S. A., Nemoto, M., Guiou, M., Walker, M., Pouratian, N., & Toga, A. W. (2004). Linear and nonlinear relationships between neuronal activity, oxygen metabolism, and hemodynamic responses. *Neuron, 42*(2), 347-355.

Shih, A. Y., Mateo, C., Drew, P. J., Tsai, P. S., & Kleinfeld, D. (2012). A polished and reinforced thinned-skull window for long-term imaging of the mouse brain. *J Vis Exp*(61). doi: 10.3791/3742

Shmuel, A., & Leopold, D. A. (2008). Neuronal correlates of spontaneous fluctuations in fMRI signals in monkey visual cortex: Implications for functional connectivity at rest. *Hum Brain Mapp, 29*(7), 751-761. doi: 10.1002/hbm.20580

Silva, A. C., & Koretsky, A. P. (2002). Laminar specificity of functional MRI onset times during somatosensory stimulation in rat. *Proc Natl Acad Sci U S A, 99*(23), 15182-15187. doi: 10.1073/pnas.222561899

Sirotin, Y. B., Hillman, E. M., Bordier, C., & Das, A. (2009). Spatiotemporal precision and hemodynamic mechanism of optical point spreads in alert primates. *Proc Natl Acad Sci U S A, 106*(43), 18390-18395. doi: 10.1073/pnas.0905509106

Sonkusare, S. K., Bonev, A. D., Ledoux, J., Liedtke, W., Kotlikoff, M. I., Heppner, T. J., . . . Nelson, M. T. (2012). Elementary Ca2+ signals through endothelial TRPV4 channels regulate vascular function. *Science, 336*(6081), 597-601. doi: 10.1126/science.1216283

Spector, A. A. (2009). Arachidonic acid cytochrome P450 epoxygenase pathway. *J Lipid Res, 50 Suppl*, S52-56. doi: 10.1194/jlr.R800038-JLR200

Sreenivasan, V., Kyriakatos, A., Mateo, C., Jaeger, D., & Petersen, C. C. (2017). Parallel pathways from whisker and visual sensory cortices to distinct frontal regions of mouse neocortex. *Neurophotonics, 4*(3), 031203. doi: 10.1117/1.NPh.4.3.031203

Stroh, A., Adelsberger, H., Groh, A., Ruhlmann, C., Fischer, S., Schierloh, A., . . . Konnerth, A. (2013). Making waves: initiation and propagation of corticothalamic Ca2+ waves in vivo. *Neuron, 77*(6), 1136-1150. doi: 10.1016/j.neuron.2013.01.031

Sun, R., Bouchard, M. B., & Hillman, E. M. (2010). SPLASSH: Open source software for camera-based high-speed, multispectral in-vivo optical image acquisition. *Biomed Opt Express, 1*(2), 385-397. doi: 10.1364/BOE.1.000385

Takano, T., Tian, G. F., Peng, W., Lou, N., Libionka, W., Han, X., & Nedergaard, M. (2006). Astrocyte-mediated control of cerebral blood flow. *Nat Neurosci, 9*(2), 260-267. doi: 10.1038/nn1623

Takuwa, H., Autio, J., Nakayama, H., Matsuura, T., Obata, T., Okada, E., . . . Kanno, I. (2011). Reproducibility and variance of a stimulation-induced hemodynamic response in barrel cortex of awake behaving mice. *Brain Res, 1369*, 103-111. doi: 10.1016/j.brainres.2010.11.007

Tallini, Y. N., Brekke, J. F., Shui, B., Doran, R., Hwang, S. M., Nakai, J., . . . Kotlikoff, M. I. (2007). Propagated endothelial Ca2+ waves and arteriolar dilation in vivo: measurements in Cx40BAC GCaMP2 transgenic mice. *Circ Res, 101*(12), 1300-1309. doi: 10.1161/CIRCRESAHA.107.149484

Tang, B. L. (2017). Brain activity-induced neuronal glucose uptake/glycolysis: Is the lactate shuttle not required? *Brain Res Bull, 137*, 225-228. doi: 10.1016/j.brainresbull.2017.12.010

Tian, P., Teng, I. C., May, L. D., Kurz, R., Lu, K., Scadeng, M., . . . Devor, A. (2010). Cortical depth-specific microvascular dilation underlies laminar differences in blood oxygenation level-dependent functional MRI signal. *Proc Natl Acad Sci U S A, 107*(34), 15246-15251. doi: 10.1073/pnas.1006735107

Toth, P., Tarantini, S., Tucsek, Z., Ashpole, N. M., Sosnowska, D., Gautam, T., . . . Ungvari, Z. (2014). Resveratrol treatment rescues neurovascular coupling in aged mice: role of improved cerebromicrovascular endothelial function and downregulation of NADPH oxidase. *Am J Physiol Heart Circ Physiol, 306*(3), H299-308. doi: 10.1152/ajpheart.00744.2013

Toussay, X., Basu, K., Lacoste, B., & Hamel, E. (2013). Locus coeruleus stimulation recruits a broad cortical neuronal network and increases cortical perfusion. *J Neurosci, 33*(8), 3390-3401. doi: 10.1523/JNEUROSCI.3346-12.2013

Townsend, R. G., Solomon, S. S., Chen, S. C., Pietersen, A. N., Martin, P. R., Solomon, S. G., & Gong, P. (2015). Emergence of complex wave patterns in primate cerebral cortex. *J Neurosci, 35*(11), 4657-4662. doi: 10.1523/JNEUROSCI.4509-14.2015

Uekawa, K., Koizumi, K., Hwang, J., Brunier, N., Hattori, Y., Zhou, P., & Park, L. (2016). Obligatory Role of EP1 Receptors in the Increase in Cerebral Blood Flow Produced by Hypercapnia in the Mice. *PLoS One, 11*(9), e0163329. doi: 10.1371/journal.pone.0163329

Uhlirova, H., Kilic, K., Tian, P., Thunemann, M., Desjardins, M., Saisan, P. A., . . . Devor, A. (2016). Cell type specificity of neurovascular coupling in cerebral cortex. *Elife, 5*. doi: 10.7554/eLife.14315

Vanni, M. P., & Murphy, T. H. (2014). Mesoscale transcranial spontaneous activity mapping in GCaMP3 transgenic mice reveals extensive reciprocal connections between areas of somatomotor cortex. *J Neurosci, 34*(48), 15931-15946. doi: 10.1523/JNEUROSCI.1818-14.2014

Virdis, A., Neves, M. F., Duranti, E., Bernini, G., & Taddei, S. (2013). Microvascular endothelial dysfunction in obesity and hypertension. *Curr Pharm Des, 19*(13), 2382-2389.

Yang, H. H., & St-Pierre, F. (2016). Genetically Encoded Voltage Indicators: Opportunities and Challenges. *J Neurosci, 36*(39), 9977-9989. doi: 10.1523/JNEUROSCI.1095-16.2016

Yeşilyurt, B., Uğurbil, K., & Uludağ, K. (2008). Dynamics and nonlinearities of the BOLD response at very short stimulus durations. *Magnetic resonance imaging, 26*(7), 853-862.

Zhang, J. Y., Cao, Y. X., Xu, C. B., & Edvinsson, L. (2006). Lipid-soluble smoke particles damage endothelial cells and reduce endothelium-dependent dilatation in rat and man. *BMC Cardiovasc Disord, 6*, 3. doi: 10.1186/1471-2261-6-3

Zhang, L., Papadopoulos, P., & Hamel, E. (2013). Endothelial TRPV4 channels mediate dilation of cerebral arteries: impairment and recovery in cerebrovascular pathologies related to Alzheimer's disease. *Br J Pharmacol, 170*(3), 661-670. doi: 10.1111/bph.12315

Zhang, Y., Chen, K., Sloan, S. A., Bennett, M. L., Scholze, A. R., O'Keeffe, S., . . . Wu, J. Q. (2014). An RNA-sequencing transcriptome and splicing database of glia, neurons, and vascular cells of the cerebral cortex. *J Neurosci, 34*(36), 11929-11947. doi: 10.1523/JNEUROSCI.1860-14.2014

Zheng, Y., Pan, Y., Harris, S., Billings, S., Coca, D., Berwick, J., . . . Mayhew, J. (2010). A dynamic model of neurovascular coupling: Implications for blood vessel dilation and constriction. *Neuroimage, 52*, 1135-1147. doi: 10.1016/j.neuroimage.2010.01.102

Zhou, Y., Wang, Z., Zuo, X. N., Zhang, H., Wang, Y., Jiang, T., & Liu, Z. (2014). Hyper-coupling between working memory task-evoked activations and amplitude of spontaneous fluctuations in first-episode schizophrenia. *Schizophr Res, 159*(1), 80-89. doi: 10.1016/j.schres.2014.07.023

Appendix

Related Publications and Presentations

Publications

Ma Y*, **Shaik MA***, Kim SH, Kozberg MG, Thibodeaux DN, Zhao HT, Yu H, Hillman EM. Wide-field optical mapping of neural activity and brain haemodynamics: considerations and novel approaches. Philos Trans R Soc Lond B Biol Sci. 2016 Oct 5;371(1705). pii: 20150360. doi: 10.1098/rstb.2015.0360. Review. PubMed PMID: 27574312; PubMed Central PMCID: PMC5003860.

*Co-authors.

Ma Y, **Shaik MA**, Kozberg MG, Kim SH, Portes JP, Timerman D, Hillman EM. Resting-state hemodynamics are spatiotemporally coupled to synchronized and symmetric neural activity in excitatory neurons. Proc Natl Acad Sci U S A. 2016 Dec 27;113(52):E8463-E8471. doi: 10.1073/pnas.1525369113. Epub 2016 Dec 14. PubMed PMID: 27974609; PubMed Central PMCID: PMC5206542.

Kozberg MG, Ma Y, **Shaik MA**, Kim SH, Hillman EM. Rapid Postnatal Expansion of Neural Networks Occurs in an Environment of Altered Neurovascular and Neurometabolic Coupling. J Neurosci. 2016 Jun 22;36(25):6704-17. doi: 10.1523/JNEUROSCI.2363-15.2016. PubMed PMID: 27335402; PubMed Central PMCID: PMC4916248

Chen BR, Kozberg MG, Bouchard MB, **Shaik MA**, Hillman EM. A critical role for the vascular endothelium in functional neurovascular coupling in the brain. J Am Heart Assoc. 2014 Jun 12;3(3):e000787. doi: 10.1161/JAHA.114.000787. PubMed PMID: 24926076; PubMed Central PMCID: PMC4309064.

Shaik MA, Ma Y, Portes J, Kim SH, Thibodeaux DN, Voleti V, Kozberg M, Hillman EM. Selective perturbation of neurovascular coupling reveals dual endothelial mechanisms. *Pending Submission*

Conference Posters

Shaik MA, Thibodeaux ND, Kim SH, Hillman EMC, "Wide field optical mapping (WFOM) of large-scale neuronal activity and hemodynamics in the awake mouse cortex, Society of General Physiologists, October, 2017, Woods Hole, MA

Shaik MA, Kim SH, Ma Y, Hillman EMC, "Investigating the effect of nonselective COX-inhibition on neuronal and vascular dynamics in the awake mouse cortex", Gordon Research Conference – Glial Biology: Functional Interactions Among Glia & Neurons, March 2017, Ventura, CA

Shaik MA, Kim SH, Ma Y, Zhao H, Hillman EMC, "The effects of endothelial dysfunction on neural activity, hemodynamics and neurovascular coupling." Society for Neuroscience Annual Meeting, October 2015, Chicago, IL

Shaik MA, Kim SH, Zhao H, Hillman EMC, "The influence of endothelial dysfunction on neurovascular coupling", Brain ISCBFM conference, June 2015, Vancouver, Canada

Shaik MA, Chung DY, Kozberg MG, Hillman EMC, "Assessing the contribution of endothelial mechanisms in functional neurovascular coupling", Society for Neuroscience Annual Meeting, November 2014, Washington, DC

Dynamic Poster

Shaik MA, Kim SH, Thibodeaux DN, Hillman EMC, "Endothelial dysfunction diminishes conducted vasodilation leading to abnormal functional hyperemia in the awake mouse cortex", Society for Neuroscience Annual Meeting 2016, San Diego, CA

Conference Talks

M.A. Shaik, S.H. Kim, H.T. Zhao, E.M.C. Hillman, "Simultaneous multi-region imaging of neuronal activity, hemodynamics and speckle flow in awake mice", Optics in the Brain (OSA), Vancouver, Canada, April, 2015